Single electron and single dopant control in silicon transistors

Benoit Voisin

UNIVERSITÉ DE GRENOBLE

THÈSE

Pour obtenir le grade de

DOCTEUR DE L'UNIVERSITÉ DE GRENOBLE

Spécialité : **Physique de la matière condensée et du rayonnement**

Arrêté ministériel : 7 août 2006

Présentée par

Benoit VOISIN

Thèse dirigée par **Marc SANQUER**
et codirigée par **Silvano DE FRANCESCHI**

préparée au sein **du laboratoire de transport électronique quantique et supraconductivité,**
du service de physique statistique, magnétisme et supraconductivité, de l'institut nanosciences et cryogénie,
du CEA Grenoble
et de **l'école doctorale de physique de Grenoble**

Contrôle d'électrons et de dopants uniques dans des transistors silicium.

Thèse soutenue publiquement le **16 décembre 2013**,
devant le jury composé de :

Henri MARIETTE
Unité mixte CEA/institut Néel / Grenoble, Président
Bernard PLAÇAIS
Laboratoire Pierre Aigrain / ENS Paris, Rapporteur
Floris ZWANENBURG
Faculty EEMCS / University of Twente, Rapporteur
Marc BESCOND
IM2NP / Marseille , Examinateur
Marc SANQUER
SPSMS / CEA Grenoble, Directeur de thèse
Silvano DE FRANCESCHI
SPSMS / CEA Grenoble, Co-Directeur de thèse

Contents

Abstract/Résumé

Abstract

Recent progress in Silicon-On-Insulator transistors fabrication have concerned a dimensions reduction, up to a few tens of nanometers, and an improvement of the leads. This allows to study the few electrons regime at low temperature. These latter are confined in the corners of the nanowire, where the electric field is maximized. This leads for the silicon valley degeneracy to be lifted, with a singlet for the two-electron ground state at zero magnetic field. We also investigate the interactions between these confined electrons and the electrons of the contacts conduction bands, with the Kondo effect and the Fermi-edge singularity.

The dopants, essential ingredients of the transistors fabrication, naturally lift the valley degeneracy thanks to their deep confinement potential. First, by tuning the transverse electric field, we investigate the influence of the complex environment on a donor's ionization according to its position in the nanowire. We then realized the first Coupled-Atom Transistor, where the transport is controlled by the alignment of the ground states of two dopants placed in series. We could measure an energy splitting between the two first states of the order of 10 meV, one order of magnitude larger than that of the first electrons of the conduction band. This large separation allows to manipulate the electronic states in the ten's gigahertz regime. We induce one-electron interferences between the ground states of the two dopants, opening the way towards coherent electron manipulations in dopant-based devices.

Résumé

Les récents progrès de fabrication des transistors en silicium-sur-isolant concernent la réduction de leurs dimensions, qui atteignent désormais quelques dizaines de nanomètres, et l'amélioration des contacts. Cela permet l'étude des premiers électrons du canal à basse température. Ceux-ci sont confinés dans les coins du nanofil, où le champ électrique est le plus intense. La dégénérescence de vallée du silicium est alors levée, donnant lieu à un singulet comme état à deux électrons de plus basse énergie en champ magnétique nul. La proximité de contacts quasi-métalliques permet l'étude des interactions entre ces électrons confinés et les électrons de la bande de conduction des contacts à travers l'effet Kondo et la singularité au niveau de Fermi.

D'autre part les dopants, ingrédients essentiels de la fabrication de ces transistors, offrent naturellement une levée de dégénérescence de vallée de par leur fort potentiel de confinement. En variant le champ électrique transverse, nous étudions l'influence de l'environnement complexe sur l'ionisation d'un dopant selon sa position dans le canal. Nous avons ensuite réalisé le premier transistor à atomes couplés, où le transport est contrôlé par l'alignement des niveaux de deux atomes en série, facilitant la spectroscopie: nous mesurons une séparation entre les deux premiers états d'un dopant de l'ordre de 10 meV, un ordre de grandeur plus grand que celle des premiers électrons de la bande de conduction. Cette séparation permet de manipuler les états électroniques dans le régime de la dizaine de gigahertz. Une expérience d'interférométrie à un électron entre deux dopants est réalisée, ouvrant la voie vers des manipulations cohérentes dans des systèmes à dopants uniques.

Introduction (français)

Contexte

Les semi-conducteurs sont à la base de l'électronique moderne. Depuis la réalisation du premier transistor à effet de champ dans les années 60, de nombreux travaux ont été menés pour en améliorer les performances, que ce soit en termes de vitesse, de consommation d'énergie ou de schémas d'intégration dans tous les appareils électroniques qui nous entourent : téléphones, ordinateurs, capteurs ou encore sources lumineuses. Cette électronique, dite "classique", utilise le silicium comme ingrédient essentiel, de par son abondance et ses faibles coûts de production. Ce développement si rapide, conjuguée à une économie florissante, est guidé par un consortium international, appelé ITRS[73] (International Roadmap for Semi-conductors) créé en 1994 afin de définir les prochains objectifs de la recherche en microélectronique. L'un de ses principaux axes concerne la miniaturisation de ces dispositifs, qui peuvent être désormais composés de milliards de transistors dont la taille caractéristique n'excède pas 20 nm. A une telle échelle, des effets parasites apparaissent dégradant leur comportement typique, comme de l'effet tunnel direct, de la fuite de grille ou du confinement électronique stochastique. La recherche en microélectronique s'est alors orientée vers de nouveaux matériaux et de nouvelles architectures, permettant de garder un excellent contrôle des dispositifs à ces échelles nanométriques[19].

les autres semiconducteurs n'ont cependant pas été laissés pour compte face à l'avènement de la microélectronique et du silicium. La recherche fondamentale s'est aussi orientée sur d'autres matériaux présentant de meilleures voire de nouvelles propriétés intrinsèques. On peut citer le graphène, constitué d'une monocouche d'atomes de carbone, avec sa relation de dispersion linéaire et l'absence de gap au niveau des points de Dirac. On peut aussi donner l'exemple des gaz 2D de haute mobilité issus d'hétérostructures en GaAs, qui ont amené à des découvertes majeures de la physique mésoscopique, comme la quantification de la conductance ou l'effet Hall quantique. Il est aussi possible de fabriquer des transistors à électrons uniques (communément appelés SET pour " Single Electron Transistor ") où des électrons sont confinés et contrôlés un par un dans des petits volumes. Ces SET deviennent même des boîtes quantiques lorsque le nombre d'électrons confinés est assez faible pour que des effets quantiques comme la dégénérescence de vallée ou de spin apparaissent. Ces développements ont ouvert la voie vers une nouvelle manière de coder l'information en utilisant ces nombres quantiques. En 1998, Loss et Di Vincenzo ont proposé un nouveau schéma ou les bits dits " classiques " (" 0 " ou " 1 " suivant que le transistor soit " ouvert " ou " fermé ") seraient remplacés par des bits dits " quantiques ", par exemple encodés dans les spins d'électrons confinés dont l'état peut alors être dans

une superposition quantique, soit un mélange, de " 0 " et de " 1 ". Mais si des réalisations expérimentales de tels bits quantiques ont bien vu le jour, deux obstacles majeurs restent à franchir avant d'étendre ces travaux vers la réalisation d'un ordinateur quantique. Tout d'abord ces bits ne présentent pas de temps de cohérence suffisant du au couplage de ces spins au bain de spin nucléaires fluctuant dans le temps. L'information quantique est alors trop rapidement perdue. Deuxièmement de telles hétérostructures ne sont pas compatibles avec les besoins actuels de la microéléctronique qui vise une intégration maximale des bits dans une puce électronique.

Une alternative est alors d'utiliser le silicium comme matériau hôte aussi pour ces boîtes quantiques. En effet le silicium peut-être purifier pour ne contenir quasiment aucun spin nucléaire et il est au cœur de la technologie CMOS fondée par l'industrie microélectronique. Cela le rend donc très attractif pour des applications quantiques à large échelle. Si des SET en silicium ont été réalisés dès la fin des années 80, être capable de fabriquer des structures en silicium de petites tailles, permettant le contrôle sur les premiers électrons d'une boîte, est resté un défi. Mais il est en passe d'être relevé grâce aux formidables développements de la microélectronique, qui devient même nanoélectronique avec ces dimensions caractéristiques de l'ordre de la dizaine de nanomètres. Cela ouvre même l'étude de dopants uniques dans le silicium : Kane proposa d'utiliser le spin nucléaire d'un donneur dans le silicium comme bit quantique, et de premières expériences ont récemment été reportées. Le dopage dans les semi-conducteurs a été largement étudié dans le cas macroscopique depuis les années 50, les propriétés d'un atome unique dans du silicium massif sont donc bien connues. Un point crucial est maintenant de comprendre comment ces propriétés sont affectées par la présence d'un environnement mésoscopique formé d'oxydes et de différentes électrodes, inhérent au contrôle de tels objets.

Le but de cette thèse est donc d'étudier les propriétés d'éléctrons uniques dans ces nano-transistors modernes. Ces dispositifs de taille ultime sont fabriqués par le LETI (Laboratoire d'Electronique et des Technologies de l'Information), une plateforme CMOS semi-industrielle de Grenoble. Ce travail s'inscrit dans la continuité des thèses de Max Hofheinz et de Mathieu Pierre, qui ont montré que ces dispositifs se comportent comme des SET à basse température et ont pu ainsi étudier le régime à grand nombre d'électrons. Ils ont aussi mis évidence le rôle des dopants uniques, soit par transport direct ou par transport assisté par un dopant. Une première partie de mes travaux consiste à démontrer que l'on peut désormais atteindre le régime à faible nombre d'électrons dans des dispositifs de nouvelle génération avec des architectures de source et drain améliorées, donnant de meilleures électrodes. J'ai aussi travaillé étroitement avec Benoît Roche, un autre étudiant qui a soutenu sa thèse en 2012. Dans une deuxième partie, de récents résultats sur le couplage de deux donneurs dans le silicium et sur l'échange cohérent d'électrons seront présentés.

Contenu

Ce manuscript est composé de cinq chapitres.

Le premier chapitre présentera les principaux challenges de la microélectronique moderne ainsi que les développements de la fabrication qui en ont résulté. Nous rappellerons les résultats clés obtenus sur la physique des SET et des dopants uniques dans le silicium. Cela servira de base pour le reste du manuscrit.

Au cours du chapitre 2 nous étudierons le régime des premiers électrons d'une boîte quantique, s'intéressant notamment à leur spectroscopie. Nous étudierons aussi l'impact des réservoirs à travers les effets Kondo et de singularité au niveau de Fermi.

Le rôle d'un environnement proche et complexe sera le fil conducteur du chapitre 3 qui s'intéressera au transport à travers des dopants uniques dans de très courts nanofils trigates. On révélera l'influence de la position du donneur, du champ électrique transverse et des différentes électrodes sur son ionisation. Le problème de la double occupation, où deux électrons sont liés à un seul donneur sera également traité. Ces études s'appuieront largement sur des simulations numériques implémentées en collaboration avec un autre groupe du CEA Grenoble, qui prennent en compte la réelle géométrie 3D des dispositifs.

Le chapitre 4 commencera par la présentation d'autres simulations faites par le LETI, qui illustreront comment le processus de diffusion des dopants, inévitable dans la technologie CMOS, peut être guidé grâce à une nouvelle géométrie des échantillons avec deux grilles face-à-face. Cela nous amènera à la présentation du premier transistors à donneurs couplés que nous avons réalisé, insistant particulièrement sur l'aspect spectroscopique qui en est facilité. Une comparaison avec les résultats du chapitre 2 sera dressée.

Enfin le chapitre 5 montrera tout d'abord les résultats préliminaires obtenus sur la relaxation d'un état excité de spin. Nous décrirons ensuite en détails l'échange cohérent d'un électron entre deux donneurs présents dans le silicium grâce à des transitions Landau-Zener. Ces travaux constituent une première étape vers la manipulation cohérente d'un état de charge entre deux atomes.

Introduction

Context

Semiconductors are the cornerstone of modern electronics. After the first realization of a field effect transistor in the 60's, intense efforts have been devoted to the improvement of their characteristics in terms of speed, power consumption and integration schemes into almost every electronic devices of our everyday life: phones, computers, sensors or light sources. Classical electronics mostly uses silicon as the host material, especially thanks to its abundance and low fabrication cost. The key point which has guided microelectronics research over the last decades is a constant hunt for device miniaturization. An international consortium has been created in 1994, under the acronym ITRS (International Roadmap for Semi-conductors) [73], which sets the targets for the future developments of microelectronics. Current commercial devices are composed of billions of transistors whose dimensions don't exceed 20 nm. At this scale, the transistors exhibit parasitic effects such as direct tunneling, gate leakage or stochastic electron confinement, which degrade the transistor behaviour. In order to face this problem, microelectronics research has to come up with new materials and architectures fostering an excellent device control at such nanometer scales [19].

Other semiconductors have not been left aside in the meantime. In parallel to the development of microelectronics, fundamental research also focus on materials with better or even new intrinsic properties compared to silicon. A striking example is graphene, a 2D layer of carbon atoms, with its linear dispersion relation near the well known Dirac points where the band gap closes. An other is the design and the control of high mobility electron gas in GaAs heterostructures which have allowed to observe some of the milestones of mesoscopic physics, such as the conductance quantization and the quantum Hall effect. One can also create Single Electron Transistors (SET), with the confinement and the one-by-one control of electrons in a small region of space. SETs even become quantum dots in the limit of a small number of electrons where quantum effects such as spin and orbital degeneracies come into play. These developments have opened a new way to encode information using these quantum numbers. In 1998, Loss and Di Vincenzo [62] proposed a new computing scheme where the classical bits ("0" or "1", corresponding to a transistor open or close) would be replaced by quantum bits, encoded in the spins of confined electrons, where the states "0" and "1" can be in a quantum superposition. If experimental realizations of quantum bits have been achieved [78, 54], two major issues prevent from extending these works into a large scale quantum computer scheme. First, these quantum bits do not present sufficient coherence times due to the coupling between

the electrons and the fluctuating nuclear spin bath. Secondly such heterostructures are not compatible with a scalable integration scheme, which is absolutely necessary for further applications.

An alternative option is to use silicon as host material for these quantum dots. Indeed silicon presents almost no nuclear spin and it is at the core of the CMOS technology. This makes this material very attractive for quantum applications. If silicon SETs were already realized long time ago [100], achieving sufficiently small structures to enable a good control over the first electrons of a dot has been challenging. This has now become possible thanks to outstanding fabrication developments, resulting in devices dimensions of the order of tens of nanometers. These scales also allow to investigate single donors in silicon: Kane proposed to use the nuclear spin of single donors in silicon as quantum bits [47], and some first experimental realizations were recently reported [66, 83]. Doped semiconductors have been widely studied in the macroscopic case since the 50's [23], the bulk properties of single atoms are then well established. A crucial point is now to understand how these properties are affected by the proximity of a mesoscopic environment such as electrodes and oxides, essential for the control of a single dopant.

The aim of this thesis is then to investigate the properties of single electrons in modern silicon nano-transistors. These ultimate transistors are fabricated at LETI (Laboratoire d'Electronique et des Technologies de l'Information), a semi-industrial CMOS foundry of CEA Grenoble. It follows the work done by Max Hofheinz and Mathieu Pierre during their thesis. They showed that these field-effect transistors become Single Electron Transistors at low temperature and could investigate the large electron number regime of these SETs. They also evidenced the role of single donors, either by direct resonant transport or dopant-assisted transport. A first part of my PhD work, done in LaTEQS in CEA Grenoble, has been to demonstrate the achievement of the single electron regime in new-generation's devices, with improved source and drain architectures, resulting in better and closer electrodes. I also worked in close collaboration with Benoît Roche, an other PhD student who graduated in 2012. In a second part, recent results on the coupling between donors in a silicon nanostructure and coherent electron exchange will also be presented.

Contents

This manuscript is divided into five chapters.

The first chapter will present the main challenges of nowadays microelectronics and the resulting fabrication developments. We will also review the main results on SET and single dopant physics in silicon. This will serve as a basis for the rest of the manuscript.

In Chapter 2, we will investigate the first electron's regime in modern transistors. We will focus on the spectroscopy of these first electrons. We will also investigate the impact of the reservoirs on these first electrons through the Kondo and the Fermi-edge singularities effects.

The impact of a nearby environment will also be leading the development of the

Chapter 3, investigating the transport through individual donors in very short trigate nanowires. It will reveal the impact of the donor location, of the transverse electric field and of the different electrodes on its ionization. The issue of the double occupation, with two electrons bound to a single donor, will also be tackled. The support of numerical simulations done in collaboration with an other group of CEA Grenoble, taking into account the actual device geometry, will be very useful.

Chapter 4 will present process simulations, done by LETI, which will illustrate how the dopant diffusion process, well controlled but unavoidable in CMOS technology, can be guided thanks to a new device geometry using two front gates facing each other. This will lead us to the first Coupled-Atom transistors, and we will especially emphasize on the clear spectroscopy which can be carried out. A comparison with the results obtained on the first electrons in Chapter 2 will be performed.

Chapter 5 will first present preliminary results on the relaxation time of a spin excited state. We will also describe in detail the coherent electron exchange which can be induced thanks to Landau-Zener transitions between two As atoms embedded in silicon. This work represent a first step towards coherent manipulation of a charge state between two atoms.

Chapter 1

Towards silicon quantum electronics

Contents

Introduction

Silicon has been the base element for the microelectronics industry since the last fifty years. We can identify many reasons to account for this fact: its abundance on earth (second element in earth crust after oxygen), an easy purification, a good crystallisation and the native presence of a good oxide. Thanks to these properties and their resulting low fabrication cost, silicon has guided every technological advance in modern electronics during the last decades, from the first transistors in 1948 to the most recent "smart" phones, despite a low mobility. We will see in this chapter the main technological challenges that the CMOS technology has to face and the modern transistors characteristics.

The intense efforts devoted to the size reduction of such devices, while keeping an excellent electrostatic control over a small volume of silicon have now led them to become an excellent candidate to study single electron and single atom physics at low temperature. This concerns not only these etched silicon nanostructures but also many others silicon-based devices fabricated with different techniques: self-assembled nanocrystals, CVD nanowires or STM patterned. We will describe the main properties of the quantum dots through the Coulomb blockade regime which can be induced in those nanostructures.

Finally, following these outstanding fabrication developments, we are now able to probe single dopants in silicon by resonant transport. Single atomic orbitals represent the ultimate building blocks of condensed matter and are promising candidates for future quantum computing applications.

1.1 The CMOS MOSFET on SOI

1.1.1 Main physical properties of silicon

We first remind the main physical properties of bulk silicon. Silicon, under its crystalline form, is a covalent bonded crystal with atoms placed on a diamond-like, face-centered-cubic lattice with a lattice parameter $a = 5.43\,\text{Å}$. Thus it has a cubic symmetry leading to six degenerate valleys in its conduction band. We will see in the next sections how this degeneracy can be lifted in a nanostructure. The band structure of silicon is represented in Fig 1.1. It has an indirect gap of 1.12 eV at 300K (1.169 eV at 4K) with the six-fold degenerate minimum of the conduction band found between points Γ and X at $\|\overrightarrow{k_0}\| = 0.85\,(2\pi/a)$. The parabolic dispersion of the conduction band around $\overrightarrow{k_0}$ allows to extract the longitudinal and the transverse effective masses (respectively $m_l^* = 0.916\,m_e$ and $m_t^* = 0.190\,m_e$), with m_e the mass of a free electron. An other typical quantity of interest is the silicon mobility which, in absence of doping, can reach $10^4\,cm^2.V^{-1}.s^{-1}$ but drops to $\mu \approx 10^2\,cm^2.V^{-1}.s^{-1}$ in typical transistors at room temperature.

Compared to silicon, GaAs seems to be the perfect semi-conductor for both the microelectronics industry, thanks to its higher carrier mobility $\mu \approx 10^6\,cm^2.V^{-1}.s^{-1}$, and also for quantum applications, obviously thanks to its longer phase coherence length (10μm versus 10 nm in silicon) and mean free path ($1\,\mu$m versus 2 nm in silicon). GaAs also benefits of its smaller effective mass ($m* = 0.067\,m_e$), which leads to a higher single level

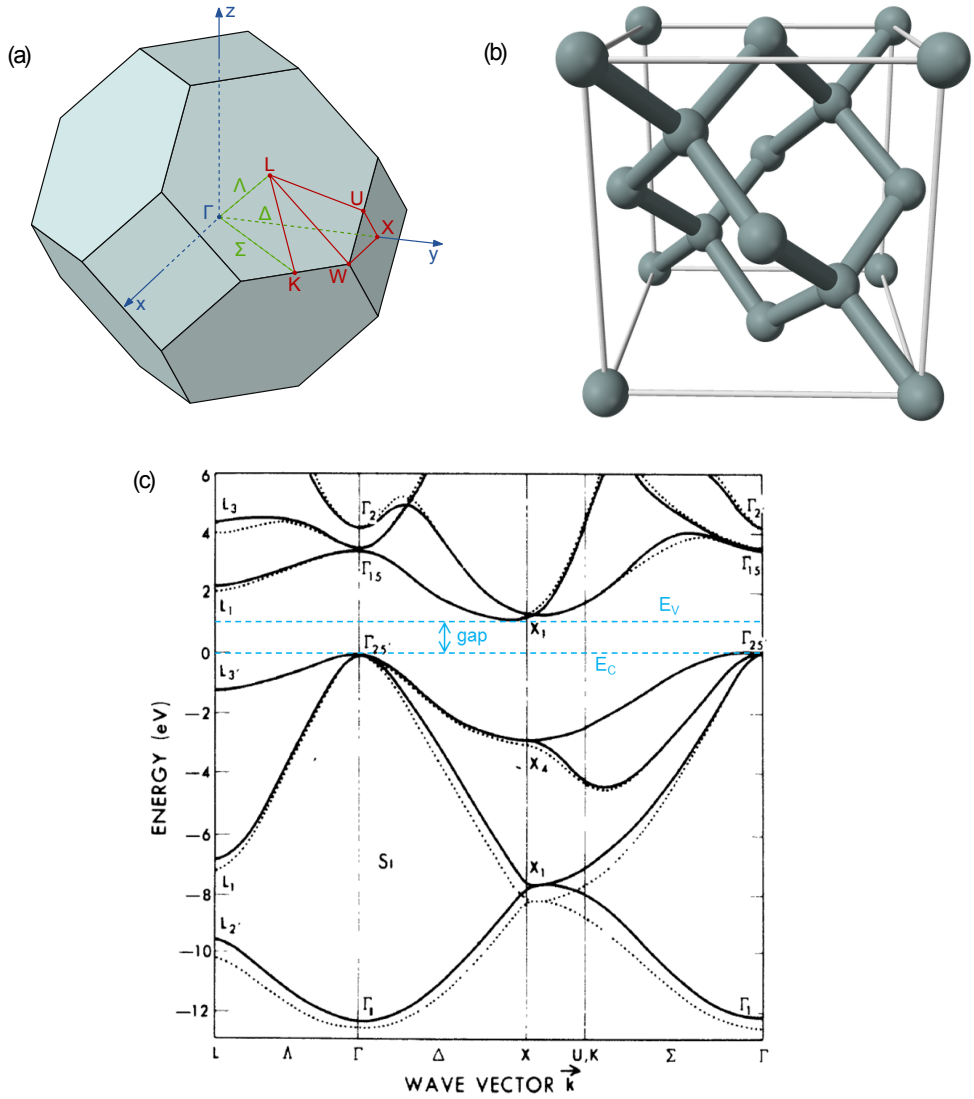

Figure 1.1 *The silicon crystal in the reciprocal (a) and real (b) spaces. (c) The silicon band structure in the first Brillouin zone. Silicon has an indirect gap of 1.12eV, with a six-fold degenerate conduction band minimum. Adapted from [15]*

spacing for the same confinement volume (see section 1.2.1). Then GaAs structures offer the possibility to built quantum devices from a relative large surface ($\sim (50\,\mathrm{nm})^2$), easily achievable with the electron-beam lithographic techniques developed on the III-V materials. This accounts for why this material has been widely used since the raise of the quantum nano-electronics field in the 90's.

Nevertheless, silicon has been chosen by the microelectronics industry as the standard material. Again the first reason is the much lower price of silicon compared to Ge, Ga or As. A unique property is the ability to reproducibly etch silicon films up to a few tens of nanometers wide without degrading its properties. This allows an excellent size control of the structures and to place them very precisely, which is essential for technological applications with the need of devices integration. Furthermore, silicon also benefits from

the presence of silicon oxide (SiO_2) layers, which don't present much charge noise and can be tuned up to a few nanometer thickness. Hence one can induce very large electric fields thanks to electrodes located very close to the channel, which allows to increase and to vary the carrier density on a larger scale than in GaAs (from 10^{11} to $10^{13}\,cm^{-2}$ in Si instead of 10^{10} to $10^{12}\,cm^2$ in GaAs), counterbalancing the smaller mobility and without the raise of gate leakage thanks to the oxide layers. Most of III-V devices were instead using Schottky barriers, which are nice to gate devices but result in poor Ohmic contacts and kill the mobility . Finally, doping is an essential and inevitable point of semiconductors industry. The high mobility of GaAs heterostructures vanishes if dopants and carriers are too close from each other. Again, silicon is much more attractive since the doping can be more easily controlled. The examples of the p-n junction, the most basic electronics component, and of the works devoted to the Tunnel-Field-Effect-Transistor justify this last point.

Silicon has also intrinsic characteristics which are very useful for quantum applications. First, its most abundant isotope[1], ^{28}Si, has no nuclear spin. Nuclear spins cause a fluctuating (in space and time) magnetic field, which is a source of decoherence for electron spins. ^{28}Si can also be purified up to 99.92% to remove the remaining nuclear spins. Secondly, silicon presents a weak spin-orbit and piezo-electric coupling. Thus the decoherence arising from the coupling between the spins and phonons is also reduced in silicon.

Therefore we understand that silicon can be a good candidate for quantum nanoelectronics devices, at the cost of efforts in term of devices size reduction to go from the classical to the quantum regimes. We will now see that the microelectronics industry also pushes the CMOS technology to the limits of about 5 nm. At this scale, several parasitic quantum effects arise, which we will develop in section 1.2.2.

1.1.2 Introduction to the SOI transistor and the CMOS technology

We first remind the basic principles of the transistor. A transistor is a current switch, controlled by an external voltage. It is composed of three parts, called electrodes: the emitter (E) and the collector (C) between which the current can flow and the base (B) which acts as the controller. The invention of the transistor is usually attributed to the Bell labs in 1948, although other groups in the world independently obtained similar results[2]. Bardeen, Brattain and Schockley measured the current flowing between three layers of appropriately doped germanium. They showed that the current in one electrode (between B and E), under certain polarisation conditions, influences the current in the others (usually between the emitter and the collector): the TRANSfer resISTOR was born[3][6]. It can also be used as an amplifier when there is gain, *i.e.* when the output

[1] silicon has three stable isotopes: ^{28}Si (92.2% of natural silicon), ^{29}Si (4.7%) and ^{30}Si (3.1%). Only ^{29}Si has a nuclear spin, with $I = 1/2$.

[2] for an interesting after-war story, consult: http://spectrum.ieee.org/semiconductors/devices/how-europe-missed-the-transistor

[3] Bardeen, Brattain and Schockley were awarded the Nobel prize in 1956 for this invention. Moreover Bardeen is the only person who was awarded two Nobel prizes in physics: he received his second one in

power (between E and C) is larger than the input power (between B and E).

A full zoology of different transistors, with different techniques, materials and applications, has followed this breakthrough. We will only focus on the most commonly used transistor in microelectronics and which is going to be at the heart of this thesis: the Metal-Oxide-Semiconductor Field-Effect-Transistor (MOSFET) done on Silicon-On-Insulator (SOI). A TEM view is represented in Fig 1.2. Two regions, called source and drain (called SD throughout the manuscript) are heavily doped (n or p). The single-crystal channel, which lays on a thick Buried OXide (BOX) can either be undoped or counterdoped, meaning p if SD are n and reversly n if SD are p. The current flowing between SD is controlled by a gate, isolated from SD and from the channel thanks to an insulating layer. Thus no current should flow from the gate towards SD.

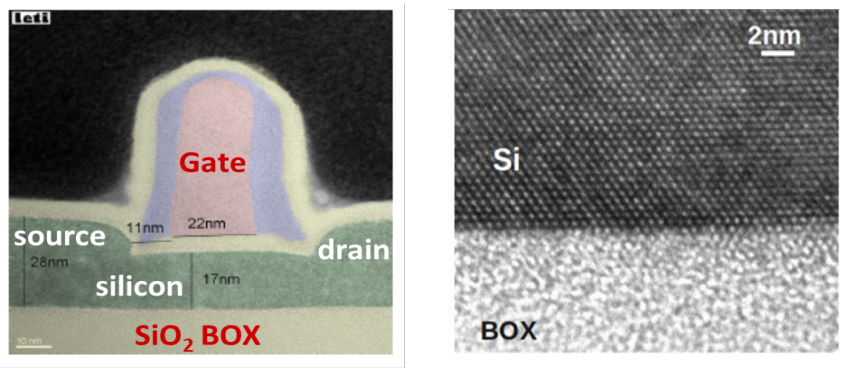

Figure 1.2 *TEM views of a SOI-MOSFET. (left) cut along source-Drain. (right) zoom on the BOX interface, which shows a good crystalline quality.*

1.1.3 CMOS technology

In order to built any electronic component and circuit, the transistors have to be linked in a proper way . This is done using the Complementary Metal Oxide Semiconductor technology (CMOS). The term "complementary" stands for the need for n and p-type devices, which act as opposite logic input/output gates: n and p-type devices have the same characteristics, described below, for opposite gates and SD voltages. The SD current should as low as possible at $V_g = 0V$ and maximum at $V_g = +1.2V$ (resp. $V_g = -1.2V$) for a n-MOS (resp. p-MOS). In this manuscript we will only focus on n-type devices but it has to be noted that p-types are essential for logic operations: we give as example in Fig 1.3 the example of a inverter involving two transistors. If V_g is "high", the p-transistor is closed and the n-MOS open, $V_{out} \sim 0$ and if Vg is "low", the p-transistor is open and the n-MOS close, leading to $V_{out} \sim V_d$.

Once a transistor has been fabricated, many steps remain to be done before connecting a sample to the "outside" world. First a Si cap layer is deposited on the sample, which prevents any aging or oxidation effects from occurring. Secondly the source, drain and gates electrodes must be connected from the doped regions to the top of this capping

1972 for the famous Bardeen-Cooper-Schrieffer theory of superconductivity.

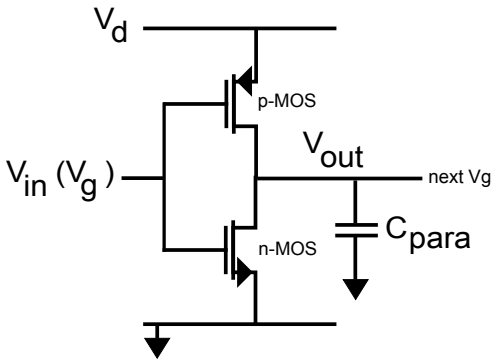

Figure 1.3 *Scheme of an inverter, the most basic CMOS logic component with one n and one p-MOS.*

layers, in order for the sample to be measured. This includes metallic lines and bonding pads. All these elements can be identified on the picture of Fig 1.4. A crucial point to fulfil for microelectronics is a perfect process reproducibility. As billions of transistors, built on the same process, have to work together and as millions of identical processors are then sold all over the world, it is obvious that one must insure that this process is highly reproducible. Samples are nowadays fabricated on 300 mm Si wafers. Each one is divided into dies (around 150), which go through the exact same process and then contain the same devices[4]. This allows to perform statistics on the exact same device from die to die and also to study the influence of the fabrication parameters (doping level, geometries). A further explanation on the working principles of a wafer is given in Appendix A.

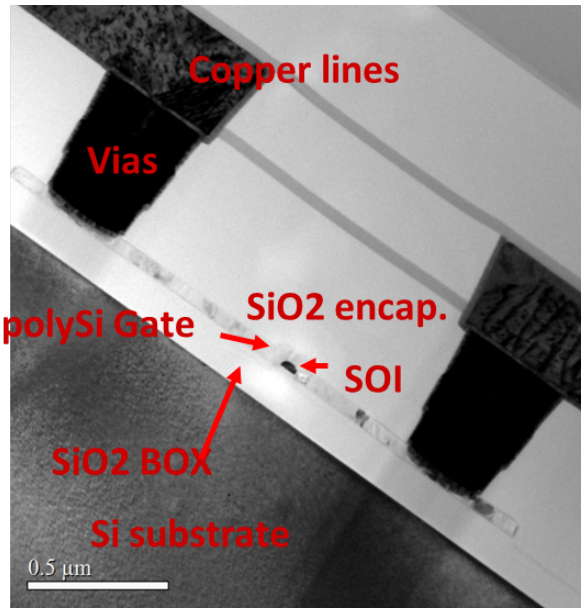

Figure 1.4 *Large TEM picture of a sample with the nanowire in the middle, including the vias and copper lines.*

[4]A die has approximately the size of processor and can then contain up to a billion of transistors. Our wafers, considered as tests before industrial processing, rather contain a few thousands of samples per die.

1.1.4 Fabrication of SOI-MOSFETs

We describe here using Fig 1.5 the main fabrication steps used by the microelectronics to create a SOI-MOSFET. The whole fabrication is performed by the LETI in Grenoble. We first start from an undoped SOI substrate, consisting of a thin silicon film (a). This film can be lightly doped or not (b). A Deep Ultra-Violet lithography with 193 nm wavelength. Then the film is etched to the desired sizes: we are able to achieve up to 5nm-diameter nanowires. An oxide layer is deposited on the film and then the gate (c). Si_3N_4 spacers are deposited around the gate, followed by an epitaxy of the silicon channel to create the SD. These are then doped above the Mott transition with arsenic atoms (with a concentration of $10^{20}\,cm^{-3}$) (d). These two last steps are repeated a second time in order to obtain an optimal gradient (about 1 order of magnitude in conentration/5nm) of the doping from the SD to the core of the channel (e). The dopants are activated thanks to an annealing at 1400 °C for the SD to become metallic-like. This step induces a dopant diffusion, which we will developp in Chapter 4. Finally these contacts are silicided with Ni to form an NiSi alloy which decreases their resistance.

Almost all of the parameters are adjustable: the presence of doping (n or p) and its dose on step (a), the thickness (T_{Si}), width (W) and length (L) of the channel, the presence of spacers, their widths (15 or 40 nm). The material used for the gate oxide and for the gate itself can also vary.

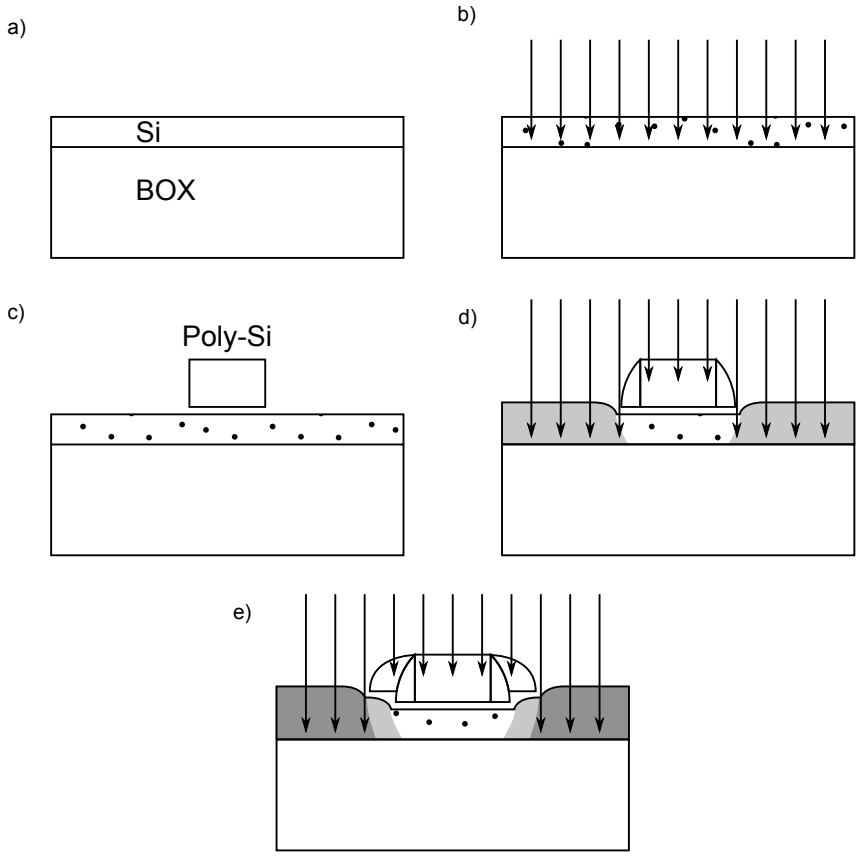

Figure 1.5 *Main fabrication steps (see main text). Adapted from [93]*

1.1.5 Room temperature characteristics

We present on Fig 1.7 the characteristics of such a transistor, which is the measurement of the SD conductance for a small bias voltage ($V_d = 1\,mV$). The channel is undoped (with no light doping under the spacers, which are 40 nm wide), its dimensions are $L \times W \times T_{Si} = 40 \times 60 \times 12\,nm^3$.

- For negative value on the gate voltage (called V_g), the current is exponentially increasing with V_g: $G_{sd} \sim \exp(-\alpha e(V_g - V_{th})/k_B T)$, called **thermally activated regime**. α expresses the potential difference $d\phi_{ch}$ in the channel when the gate voltage is swept:dV_g: $\alpha = d\phi_{ch}/dV_g$. It can be expressed as a function of the capacitances depicted on the sketch of Fig 1.6

$$\boxed{\alpha = \frac{C_g}{C_s + C_d + C_g + C_b} \approx \frac{C_g}{C_s + C_d + C_g}} \tag{1.1}$$

  Due to the thick BOX layer (145 nm) compared to the thin front oxide layer (5 nm), we usually have $C_b \ll C_g$. The blue curve, fitting this regime, gives directly access to this α parameter. We find here $\alpha = 0.51$. This has to be compared with the green slope, which would design the thermally activated regime for an ideal transistor ($\alpha = 1$ at room temperature (the maximum slope equals $\frac{k_B T}{e}\ln(10)$=60 mV/decade). This control on α is crucial and will be improved as we will see in section 2.1.1.
- G_{sd} is linear as a function of V_g, called **the linear regime**. A channel is formed under the gate. Supposing a constant mobility and a 2D density of states, hence constant with the energy, we obtain a linear increasing accumulation of carriers with the gate voltage.
- the transistor reaches a **saturation regime**[5], mostly due to the access resistances R_a.

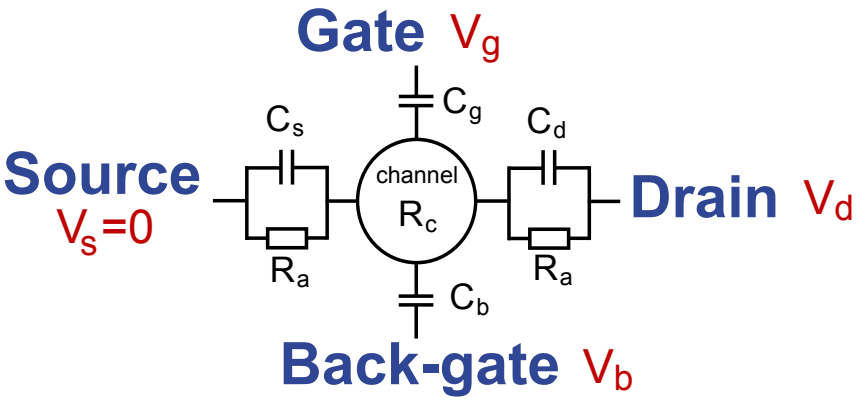

Figure 1.6 *Electrical equivalent circuit of a MOSFET. The current flows between Source and Drain and the channel is capacitively coupled to the front and the back gates. By convention, we consider the source as grounded* $V_s = 0V$.

[5] those terms have slight different definitions in microelectronics, as the sweep parameter is usually V_d and not V_g. The saturation regime is then reached when $V_d \approx V_g$ (called the pinch-off), when no carriers stand between the gate and the drain.

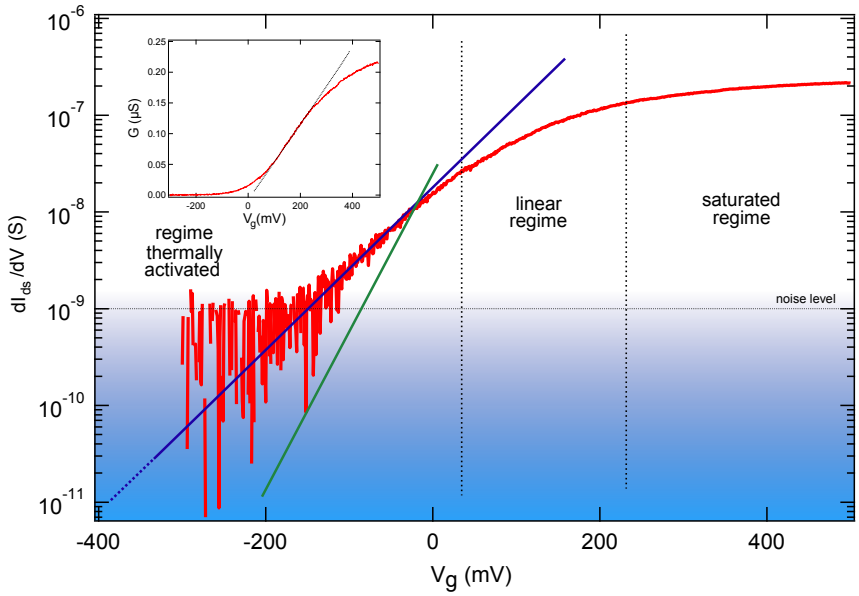

Figure 1.7 *Differential conductance vs.* V_g *at 300K for a typical MOSFET. Three regimes can be identifies: a thermally activated regime, with an exponential dependence of the conductance, a linear and a saturated regime. Inset: the conductance plotted in linear scale showing the linear regime range.*

1.2 Single electron dots in silicon MOSFETs

1.2.1 From Field Effect Transistor to Single Electron Transistor

We have seen the main characteristics of a modern CMOS transistor at room temperature. We will now investigate its behaviour when we cool down the sample in order to get rid of the temperature broadening and furthermore to reveal the single electron physics lying in those nanostructures.

If one wants to control and manipulate electrons one by one, the first step to achieve is to be able to isolate electronic wavefunctions. This can be done through the realization of single electron transistors, where electrons are confined in a region of space. This region, usually called the dot, is then linked to the environment through the tunnel barriers. We first quickly give the basics of the working principles of single electron dots, using the Fig 1.6.The electrostatic model gives the energy to add an electron in the dot, which is called the charging energy E_C and is expressed as a function of the capacitances of the device:

$$\boxed{E_C = \frac{e^2}{2C} \; with \; C = C_s + C_d + C_g + C_b} \tag{1.2}$$

We can also derive the total energy of a dot with N electrons E(N) as a function of the gate voltage, assuming that no bias is applied between SD ($V_d = 0$) and no offset charge is present:

$$E_N(V_g) = \frac{E_C}{2}\left(N - (\frac{C_g V_g}{e} + \frac{C_b V_b}{e})\right)^2 \tag{1.3}$$

Two conditions are necessary to discretize the filling of the dot, where electrons enter the dot one by one. First, the temperature has to be lower than the charging energy. Taking C = 50aF, this leads to:

$$\boxed{T < \frac{E_C}{k_B} \approx 40K} \tag{1.4}$$

Secondly the tunnel barrier should be opaque enough in order to ensure a sufficient electron confinement. This can be understood with the Heisenberg uncertainty principle. Adding an electron in the dot requires to pay the charging energy E_C. This electron will enter (or escape) the dot within a time given by $\tau \sim 1/\Gamma \sim RC$. (we take here for simplicity $R_s = R_d = R$ and $C_s = C_d = C$). The Heisenberg principle leads to a energy uncertainty ΔE over this time given by $\Delta E \sim \hbar/\tau$. For the state with an extra electron in the dot to be well defined, one needs to check that :

$$\frac{\Delta E}{E_C} \ll 1 \Rightarrow \boxed{R \gg \frac{\hbar}{e^2} = R_q} \tag{1.5}$$

We find that the access resistance should be higher than the quantum of conductance $R_q \approx 25.2\,k\Omega$. This is of the same order of magnitude resistances observed in our device, as shown on Fig 1.8. Then we cooled down this device down to 400mK in a dilution fridge with filtered DC lines and measured its conductance as a function of V_g with $V_b = 50V$. A dot can be created in the channel for positive V_g, with the potential in the channel lying under the Fermi energy defined by the SD, and depleted for negative V_g (see Fig 1.8(a)). Indeed we can observe a strong modulation of the current on a large V_g range (Fig 1.8(b)), corresponding to conductance oscillations, as seen in (c), which are the sign that the transistor is in the single electron regime. A peak in the conductance is measured for the gate voltage V_g^N corresponding to the degeneracy between the energies of the dot with N and N+1 electrons: the electrochemical potential $\mu(N)$, defined as the energy difference between N+1 and N electrons equals the Fermi level (Fig 1.8(c) and (d), red cross) [36]:

$$\mu(N) = E_F \Rightarrow E_N(V_g^N) = E_{N+1}(V_g^N)$$

$$E_N(V_g^N) = E_{N+1}(V_g^N) \Rightarrow E_C(N - C_g V_g^N/e)^2 = E_C(N + 1 - C_g V_g^N/e)^2$$

$$\boxed{\Rightarrow C_b V_b^N + C_g V_g^N = e(N + \frac{1}{2})} \tag{1.6}$$

On the contrary, a dip in the conductance occurs if we are out of this resonant condition (Fig 1.8(c) and (e), purple cross): it is the Coulomb blockade regime.

We see with equation 1.6 that there is a balance between V_b and V_g: if we increase V_b, we have to lower V_g by the amount $C_b V_b/C_g$ to stay at resonance with the same number of electrons in the dot. We will see in chapter 3 that this linear relation is not always valid and that we need to go beyond this model.

The 50V-bias voltage is applied on the back-gate at low temperature following the technique developed in [92]. At low temperature, the threshold corresponds to the gate

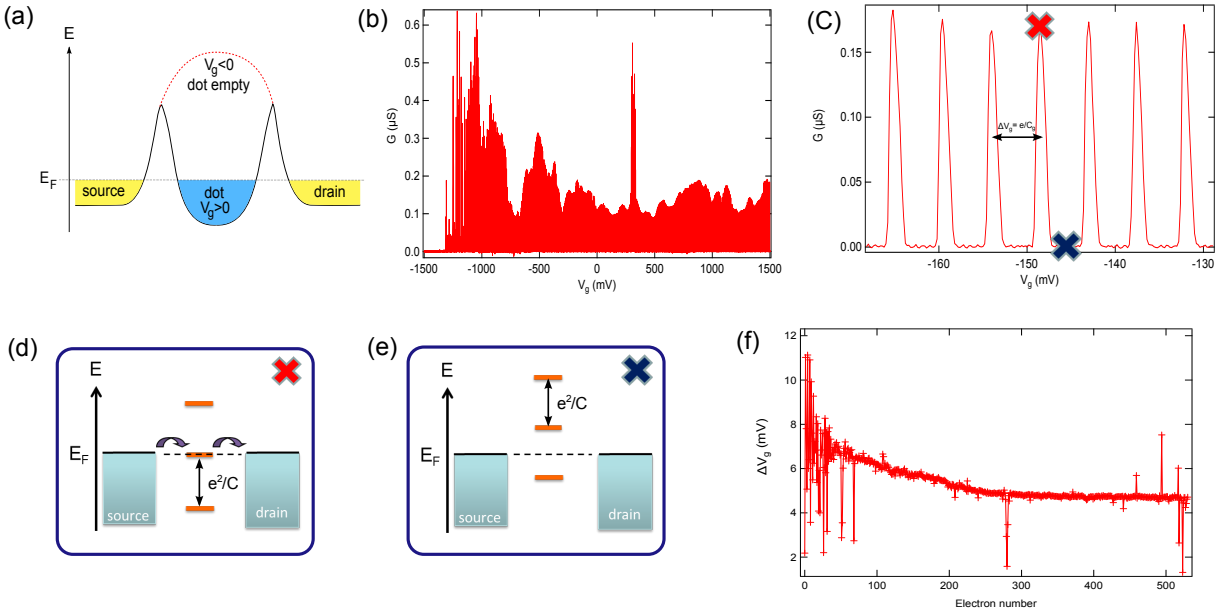

Figure 1.8 *Example of a CMOS MOSFET exhibiting Coulomb blockade at low temperature (400 mK).(a) The large spacers create the barrier which confine electrons and create the dot. (b) More then 500 Coulomb oscillations are observed on a 3 V range of* V_g. *(c)Zoom of (b) showing the regularity of the oscillations. A peak in conductance is observed when an electronic level, separated from the other by the charging energy, is aligned with the Fermi level in the SD (red cross, (d)). The current is blocked out of the resonance (purple cross, (e)). (f) The gate voltage spacing between successive resonances, extracted from (b), plotted as a function of the relative number of electrons in the dot. B.Voisin et al., unpublished.*

voltage where the first electron is put in the dot. From discussion above, applying a positive V_b should lead for the threshold voltage to be shifted towards negative values of V_g. This corresponds to what we observe: the first Coulomb peaks appear at $V_g \sim -1.3V$. However we don't induce a SET to FET transition as in [92] but we still remain in SET regime even for this high bias. This indicates that the wide and undoped barriers still confine electrons, enabling to measure and to study the peak spacing between successive resonances (called ΔV_g) on a V_g-range of 3V.

From equation 1.6 it is straightforward to see that the voltage peak spacing (keeping V_b constant) ΔV_g should be independent of N: $\Delta V_g = V_g^{N+1} - V_g^N = e/C_g$. For this sample, we observe on Fig 1.8(f) that ΔV_g seems to be constant only for high electron number ($N \geq 250$), when the dot is well formed. For smaller electron number, the peak spacing is increasing as well as its variance for $N \leq 100$. This reflects the disorder and the quantum confinement which appear in the channel and modify the capacitances of the system. This disorder is smoothed by a large number of electrons. Still we can compare the average peak spacing to the expected one from the geometric capacitance, assuming a planar model (we remind that the gate surrounds three faces of the nanowire)

$$\Delta V_g^{geom} = e/C_g^{geom} = e/(\epsilon_0 \epsilon_{SiO_2} \frac{L(2T_{Si}+W)}{t_{ox}}) = 16.6mV$$

This value is around two to three times the experimental peak spacing. The planar model

may then not be the most accurate for such a device. Nevertheless, we show here that we are able to add or remove more than 500 electrons in the dot without leaving the single electron regime. This correspond to a 2D electron density:

$$n_{2D} = \frac{N}{S} \approx \frac{N}{L(2T_{Si}+W)} \approx 1.5 \times 10^{13}\,cm^{-2}$$

Again this large electron density is the key to counterbalance the relative low mobility for the transistor. It can also induce a large screening of the disorder naturally present in silicon. A detailed analysis of the Coulomb blockade in these silicon transistors has been performed by Max Hofheinz[43] and Mathieu Pierre[79] as a function of the fabrication and geometric parameters. But if single electron dots in such CMOS devices are now well-established, they have only concerned up to now diffusive dots, where any electron entering the dot will lose its phase and spin coherence. This is obviously incompatible with the aim of manipulating the quantum properties of an electron in such a system.

We describe, following the derivation of Beenakker [8], two different transport regimes of interest for now. We need to focus on three quantities: the temperature T, the mean level spacing Δ_1, which reflects the spectrum of the quantum dot, and the tunnel rates Γ_S and Γ_D between the dot and the SD.

- **the sequential multilevel regime:** $\hbar\Gamma \ll \Delta_1 \ll k_BT \ll e^2/C$
  We are in the sequential regime as the charging energy prevents for more than one electron to populate the dot. Because of the temperature broadening, the dot spectrum can be considered as a continuum of states. Any effect of the density of states of the dot is killed. Then all the states (convoluted with the Fermi-Dirac distribution) contribute to the conductance of a Coulomb peak, which takes the following form as a function of V_g:

$$G = \frac{e^2\rho}{2}\frac{\Gamma^S\Gamma^D}{\Gamma^S+\Gamma^D}\frac{1}{\cosh^2(\frac{\alpha eV_g}{2.5k_BT})} \tag{1.7}$$

  We can note that the maximum conductance G_{max} is independent of the temperature. The Full Width at Half Maximum (FWHM) gives FWHM $\sim 4.41\,\frac{k_BT}{\alpha e}$. This was the regime studied by Hofheinz and Pierre and also concerns the sample of Fig 1.8.

- **The sequential single-level regime:** $\hbar\Gamma \ll k_BT \ll \Delta_1 \ll e^2/C$
  If we lower the temperature enough to reach this regime, then only one state of the dot can contribute to current. The conductance is given by:

$$G = \frac{e^2}{4k_BT}\frac{\Gamma^S\Gamma^D}{\Gamma^S+\Gamma^D}\frac{1}{\cosh^2(\frac{\alpha eV_g}{2k_BT})} \tag{1.8}$$

  leading to FWHM $\sim 3.53\,\frac{k_BT}{\alpha e}$. We can note the difference with e first regime in G_{max} which increases when decreasing the temperature in this regime, which is the first signature to experimentally observe.
  Hence we recover the effect of the single level spacing, which has to be added to be added to the charging energy. For instance we can consider that we put the N-th

(resp. N+1-th) electron on an state (orbital or valley) with energy ϵ^N with a spin s^N (resp. ϵ^{N+1} and s^{N+1}), the resonant condition 1.6 leads to the following peak spasing between N-th and N+1-th electron:

$$\boxed{\alpha \Delta V_g^N = E_C + (\epsilon^{N+1} - \epsilon^N) + g\mu_B B(s^{N+1} - s^N)} \tag{1.9}$$

with $g\mu_B B(s^N) = \Delta E_Z$ standing for the Zeeman energy of the state with g the gyromagnetic factor (g = 2 in silicon), μ_B the Bohr magneton and B the applied magnetic field. for s = 1/2, we find $\Delta E_Z \approx 57.8\,\mu$eV/T.

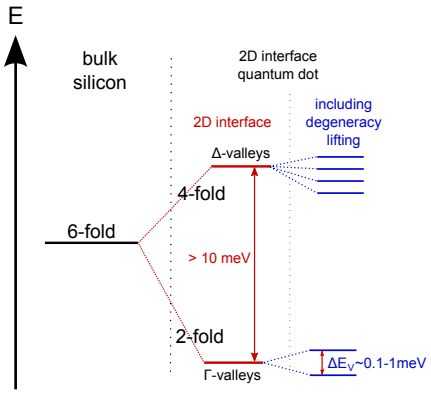

Figure 1.9 *valley splitting of a 2D quantum dot.*

We can calculate the mean level spacing Δ_1 (or spectrum) of a 2D dot of a surface S:

$$\Delta_1 = \frac{2\pi\hbar^2}{d_{spin} d_{valley} m^* S} \tag{1.10}$$

When the electrons are confined in two dimensions, the valley degeneracy is partially lifted into a four Δ-valleys lie tens of meV above a two Γ-valleys. These two Γ-valleys can further be lifted with an electric field and is also related to the interface intervalley scattering, very sensitive microscopic details of the interfaces [4, 96] (see Fig 1.9). We will discuss and develop these two points in the Chapter 2. Here we take $d_{spin} = 2$ and $d_{valley} = 2$. m^* represents the average effective mass ($m^* = \sqrt[3]{m_t^2 m_l} = 0.32\,m_e$) and S the area of the dot. One obtains: $\Delta_1 = 1$ meV for an area of $20 \times 20\,nm^2$. This value wasn't achieved in these previous samples and therefore no spectroscopy of the dot was possible.

1.2.2 Challenges for microelectronics...

The semi-conductor is one of the world biggest industry, representing a annual market of more than 300B$. This deserves a careful study of its advances and future objectives, which is done in an international consortium including the leading chip manufacturers. It is called the International Technology Roadmap for Semiconductors (ITRS), delivering a bi-annual report[73].

The general trend of the microelectronics industry has been identified in 1965 by G.E. Moore, who empirically predicted what is now often called Moore's law. It can be easily summarised with the following idea: "Every quantitative parameter doubles every two years". As examples we detail on Fig 1.10 the number of transistors per processor, the price of a single transistor and the clock frequency in the last decades.

This constant evolution of microelectronics is guided by the following reasons. There is a constant demand for more and new functionalities in our electronic devices. This deserves a constant effort in the integration schemes of the transistors: more transistor within the same volume and an improved architecture. These devices also need to be

as cheap as possible, and of course, low energy consuming. These reasons seem rather practical but they have had strong impact on the design of the transistors to fulfil these conditions. We can take as examples three parameters characterizing a circuit.

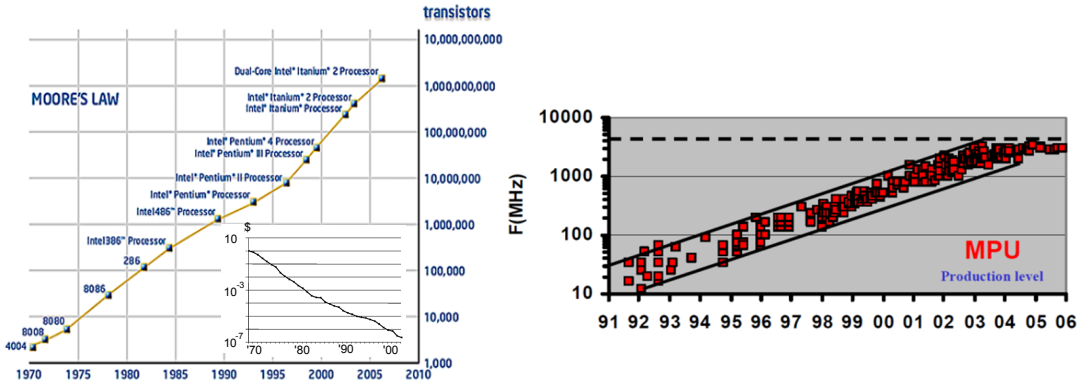

Figure 1.10 *Illustrations of Moore's law. (left) The number of transistors in different processors. Inset: average cost of a single transistor. (right) Driving frequency of processors.*

We simply consider a transistor as a RC circuit. The resistance R and the capacitance C include both the transistor and the interconnects. The resistance of the transistor is simply given by the ratio of the bias voltage (V_d) over the on-current (I_{on}).

- **The clock frequency f.** We can express it as $f \sim 1/RC$. To increase this frequency, one should then decrease the capacitances an resistances of the system. This goes towards a reduction of the transistor dimensions, especially the length[6].
- **The static power P_{stat}.** This power is due to the leakage current when the transistor is off ($V_g = 0V$). Then we have the relation $P_{stat} \sim RI_{off}^2$. This should correspond to a region where the transistor is in the thermally activated regime, controlled by α. The more α is close to one, the steeper will be the slope and the lower will be I_{off}[7]. In that respect the sample presented on Fig 1.7 would be a really poor transistor, as its threshold voltage is around 0 (then we are not completely in the thermal regime) and its alpha factor is poor (0.51).
- **The dynamical power.** This denotes the needed power to switch the transistor at the clock frequency: $P_{dyn} \sim CV_d^2 f \sim V_d^2/R$. As we can observe, a decrease in the resistance which would beneficial in the two previous parameters would here increase the dynamical power and deteriorate the performance of the transistor. Instead, the direction is towards a reduction of the bias voltage, from 1V to around 0.5V. This implies more drastic requirements on the I_{on}/I_{off} ratio, which must be kept above 10^5.

[6]Note that a decrease of the width implies a increase of the resistance R, which should be avoided and must be counterbalanced.

[7]Intense efforts are also currently made in order to completely switch the unusued parts of a electronic circuit at a time t, with then truly $I_{off} = 0$.

We now explain how these requirements have been implemented on the technological side. As we have already mentioned, one key is the miniaturization of the transistors, in order to increase the number of devices per area. The ITRS road-map has planned this reduction with steps to reach for the technology. Currently, the 22-nm generation (devices with 22nm gate length) is on production and the 14-nm node is still under research. This reduction of the gate length has to be accompanied by a scaling of the other geometrical dimensions of the devices to keep constant electric fields in the channel (approximately W $\sim$ 3L). This geometric scaling of the device and an increased device integration result in smaller capacitances, which is good for the clock frequency and the dynamical power. To decrease $I_{off} = 0$ and the static power, we need a better α parameter, meaning to increase the gate capacitance with respect to the SD capacitances. This is done using other oxides than the usual SiO_2 ($\epsilon_r = 3.9$) with a higher dielectric constant, as HfO_2 ($\epsilon_r = 25$) or HfSiON ($\epsilon_r = 14$) as instance in Fig 1.11. One can now include a stripe of TiN, to increase the threshold voltage to ~ 0.5V (due to higher working functions) and decrease I_{off}. These high-k dielectrics also allow to reduce the tunnel current which would be strong for an equivalent capacitance made in SiO_2, which would deserve $t_{ox} \approx 1.5$nm. Efforts have also been made to improve the access of the device thanks to a better control of the doping regions in order to obtain low access resistances. One can also include strain in the silicon (for example by incorporating germanium) in order to modify the crystal band structure and to increase the channel mobility.

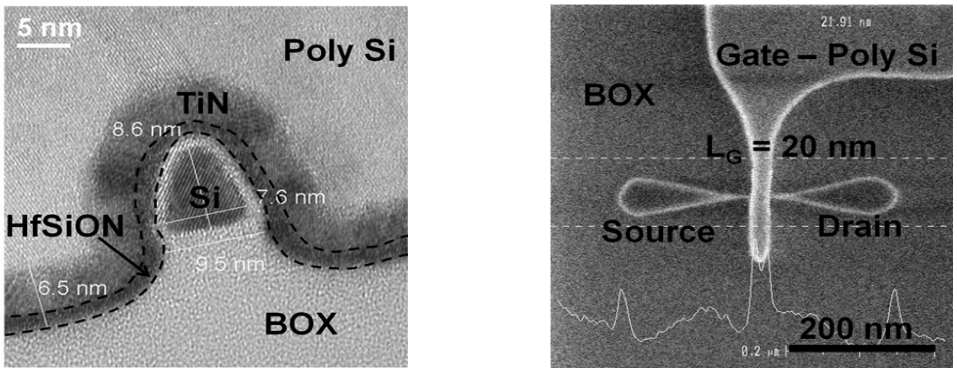

Figure 1.11 *TEM views of a modern MOSFET transitor made by LETI. (left) Cut view along to see the nanowire, the high-k dielectric and the TiN gate which surrounds the nanowire for an excellent electrostatic control on the whole channel. (right) Top view before spacer deposition. We can see the aggressive etching to create the channel (under the gate) while keeping relatively large access region on its side (source/drain) to ensure low access resistances. Adapted from V. Deshpande [20].*

Shrinking these devices to the nanometer scale also brought drawbacks. First, the use of a thin oxide layer to decrease the capacitances also allows leakage current to flow from the gate to the SD (even if counterbalanced with the use of high-k). This current, proportional to the gate area, enhances the static power. Secondly, direct tunneling can occur between SD because of the very small gate length. We can develop this point thanks to the scheme presented on Fig 1.8(a), where the device is supposed to be in its off-state. We therefore consider the channel as a barrier of length L (gate length, taken as 20 nm) and of height E_B (of the order of 100 meV). The thermionic current which will

flow between SD is only due to the hot electrons whose energy k_BT is higher than the barrier height E_B. Hence it is independent on the barrier length but is proportional to $\exp(-E_B/k_BT)$. On the other side, the tunnel current flowing through the barrier is proportional to $\exp(-\sqrt{E_B/2L})$. Decreasing the gate length will enhance this tunnel current and it actually becomes dominant for $L < 10\,nm$ [81]. An other drawback, known as short channel effects, is the lack of control of the gate on the channel for very short devices, due to the tunneling between SD through electric field lines deep in the substrate. For this point the SOI technology presents a serious advantage: the BOX pulls up all these electric field lines towards the front gate interface. We take as an example the recent Ultra-Thin-Body-and-Box MOSFET (UTBB-MOSFET) which has been developed in a collaboration between STMicroelectronics and the LETI. Its main advance is to use a thin buried oxide ($\sim 25\,nm$) and a very thin silicon channel ($\sim 6\,nm$) and to use the back-gate as a second gate. These dual-gate devices allow to maintain a perfect control of the device electrostatics, even for ultra-scaled gate lengths.

At this scale, the position of any dopant is crucial and can strongly affects the room temperature characteristics of a transistor. This effect, known as Random Dopant Fluctuations, has been numerically studied by Asenov [5] and experimentally demonstrated by Pierre *et al.* [63] with the transport through a single atom (see section 1.3.3). We will extend his work on Chapter 3. This causes an enhanced variability of the process and microelectronics therefore intensively work towards an atomic control of the dopant.

Finally, confinement effects can occur as the actual device size become comparable to the Fermi wavelength ($\lambda_F = \sqrt{\frac{d_{spin}d_{valley}\pi}{n_2D}} \sim 5\,nm$), added to the surface roughness of the interfaces which also becomes an issue. Those two effects can result in stochastic Coulomb blockade, even at room temperature, due to the quantization of the energy levels.

All these considerations have only concerned the transistor itself, which will be the focus of this work. One other major issue is the interconnections between the different parts and transistors of a circuit, as illustrated on Fig 1.3 with the parasitic capacitance C_{capa}.

1.2.3 ...opening opportunities for nanoscale physics

We have seen that the microeletronics has developed outstanding fabrication processes. This evolution has been led by a constant hunt for an excellent electrostatic control over a small volume of silicon, without degrading its physical properties. It is then possible to tune the electric field and the electron density on a very large scale in this system, thanks to the presence of nearby gates and thin oxides layers. This represents a unique opportunity to control quantum objects (quantum dot, single donor) on such small scales, with an already steady integration scheme. Recently the first electron of a quantum dot in a MOSFET of size $20 \times 20 \times 8\,nm^3$ was measured by Prati *et al.* [84]. We will continue this work and characterize the first states of such state-of-the-art transistors in Chapter 2.

Furthermore, the search for ultra low power consumptions can be expressed as the number of electrons involved to charge such a device. Taking the values of the capacitances ($\sim 100fF$), the resistance ($\sim 1k\Omega$) and the bias voltage ($V_d = 1V$) of a modern

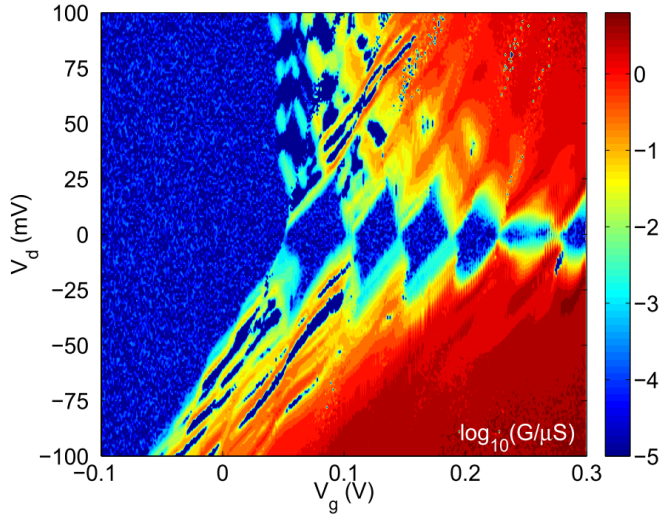

Figure 1.12 *Measurement of the first electron in CMOS MOSFET. Extracted from [84]*

transistor embedded in a circuit, we can calculate N as $N = CV_d/e \sim 625000$ with a resulting energy of approximately 10^{-17} pJ. A commonly accepted goal for 2020 is to reduce this number up to N = 10000. But we have also seen that room temperature single electron transistors also come into play. The ultimate goal would then to build full electronics controlled by the displacement of single electrons. The Heisenberg principle will illustrate that we are not so far to reach the quantum limitation of such a switch. We take an imaginary SET which would work at room temperature (*i.e.* $C \approx 1\,aF$ and $R \approx 100\,k\Omega$ to satisfy the conditions (1.4) and (1.5). We would obtain $\frac{h}{RC} \sim 40meV \sim k_BT$ at 300 K, which represents a fundamental limit for the transistor. Actually and despite these answers to technological issues, the ITRS road-map plans that no improvement in term of size reduction (up to 5 nm) will be possible within this technology after 2030, essentially due to the quantum confinement and leakage effects at this atomic level. This allows nowadays to tackle quantum physics in these modern transistors which will lead to new concepts taking advantage of these revealed quantum properties.

We have also seen that new materials as high-k dielectrics and metals for gates have appeared in the nowadays device fabrication. Actually many others new type of devices are getting developped, usually dedicated for specific operations. For instance we can cite InAs or graphene channel transistors for high frequency operations. Their control as well as their coupling and embedding with the rest of a CMOS circuit also represent a very stimulating challenge.

1.2.4 Realizations of Si dots

We review in this section some of the most important realizations concerning silicon-based single electron devices. It will demonstrate the tunability of silicon as these works rely on almost all fabrication techniques commonly used in semi-conductor physics.

Etched channel structures
We start with works using etching techniques close to ours. We can first note the group of Rogge in Delft (now at the UNSW, Australia), working on very similar MOSFET devices fabricated in IMEC, Belgium. They especially focus on dopants in these devices and therefore we will develop their work afterwards. We can also note the work of Nordberg *et al.*[72], who also measured Coulomb blockade oscillations in a MOS structure made in a CMOS compatible foundry. The group of Fujiwara in NTT, Japan also defines their structure using the SOI technique [29]. Compared to a classical MOSFET, they use an upper gate on the nanowire to create a 2D channel. Then they use three local gates, two on the sides to create the barriers and a central one to sweep the energy levels of the dot.

2DEG in bulk silicon
The first signatures of Coulomb blockade were originally observed in silicon, by Scott-Thomas *et al.* in 1989 [100]. They used two stages of gates (lateral gates and an upper gate). The group of A. Dzurak also starts from bulk silicon to create a quantum dot[61]. They use e-beam lithography and thermal evaporation to create Al gates, separated by thin aluminium oxide layers. The final structure is similar to [29] previously mentionned, with the presence of an upper gate to create a 2DEG, then depleted thanks to side gates to create the dot and a plunger gate to control the energy levels of the dot. The ohmic contacts are far away from the dot (contacted by the 2DEG), which allows to get rid of fluctuating density of states and allows an easier spectroscopy.

Nanowires
It is also possible to grow Si nanowire using a vapor-liquid-solid process. It is the method used by Zwanenburg *et al.*[123] to obtain nanowires of diameter 5-8 nm. They define the dot using salicidation of the nanowire, which results in Schottky barriers. Thanks to these small dimensions, they were able to observe the spin filling of the first four holes. However it remains challenging to embed these nanowires in an integration scheme and doping is difficult.

Dot with Si as base ingredient
Many others structures use silicon as a substrate or in combination with others materials. We can for example cite the contacts of self-assembled SiGe grown on silicon dots by Katsaros *et al.*[48] or the heterostructure created from SiGe layers [12]. Gating these devices remain quite challenging in both cases and doping is also difficult.

Finally, a unique technique has been developed at the University of New South Wales in Australia. They pattern a quantum dot by removing the dandling bonds of a high quality passivated Si:H surface with a STM tip and then evaporate phosphine in order for single P atoms to replace the missing bonds. These atoms are then activated thanks to the etching of Si on top of the surface and to an annealing step ($\sim 350\,^{\circ}\mathrm{C}$). This technique allows for an atomic precision of the quantum dot (location and size) and undoubtedly represents an innovative path towards the control of single dopants in silicon, which will

be the focus of the next section. However, because of a massive dopant diffusion, these structures don't resist to high annealing (above 1300 °C which would be needed in a CMOS-compatible technology with the use of oxide layers to induce large electric fields without leakage.

Top-down approach

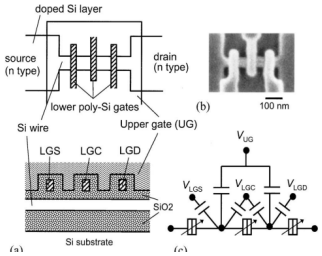

Silicon-On-Insulator device
From Fujiwara *et al.* []

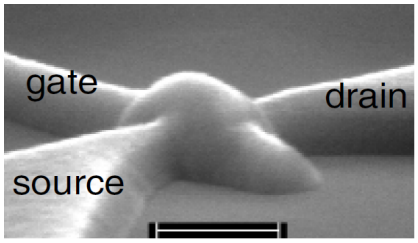

FinFET device made by IMEC, Belgium
From Sellier *et al.* []

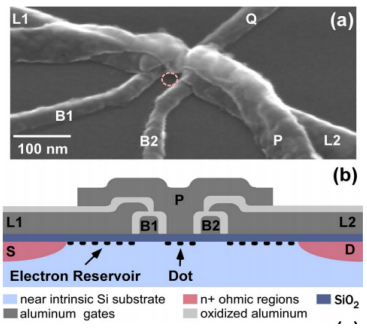

2DEG formed with Al gates
From Lim et al. []

Bottom-up approach

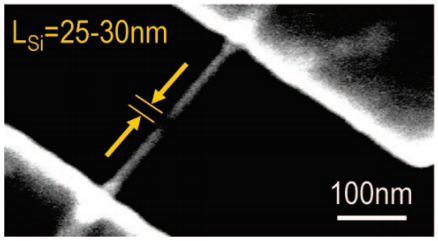

CVD grown nanowire with NiSi access
From Zwanenburg et al. []

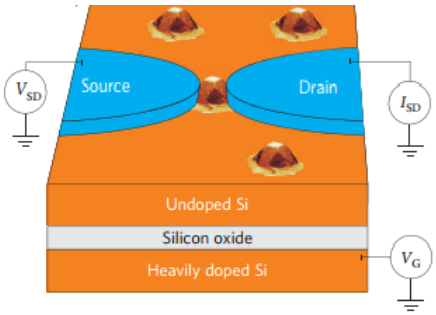

Self-assembled SiGe nanocrystals
From Katsaros et al. []

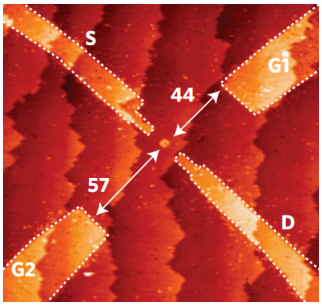

STM patterned Si:P dot
From Füechsle et al. []

Figure 1.13 *Different realizations of silicon nanoeletronic devices described in the main text.*

1.3 Single dopant physics

1.3.1 Interests of dopants in semi-conductors

Doping is an essential ingredient of the microelectronics and more generally of all the semi-conductor physics. The bulk properties of doped semi-conductors have been investigated since the 50's: doping allows to adjust the Fermi level and one can also induce the Mott transition [67], going from a semiconducting to a metallic behaviour. As an example, one has to dope silicon with an arsenic (n-type) concentration above $8 \times 10^{18}\,\mathrm{cm}^{-3}$ to induce this transition, allowing to create the SD of a transistor.

The recent developments of semiconductors fabrication also allow to purify almost any material to get rid of most of its natural impurities. Together with the size shrinking of solid-state devices and an improved control of the doping process, we are nowadays able to build single-atom devices. Indeed, dopants represent the ultimate quantum objects one can consider in solid-state matter and many proposals have bloomed this last decade to use their essential discrete properties for innovative quantum applications [50]. This includes for example quantum information, using the nuclear spin of a phosphorous donor as a quantum bit [47] or the realization of single photon sources thanks to NV centers in diamond [55] or with Mn atoms in (II-V) quantum dots [9], illustrating the large panel of systems in which the single dopant physics can be tackled.

We point out in this section the main properties of a single donor in silicon. We will see how their spectrum evolve from the bulk to a full nanostructure with the presence of a close local environment, essential in order to electrically contact and further control and manipulate them, points which will be addressed in the next chapters.

1.3.2 Spectrum of a donor: from bulk silicon to a nanostructure

In bulk silicon

Following Moores's law and the size reduction of transistors, the number of dopants inside a channel has also decreased these last decades up to a few atoms in the channel. The case of microscopic doped semi-conductors has been largely studied during the last decades. Without being exhaustive, we can cite some important works during this period: Mott studied the metal-insulator transition [67], Efros and Schklovskii the electronic properties of doped semi-conductors [22, 23]. Abrahams *et al.*[8] developed the theory of localization [2, 3]. These works represent the foundations of the mesoscopic and nanoscopic physics which have raised in the 90's with for example the experimental evidence of universal conductance fluctuations by Skocpol *et al.* [106]. It has now even become possible to observe single dopant effects in these ultra-scaled devices, as developed further in this section.

We describe here the properties of a single dopant in bulk silicon and in a nanostructure. We only focus on donors, with one extra valence electron compared to silicon. Kohn and Luttinger first consider this donor as a positive charge and derived the electronic

[8] "The gang of four"

states of an electron using the effective mass energy model [51]. Hence they obtained the following results:

$$E_I = \frac{m^*}{2}\left(\frac{e^2}{\hbar\epsilon_0\epsilon_{Si}}\right)^2 \approx 29\,meV \tag{1.11}$$

$$a_B = \frac{h^2\epsilon_0\epsilon_{Si}}{\pi m^* e^2} \approx 1.8\,nm \tag{1.12}$$

Six wave functions, separated in three subgroups A1(1-fold), T2(3-fold) and E(2-fold), are associated with the ground state (1s-like) in order to reflect the symmetry of the silicon crystal. But this model doesn't reflect the experimental data which show for instance a dependence on the chemical species. One actually has to take into account central-cell-corrections where the deep potential confinement induces valley-mixing. This is especially true for 1s(A1), whose is the only ground state wave function whose probability density is maximum on the nucleus. Further studies [90], confirmed by optical absorption experiments, showed that the splitting of these subgroups, leading to the valley-orbit splitting. We summarise the values of these energies (in meV) and degeneracies (excluding spin) in Fig. 1.14.

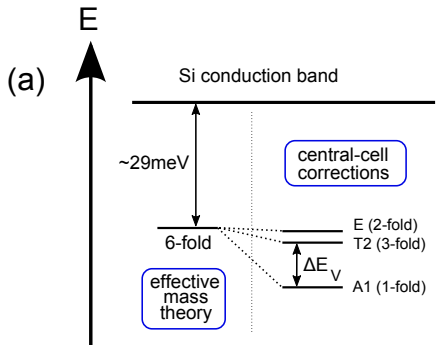

(b) in meV

Level	P	As
$1s(A_1)$	45.59	53.76
$1s(T_2)$	3.89	32.67
$1s(E)$	32.58	31.26

Figure 1.14 *(a) Valley degeneracy lifting of the ground state (1s) of a donor due to the central cell corrections. The table (b) gives the valley splittings between the states* A_1, T_2 *and E for a P and a As donor.*

We can therefore list the advantages held by a dopant over quantum dots in silicon for quantum computation. First the donor lifts the valley degeneracy thanks to its deep confinement potential, whereas the degeneracy of the ground state of a two-dimensional quantum dot strongly depends on microscopic details and then are not easily reproducible. For a donor, the large valley splitting (above 10 meV, equivalent to 2.4 THz) allows for high frequency manipulations without any risk of populating excited states. Finally, although we have tried to avoid the random presence of nuclear spins in silicon because of their resulting fluctuating magnetic field, the control of single nuclear spins of P or As atoms through the hyperfine interaction is very attractive because of their usually long coherence times.

But this list has to be tempered. First the valley mixing physics, which remained strongly unexplored, can also be interesting thanks to new ways of manipulating quantum states with only electric fields [57]. Secondly, the major drawback of a strong confinement

is the difficulty to contact a donor. This was achieved these last few years in very short devices: thus one has to investigate the impact on the donor properties of the presence of local electrodes, oxides and electric field.

Influence of an interface

One can go one step further and try to investigate the effects of a nanostructure, with the proximity of different interfaces, on this spectrum. But this energy, as well as the whole spectrum of a dopant, is affected depending on its location in a nanostructure. To enlighten this point, Diarra *et al.*[21] considered an donor embedded in the center of a nanowire of radius R, surrounded by an other material with a dielectric permittivity ϵ_{out}. In a 3D bulk dielectric material, the positive charge is screened, leading for the donor to be considered as a charge $+e/\epsilon_{Si}$ and no more +e, the rest of the charge being repelled at infinity. But for finite structure a surface charge should exist, taking into account this rest of the screened donor and also should check the discontinuity relation for the normal component of the electric field due to the dielectric mismatch. This remaining positive charge, called the image charge, in the nanowire increases the attractive potential for the electron and therefore increases the ionization energy of the donor:

$$\Delta E_I \approx \frac{1}{4\pi\epsilon_0}\frac{2e^2}{\epsilon_{in}R}\frac{\epsilon_{in}-\epsilon_{out}}{\epsilon_{in}+\epsilon_{out}}F(\frac{\epsilon_{in}}{\epsilon_{out}}) \tag{1.13}$$

with F being a form factor. Taking $\epsilon_{in} = \epsilon_{Si} = 11.7$ and $\epsilon_{out} = \epsilon_{SiO2} = 3.9$, one obtains:

$$\Delta E_I \approx \frac{30.5(meV)}{R(nm)} \tag{1.14}$$

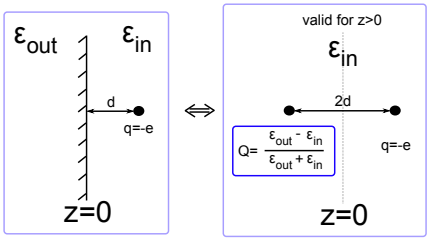

Figure 1.15 *Method of the image charge.*

This formula is valid for R higher than the Bohr radius of the donor, therefore neglecting any quantum confinement effect. Furthermore, Cobian *et al.* (unpublished) have performed simulations of the binding energy of a donor sandwiched in 20 nm-thick Si film as a function of the donor's position to the Si/SiO_2 interface (see Fig. 1.16). We observe that, in agreement with [21], the binding energy is above the bulk value when the donor is centered in the film. But when the distance to the interface is comparable to the Bohr radius, the binding energy drops to 25 meV. This is due to the symmetry breaking of the wave function around the donor's nucleus, which results for this wave function not to be centered anymore on the donor and to reduce the valley mixing of the ground state. It must be noted that a strong decrease of the binding energy also occurs due to the screening of the donor from the quasi-metallic SD (with $\epsilon_r \to +\infty$). Such effects have also been investigated in [38, 14] although assuming a one-dimensional system.

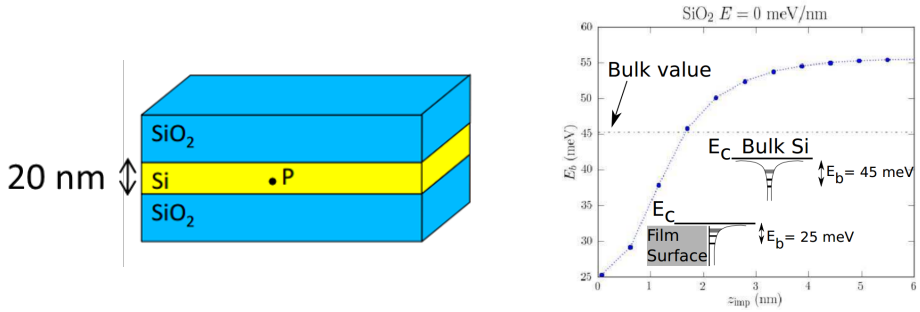

Figure 1.16 *Simulation of the binding energy of a phosphorous atom embedded in a 20 nm Si film. Adapted from Cobian et al., unpublished.*

As we described in this chapter, we are able to tune electric fields in our devices which affect the donor structure. A first striking feature related to the Stark shift is the displacement of the electron wave function from the donor to the interface wall. This is depicted in Fig. 1.17 , adapted from the work of Rahman *et al.* [87, 86]. At zero electric field, the wave function is centered on the donor nucleus and the spectrum in unchanged compared to the bulk. This the Coulomb-confined situation (C). Then at finite electric-field, a triangular potential well is formed at the interface and when the ground state of this well aligns with the ground state of the donor, we enter the hybridized regime (H) where the electron is delocalised between the donor and the interface. Finally if the electric field is strong enough, the electron is completely pulled towards the interface well because its levels are far below the donor ground state in energy: this is the interface bound state (I). It has to be noted that the electron still feel the attractive potential of the donor and therefore remains bound to it. A delocalised interface state, which would be the equivalent of a electron put in the silicon conduction band, is not created at this stage.

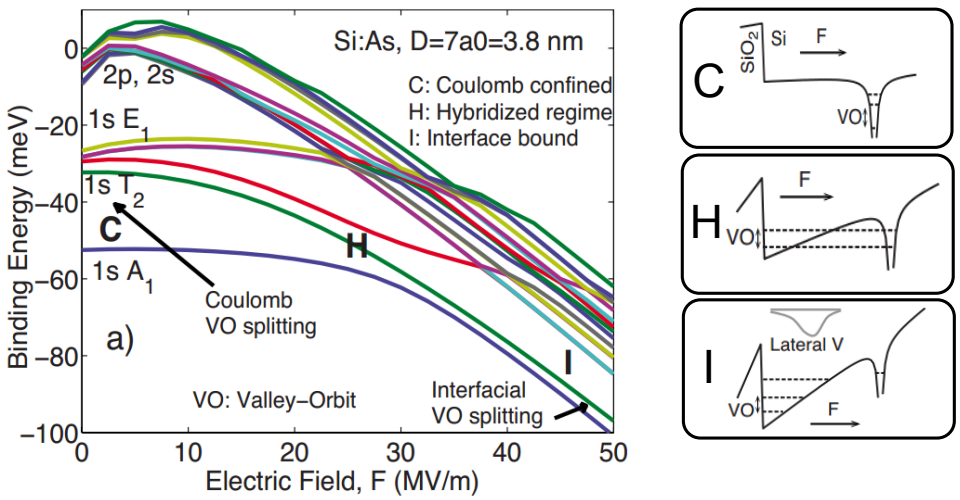

Figure 1.17 *Stark shift of an As donor close to an interface: from Coulomb confinement to the interfacial regime by increasing the electric field. Adapted from [87, 86].*

We can observe that the spectrum is strongly affected by the electric field, especially the valley splitting which is reduced from the bulk value to an interface value (discussed

in Chapter 4) when going from the Coulomb-confined to the interfacial regime. They also take into account the effect of the image charges with various interfaces (SiO_2, metal) to give a complete picture of the 1 dimensional problem.

We now review important experimental realizations concerning transport with dopants in silicon.

1.3.3 Transport with single dopant in silicon

Dopant assisted transport

The first signatures of individual impurity in MOSFETs were done measuring Random Telegraph Noise at low temperature [89]. The dopants, located at the Si/SiO_2 interface, were inducing a two-level signal of the channel resistance, according to the ionization state (D^+ or D^0) of the donor. Xiao *et al.*[120] succeeded in performing Electron Spin Resonance on such a trap. Other works have followed, we can cite those of Hofheinz *et al.* [42] and Golovach *et al.* [35] who focus on the dynamics of traps located in the barriers of the channel and on their impact on the conductance of single electron transitors. Morello *et al.* [65] deliberately implanted single donors close to SET which is then used as a detector of the donor spin state. Finally Khalafalla et al. were able to follow the influence of a donor on a SET thanks to a dual-gate device to get information about the donor location [49].

Direct resonant transport

As we have seen in this chapter, silicon MOSFET offers an excellent framework to study single donor. The size of nowadays transistors allow to have only a few donors in the channel, and these can be electrically connected between SD. Lansbergen *et al.* measured the excited states of donors in several FinFETs devices. Following the work of Rahman previously described [86], they deduce that these donors are in the interfacial regime [58]. An important step forward is the spin measurement of a couple of donors in such a device, performed by Sellier *et al.* [102]. In our group, Pierre *et al.* [80] linked the degraded room temperature Id-Vg characteristics of a short transistors to the presence of a single donor in the channel. This stochastic donor presence from sample to sample causes a large variability of the subthreshold characteristics.

The dopants addressed in those works concern random dopant which have diffused from SD to the channel. Therefore they rely on a stochastic process. Nevertheless we will take advantage of having a back-gate as a second parameter to further investigate those devices. Furthermore, we will see in Chapter 4 that we can modify the geometry of the device, with additional top gates to enhance the electrostatic control of the channel and play with the diffusion of the SD.

More reliable ways to control the position of donor have been developed in silicon nanostructures. This is done by Tan *et al.* [111] who measured resonant transport through single donors deliberately implanted in bulk silicon by a focused ion-beam. Finally, one can note the outstanding achievement realized by Fuechsle *et al.* who succeeded in realizing transport through a single donor [28], following their work on STM patterned devices presented in section 1.2.4.

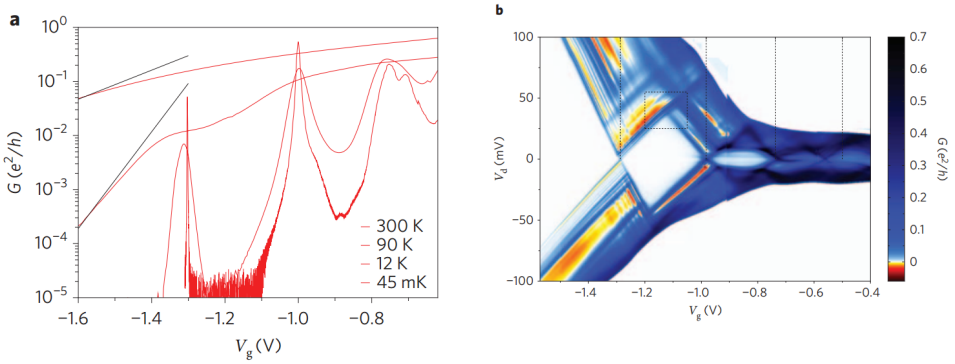

Figure 1.18 *(a) Transport through a single donor from room temperature to 40 mK. (b) Stability diagram (also called diamond in the manuscript) of the donor, allowing to extract the ratio of the capacitances. Adapted from [80].*

Double occupation

A last point to be developed in this section is the problem of the double occupied donor called D^-, *i.e.* the investigation of the analogous of the H^- problem [10]. This issue is very difficult to tackle theoretically as the electron-electron interactions have to be taken into account. A two-electron bound state on a single donor is interesting as it opens perspectives for spins and qubits manipulations.

In bulk silicon D^- systems have been found to be bound states, but with a very small binding energy of around 2.05 meV for As (1.07 meV for P) compared to the binding energy of the D^0 states (54 meV for As, 45 meV for P). Again, this binding energy is strongly affected by the presence of nearby interfaces. This has been studied by Hao *et al.* [39] and Calderõn *et al.* [14] within the effective mass approximation, including image terms and electron-electron interactions. We have adpated a figure of ref [39] in Fig. 1.19 showing the binding energy (normalised to the Rydberg energy) as a function of different interfaces and distances. The binding energy for the D^- state can be enhanced by a metallic interface, thanks to the screening of electron-electron interaction. However this statement falls if the donor is too close from the interface, because the second electron (called the outer electron), has a more extended wave-function that for the inner electron and becomes unbound. The case of an interface with a smaller dielectric constant decreases the binding energy of D^-.

The experimental results on the double occupied state of a single donor focus on the charging energy E_C, which is the energy required to add a second electron on a neutral donor. In bulk silicon, E_C equals 52 meV for a As donor and 43 meV for a P donor. Calderõn *et al.* estimated that this charging energy can be reduced by 25 % in presence of a quasi-metallic interface (Q=0.5). This is consistent with some experimental values found in literature, ranging from 26 to 36 meV [58, 101]. We will comment on these values in Chapter 3.

Finally, Rahman *et al.* investigated the influence of the electric field and of the hybridization of the donor with an interface state on the charging energy of a donor [85].

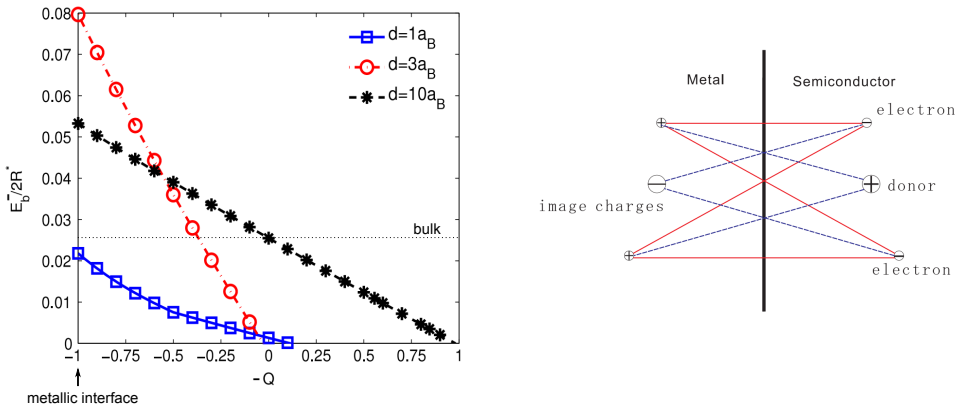

Figure 1.19 *Binding energies of the ouble occupied state as a function of the charge image Q, for different distance to the interface. Adapted from Hao et al. [39].*

They also find that the charging energy is reduced to 20-30 meV in presence of an electric field of about 30 MV/nm.

To conclude, we have seen the spectrum of a dopant is largely affected by the presence of interfaces, confinement and electric fields. The complexity arises from the fact that these different causes can induce competing effects on the donor. Therefore it is very difficult to extend these theoretical works to the experimental values, as the exact donor location in a transistor is usually unknown.

Chapter 2

First electrons regime in a silicon transistor

Contents

Introduction

We have seen the major developments of microelectronics, which nowadays has turned to become nanoelectronics with devices scaling down to the 10 nm range. The physics of diffusive Coulomb blockade in silicon MOSFET has been extensively discussed in previous works, but it was impossible to reach the so-called few electrons regime. In this regime the quantum nature of the dot blooms, with striking signatures such as the addition of the Zeeman energy to the classical charging energy.

We will see in this chapter that we are now able to reach this regime in these ultra-scaled transistors, thanks to the excellent electrostatic control of the channel and improved access resistances. In a first part we will perform a spectroscopy of the first four states in such a nanowire including a magnetic field dependence. Secondly we will investigate the impact of the leads on these first electrons thanks to two effects: the Kondo effect and the Fermi-edge singularity.

2.1 Corner states

2.1.1 Description of the samples

fabrication

In this section we focus on three different samples in which we obtained similar results. They were fabricated according to the exact same process and only differ by the channel length. The channel thickness is 11 nm and its width 40 nm. The channel is surrounded by a thermal SiO_2 and a HfSiON oxide layer with 0.8 and 1.9 nm respective thickness, resulting an equivalent SiO_2 oxide layer of 1.5 nm. Furthermore a 5 nm-thick TiN layer was deposited with 50 nm-thick n^{++}-poly Si on top to form the front gate. A TEM picture of such a sample is presented on Fig 2.1. The gate can be connected through both sides of the nanowire, which allows to flow a current through the gate. Here both ends of the gate will always be biased with the same gate voltage. The SD doping was performed as described in section 1.1.3.

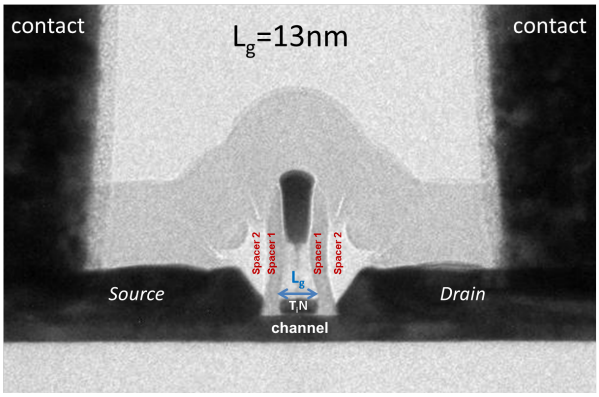

Figure 2.1 *TEM picture of sample with* $L_g = 13\,nm$*, showing the TiN gate, the channel the SD and the vias which make the contacts*

Room Temperature characteristics
We present on Fig 2.2 the room temperature conductance as a function of gate voltage for the three samples measured at lower temperature. From the thermally activated regime we extract as in section 1.1.4 the alpha parameter which characterizes the gate level of control on the channel. We can observe that the α parameters are higher than for the sample presented on section 1.1.4. This illustrates the improved control of the channel thanks to the thinner oxide layer. We can also observe that α decreases from sample #1 to #3 , *i.e.* when the channel length increases from 44 to 74 nm. This is just related to a random choice of these samples among the thousands available. Semi-automatic room temperature measurements performed on a whole wafer show a very low variability of the process (see Appendix A).

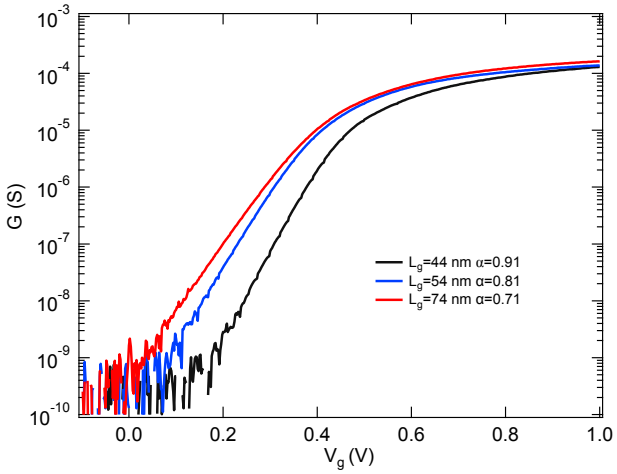

Figure 2.2 *Room temperature characteristics for the 3 samples measured at low temperature. The α factors are closer to 1 compared to the sample of Fig 1.7, illustrating the improved control of the gate on the channel for these devices.*

2.1.2 Two dots in the two top corners

We present the low temperature measurements for sample #2. On Fig 2.3 is plotted the differential conductance measured at 300 K, 4 K and 100 mK as a function of V_g. From 300 K to 4 K we observe that the current in the thermally activated regime has disappeared as expected (a). Above the threshold voltage (expected here at $V_g = 0.5\,V$ due to the work functions of the metallic gate, see section 3.2.2) we observe several conductance peaks, labelled A_1, B_1, B_2 and A_2 on Fig 2.3 (b). Although the conductance has dropped between 300 K and 4 K, one can on the contrary observe an increase between 4 K and 100 mK for these peaks. This is a first signature that we have reached the single level regime. Finally we see that for $V_g \gtrsim 0.65\,V$ corresponding to high density of electrons in the channel, the conductance at 4 K is even higher than at 300 K, illustrating the metallic behaviour of the SD and that the channel mobility at 300 K is limited by phonons and not by the static disorder.

We now focus on these first four peaks. First it has to be noted that they are located above the conduction band threshold voltage of the transistor. Furthermore no

doping was pre-implanted in the channel and the gate length is long enough to prevent any dopant which would have diffused towards the channel to be electrically connected to SD, as opposed to the samples in ref [63] and to the work presented in Chapter 3. Hence we attribute these resonances to the first electrons in the silicon conduction band.

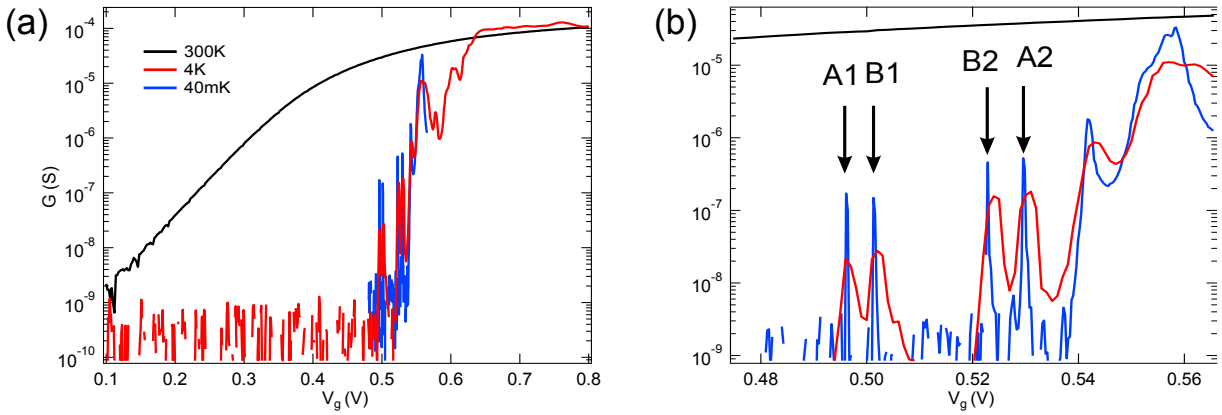

Figure 2.3 *Evolution of the conductance for different temperatures. (a) G vs. Vg at 300K, 4K and 100mK. Below 4K, the thermal actiavted regime has vanished and only current above the threshold voltage is detected. (b) Zoom of (a) showing the increase of the conductance peaks maxima from 4K to 100mK, signature of the single level regime.*

It is striking to observe that they form two pairs (A_1,B_1) and (B_2,A_2). As a first hypothesis, it would be tempting to attribute this modulation to the effect of a single dot spin-filling, as we have previously described in Chapter 1: the two first electrons are added on the same orbital (or valley) and therefore no extra energy (no Zeeman energy as no magnetic field is applied) has to be paid apart from the classical charging energy. But to add the third electron, one needs to populate a new orbital (or valley) which implies an additional orbital-spacing contribution to the addition energy. Again, the fourth electron can fill the same orbital with an opposite spin. In our device, this simple scheme can be easily ruled out thanks to a measurement of these peaks as a function of the two gates V_g and V_b. We plot on Fig 2.4 a 2D-map of the device conductance according to the two gate voltages. We recover at $V_b = 0\,V$ the four peaks labelled A_1, B_1, A_2 and B_2. Moving to negative back-gate, we can observe that the lines A_1 and A_2 run parallel to each other and the same occurs for the lines B_1 and B_2, which exhibit a clearly different slope. To quantify this point, we plot in the inset the gate shift ΔV_g of each resonance with respect to its position at $V_g = 0\,V$ as a function of V_b. According to the model described in Chapter 1 and equation 1.6, this ΔV_g shift that one has to apply to counterbalance a change in V_b for a level to stay on resonance (*i.e.* keeping a constant electrochemical potential on the dot) equals:

$$\Delta V_g = \frac{C_b}{C_g} \Delta V_b \tag{2.1}$$

We can clearly observe that A_1 and A_2 have the same coupling ratio: we find $\frac{C_b^A}{C_g^A} \approx 4.5 \times 10^{-3}$. A similar behaviour is observed for B_1 and B_2 but with a different ratio: $\frac{C_b^B}{C_g^B} \approx 3.6 \times 10^{-3}$.

Such a difference can't be explained with only one dot in the channel. Instead it suggests that the observed Coulomb peaks correspond to two dots in parallel.

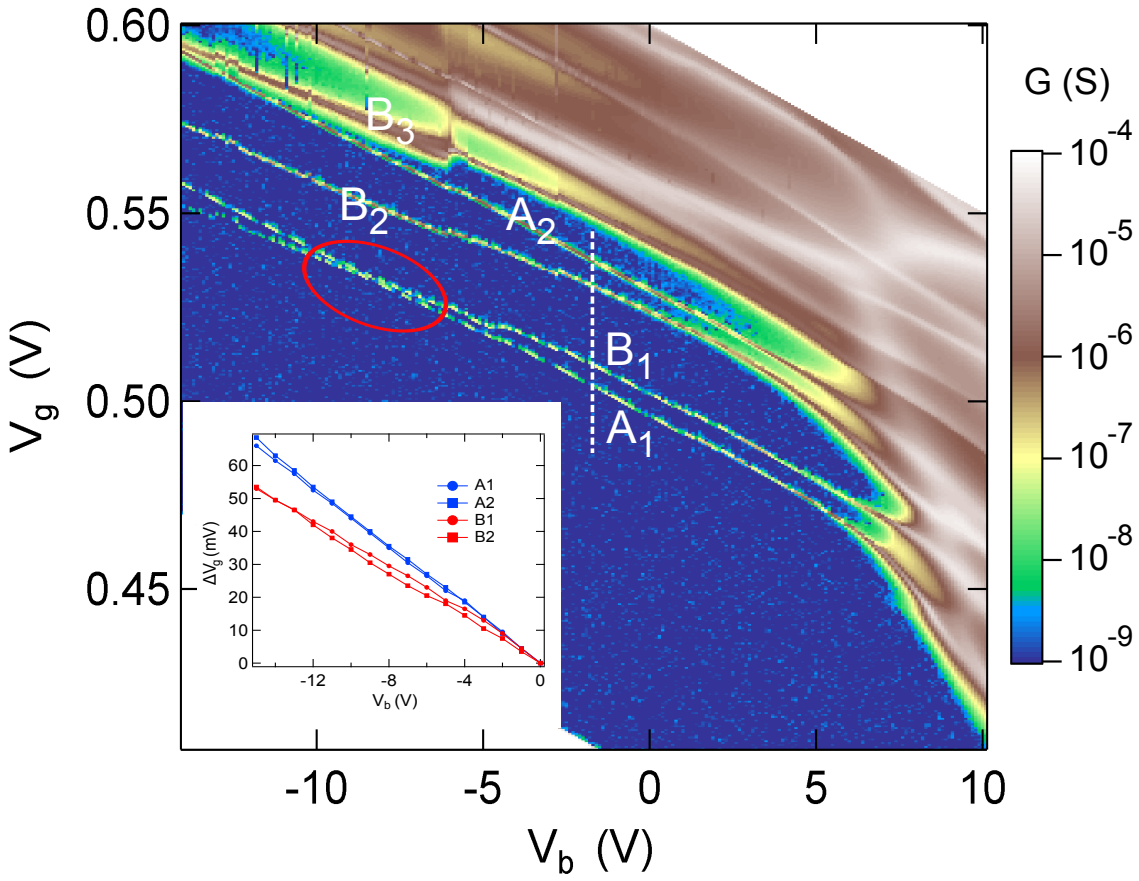

Figure 2.4 *Differential conductance measured at T=100 mK with* $V_{ac} = 30\mu V$ *as a function* V_b *and* V_g*. for negative* V_b*, one can observe two series of lines A and B which run in parallel. They are attributed to the corner states of the nanowire. Inset: position of each line relatively to their position at* $V_b = 0V$*.*

At first it is not obvious to imagine that two quantum dots can co-exist in parallel in such a small nanowire. We believe this is due to its particular geometry, which is, taking a cut along SD in the middle of the channel as in Fig. 1.4, a rectangle with relatively sharp corners. These corners induce a point effect resulting in a stronger electric field as compared to the body and the flat edges of the channel. Hence these parts can pin the wave functions of the first electrons and create a double dot device.

This is confirmed by simulations of the real device done by Yann-Michel Niquet and Viet N'Guyen in INAC/SP2M in Grenoble. They use a 3D-Poisson solver combined to a Debye-Hückel model to calculate the electric potential and the electron density distribution inside the channel, as a function of the different gate voltages. The Fig 2.5 shows a preliminary result of such a simulation done at 77 K, with $V_b = -7\,V$ and V_g such that the total concentration in the channel corresponds to one electron. In (a) we plot the carrier concentration on a 2D cut along SD, at a height close to the top of the nanowire,

given by the grey dotted line of (b). (b) shows the same data represented on a transverse cut of SD. We can observe a higher carrier concentration in the corners of the nanowire. The confinement along SD is absent and hence the electron density (or wave function) spreads all along SD. We can see on Fig. 2.5 (c) and (d) that confinement arises when we add a surface disorder, with a typical amplitude of 2-3 nanometers, extracted from current mobility at room temperature. The gate dielectric disorder is usually larger for HfSiON than for the spacers. Then electrons can then be stochastically confined in the corners of the nanowire, below the gate (and not below the spacers).

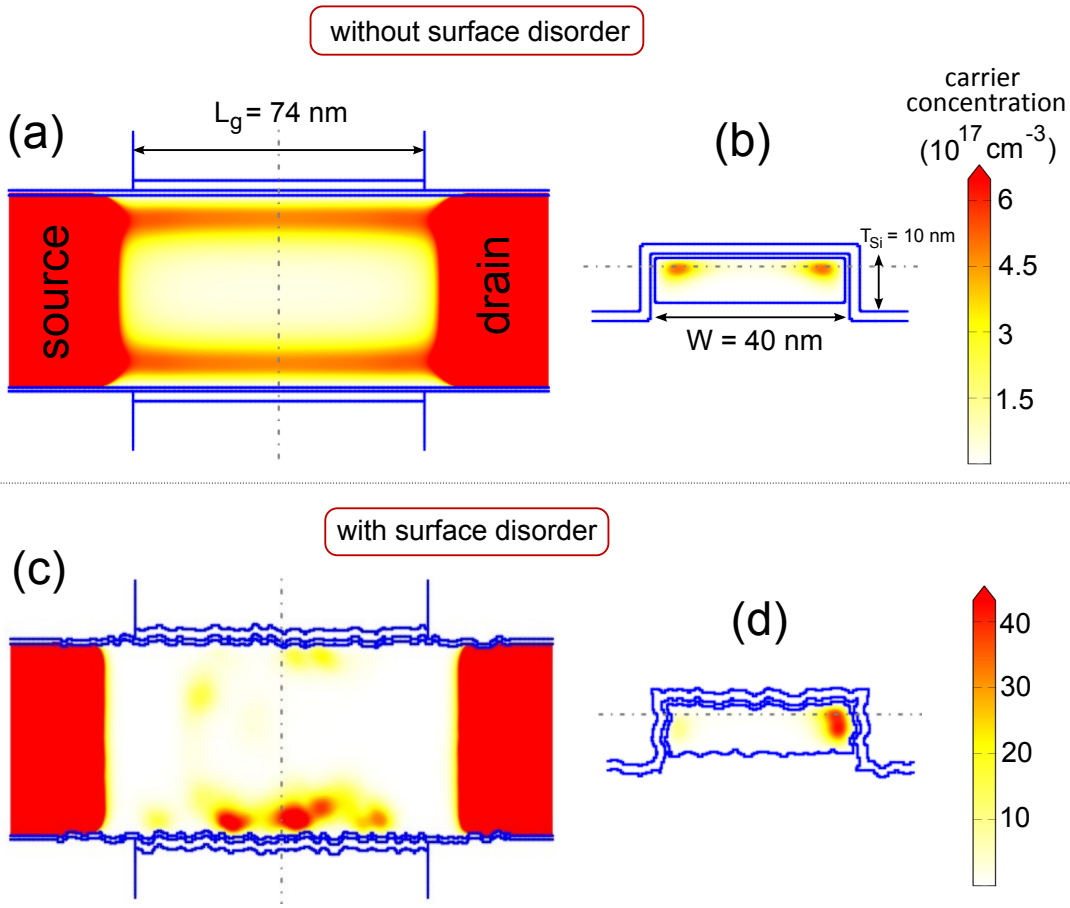

Figure 2.5 *Simulations of the electron density at 77K (with* $V_b = -7V$ *and a* V_g *corresponding to one electron) in the nanowire. (a) cut along SD, at a height given by the broken line of (b). (b) Transverse cut of SD in the middle of the channel (along broken line of (a). One can clearly evidence a higher carrier concentration in the top corners of the nanowire. (c) and (d) Effect of realistic and calibrated surface disorder, which stochastically confines electrons in the corners. From Niquet et al., private communications.*

We can investigate the different coupling capacitances of these two dots with the environment. We plot on Fig 2.6 the stability diagram at $V_b = -2V$, i.e. the conductance as a function of V_g and V_d. We find the usual Coulomb diamonds and extract thanks to the slope of their edges (black dotted lines) the different capacitances of the two dots: one can note the large gate capacitance compared to the SD capacitances. This leads to high α parameters (> 0.8), very close to 1, illustrating the excellent gate control of the device even at low temperature. We can also observe a substantial difference between the

two charging energies, with $E_C^A \sim 1.5\, E_C^B$, with E_C^A deduced from the extrapolated crossing between the edges of its diamonds. Thus dot A must a have a smaller extension than dot B.

dot	C_g (aF)	C_d (aF)	C_s (aF)	α	E_C (meV)
A_1	2.54	0.30	0.21	0.83	26.3 ± 1
B_1	3.90	0.30	0.46	0.84	17.2 ± 1

Table 2.1 *capacitances and α parameters for A_1 and B_1*

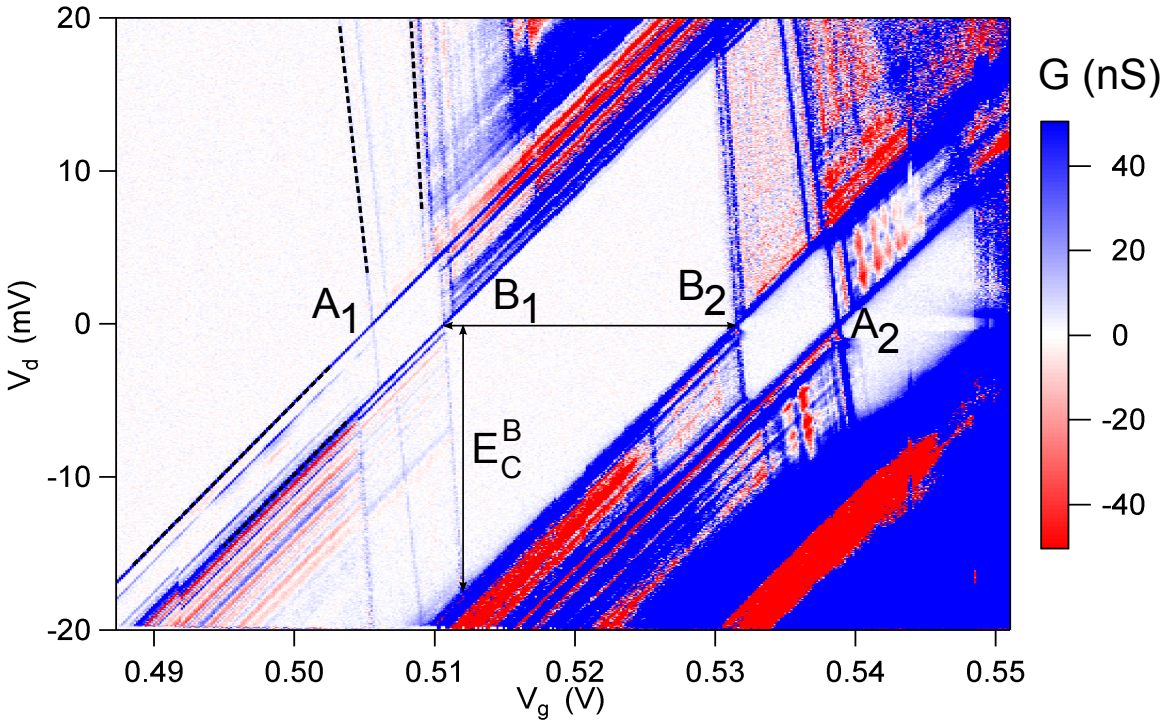

Figure 2.6 *Stability diagram (differential conductance) performed at $V_b = -2\,V$ (T=100 mK, $V_{ac} = 20\mu\,V$). One can deduce the charging energies of the two dots A and B as well as their capacitances.*

Figure 2.7 shows a zoom of the Fig 2.6 focusing on the first two electrons. On the top of the Coulomb blockade region, when the edge of diamond B_1 marked by the lower white dotted line crosses the edge of the diamond A_1 (positive slope), one can observe a shift of the white line towards lower energy. This is due to the electrostatic repulsion between the two dots as explained here. In the region labelled (1), A_1 is blocked and occupied with an electron: in order to add an electron on B_1, one has to pay the charging energy of this dot but also add the Coulomb repulsion with the electron lying on A_1. This is no more the case in the region (2), when the two levels are in the bias window: here there is no necessarily an electron on A_1 and thus the mutual charging energy disappears for B_1 (until an electron fills A_1 again): its edge shifts towards lower energy. This phenomena occurs

for all the lines attributed to the diamond B_1. This allows to extract the mutual charging energy [115]. We find here $E_C^m = 0.95 \pm 0.2\,meV$. Taking the bare Coulomb interaction in silicon and a distance corresponding to the device width W=40 nm, one should find as a rough estimate:

$$E_C^m = \frac{e^2}{4\pi\epsilon_0\epsilon_{Si}W} = 3.1\,meV \tag{2.2}$$

The reduction by a factor of 3 compared to this expectation. This illustrates the screening role of the top gate and especially its metallic part made of TiN, as mentioned in chapter 1.

For the diamond A, one can also clearly observe lines inside the diamond which run parallel to its edges, denoted by the upper black dotted line. Such lines could correspond to excited state of the dot [24] as they point towards higher energies. Up to now, in our system, such lines were rather attributed to the local density of states of the reservoirs [79, 53, 68, 27], due to disordered metallic SD. We will see in the next sections that here, this line can undoubtedly be attributed to an excited state and we will discuss its nature. A similar line, also attributed to an excited state can be isolated for the dot B, marked by the white dotted line.

Previous works already pointed out the existence of these corner states in trigate MOSFET at low temperature [102, 43] but not in the few electrons regime as we discussed here.

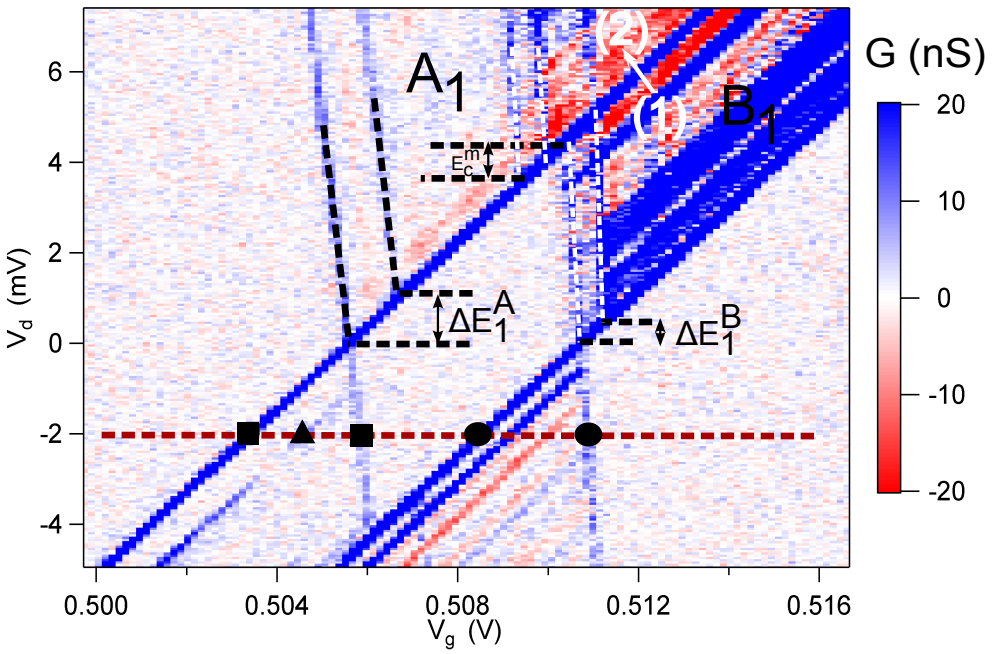

Figure 2.7 *Zoom of Fig. 2.6 on the first electrons* A_1 *and* B_1. *Parallel lines to the edges of the diamonds are observed, attributed to excited state of the dots with energies* ΔE_1^A *and* ΔE_1^B. *We also deduce the mutual energy between the two dots* E_C^m.

2.1.3 Spin-filling of the first electrons

We perform a magnetic field dependence of the first two electrons of each dot. This was done again at $V_b = -2\,V$ along the white dotted line of Fig 2.4. We apply a SD bias $V_d = -2\,mV$ and measure the conductance as a function of V_g (hence measuring a cut in the diamonds along the brown broken line of Fig 2.7), varying the magnetic field from 0 to 5.5 T.

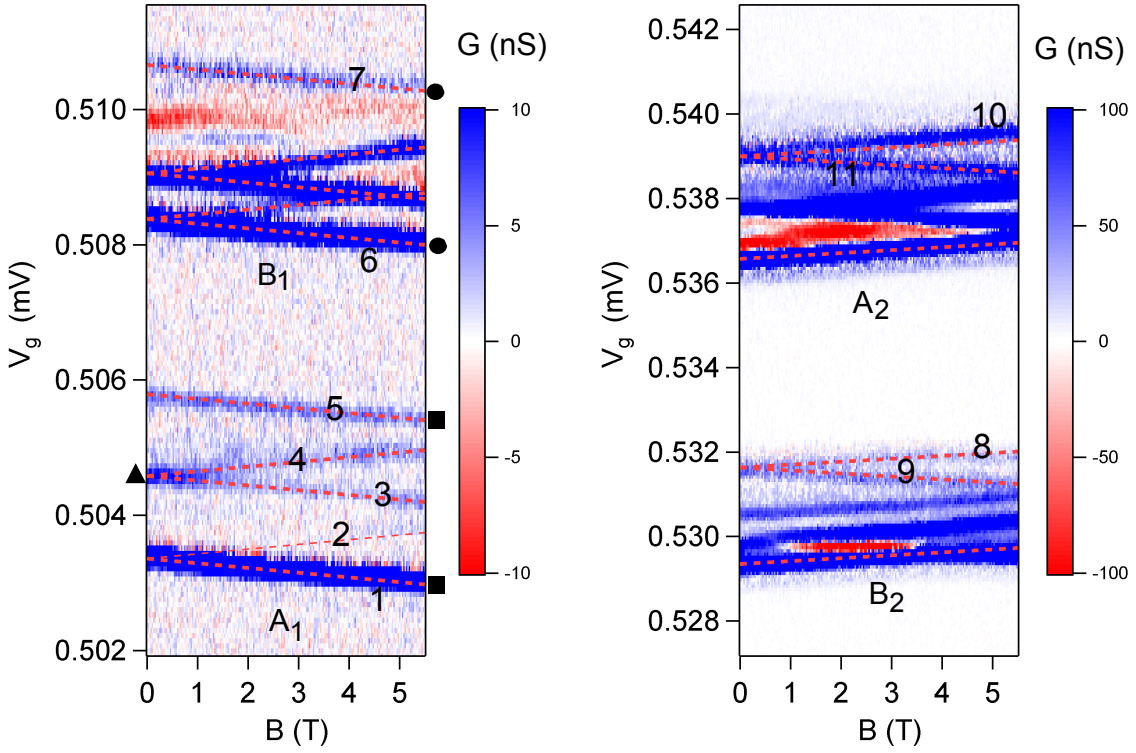

Figure 2.8 *Magnetic field dependence of the first two electrons on dot A and B. We plot the differential conductance as a function of the field B and of* V_g *with a finite bias* $V_d = -2\,mV$*, which corresponds to a cut along the red dotted line of Fig. 2.7. We evidence a spin 1/2 dependence (left) for the first electron on each dot and a singlet for the two-electron ground state (right).*

electrons A_1 and B_1

The results are plotted on Fig. 2.8. On the left we follow the evolution of the diamonds cuts for electrons A_1 and B_1. As guides, the black squares (resp. black spheres) represent the edges of the diamond A_1 (resp. B_1), also represented on Fig. 2.7. We start by discussing the diamond A_1. We observe that the position of its edges linearly decrease with the magnetic field. The slope is in total agreement with the expected slope for a spin -1/2 (by convention we take the -s (+s) as the Zeeman ground (excited) state, with s being the spin), given by the red dotted lines 1 and 5 for A_1, simply converted from an energy scale to a gate voltage scale with α:

$$\Delta V_g = \frac{\Delta E_Z}{\alpha} = \frac{57.8^* B}{0.83} \sim 69.6\,\mu eV/T \tag{2.3}$$

Throughout the manuscript, we take the convention to call "spin down" the spin ground state and "spin up" the spin excited state.

Current rectification in A_1

One should observe this spin excitation as a line inside the diamond whose position linearly increases with B: line 2. We barely can identify this line in Fig 2.8. To understand this point, we plot on Fig 2.9 (a) the d.c. current in the diamond A_1 for a magnetic field of 5.5 T. For a positive bias ($V_d > 0$) we can clearly identify the lines parallel to the edge of diamond attributed to the spin up of the ground level (called A_1^0) as well as the spins down and up of the first excited state (called A_1^*). Measuring the current for a finite bias (2.3 mV) along as a function of V_g results in four current steps which can be identified on Fig 2.9 with the red arrows. For the same bias voltage at zero field (Fig 2.7), only two steps are measured due the spin degeneracy which is recovered. The situation is different for negative bias ($V_d = -2.3\,mV$) with a constant current measured, independently of the field. We can also note that this current corresponds to the level of current measured at $V_d > 0$ when only one level is involved in the transport (about 12 pA). This means that for negative bias, although two levels are within the bias window, the current did not increase but remained constant.

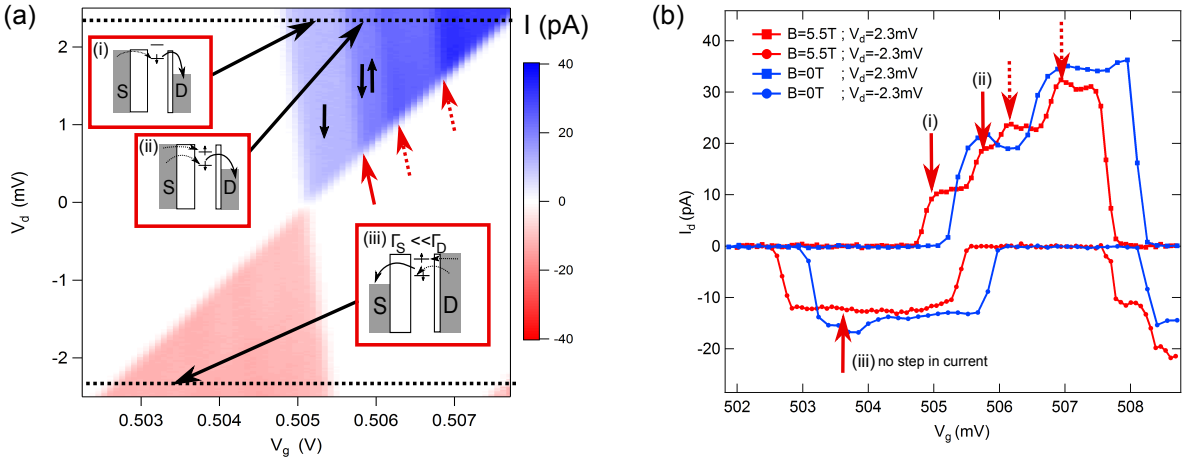

Figure 2.9 *Current rectification in the diamond A_1. (left) Diamond (plotted in current) of A_1 done at 5.5 T. (right) current at $V_d = -2.3\,mV$ (spheres) and $+2.3mV$ (squares) for B=0 T (blue) and 5.5 T (red). For positive bias, one observe a step in the current with the spin up enter the window (red arrow), which is absent for negative bias. The same phenomenon occurs for the excited state (dotted red arrows).*

This can be understood introducing an asymmetry between the source and drain tunnel rates [11, 122]: we assume that $\Gamma_S \ll \Gamma_D$ and that two non-degenerate levels (two spin states of the same level under a magnetic field) can be in the bias window. The current flowing through the device is given by the master equation for sequential tunneling 2.4, where Γ_{in} is the tunnel rate for an electron to enter the dot and Γ_{out} to leave it: if $V_d > 0$, $\Gamma_{in} = \Gamma_S$ and $\Gamma_{out} = \Gamma_D$ and inversely if $V_d < 0$[1]. For simplicity we will consider

[1]Note that if the quantum level is degenerate (for instance spin), one should take it into account by introducing a factor 2 between the *in* and *out* tunnel rates, due to the increased number of possibilities for an electron to tunnel from the reservoir to the level: $\Gamma_{in} = 2\Gamma_{out}$.

that all the levels have the same tunnel rates to the leads, which is non-trivial.

$$I = |e|\frac{(\Sigma\Gamma^i_{in})\Gamma_{out}}{\Sigma\Gamma^i_{in} + \Gamma_{out}} \tag{2.4}$$

From here we follow the sketches presented on Fig 2.9(a), which shows the SD current for the diamond A1 for a magnetic field of 5.5 T. First on situation (i), only the spin down of A_1^0 is in the bias window. Hence $\Sigma\Gamma^i_{in} = \Gamma_S$ and $\Gamma_{out} = \Gamma_D$.

$$I_{(i)} = |e|\frac{\Gamma_S\Gamma_D}{\Gamma_S + \Gamma_D} \rightarrow |e|\Gamma_S \, since \, \Gamma_S \ll \Gamma_D. \tag{2.5}$$

Note that the same current is obtained for negative bias, which is indeed observed. Now we move to the situations (ii) and (iii) where the two spin levels are involved: $\Sigma\Gamma^i_{in} = 2\Gamma_S$ for (ii) and $\Sigma\Gamma^i_{in} = 2\Gamma_S$. Therefore:

$$I_{(ii)} = \frac{2\Gamma_S\Gamma_D}{2\Gamma_S + \Gamma_D} \rightarrow 2|e|\Gamma_S = 2I_{(i)} \qquad I_{(iii)} = \frac{2\Gamma_D\Gamma_S}{\Gamma_S + 2\Gamma_D} \rightarrow |e|\Gamma_S = I_{(i)} \tag{2.6}$$

The current doubles for positive bias but remains constant for negative bias, which corresponds to the experimental observation. We see here the important role played by the tunnel rates. These can't be easily controlled in our devices and are especially very sensitive, as well as the local density of states which blurs the spectroscopy, to the back gate voltage. These asymmetries usually evolve in a non monotonic way, reflecting the remaining disorder still present at the edges of the SD and makes it difficult to follow such excited states with the back gate.

A key point concerns the line attributed to an excited state (marked by a triangle, also on Fig 2.7): we can indeed observe that it is also Zeeman splitted with a 1/2 spin (lines 3 and 4). They also lead to two steps in the current for positive bias in Fig 2.9 (b), when these states enter the bias window and contribute to current (third and fourth steps). This would not occur if this line was due to a fluctuation in the reservoir density of states, but it would just follow the Zeeman spin down state [68] and give a peak (or a dip) in the current. Therefore we unambiguously conclude that it is a dot's excited state. The same behaviour is observed for the diamond B_1 (top-left lines of Fig 2.8) with the edges corresponding to a 1/2 spin down. There is also an excited state, at lower energy than the one for B_1, and which also splits with the magnetic field with a 1/2 spin.

electrons A_2 and B_2

We now focus on the right plot of Fig 2.8, showing the magnetic field evolution of the second electrons of the dots A and B and follow the same procedure. We can observe an opposite behaviour for both electrons as compared to the first electrons: here we see that the edges of the diamonds point towards higher energies, matching with a +1/2 spin state marked again by the red dotted lines (lines labelled 8 and 10). We can also observe two lines (9 and 11) which point towards lower energies, linearly separated from the +1/2 state at the second edge of these diamonds. They correspond to an excitation where an electron down left the dot from the singlet state, leaving it in the one-electron excited

state (spin up). We conclude that for both dots and for magnetic fields below 5.5T, the two-electron ground state is a singlet.

electron B_3

We tried to perform the same spectroscopy on the resonance corresponding to the third electron on the dot B, *i.e.* B_3 (see Fig. 2.4). To do so we have to work at a very negative back-gate voltage ($V_b = -30V$) in order to reduce its tunnel couplings (see Fig 2.10 (a)) and being able to detect the expected lines corresponding to a Zeeman splitting. Unfortunately, for such a V_b range, the device presents an enhanced charge noise which prevents from doing a conclusive spectroscopy, as shown on Fig 2.10 with a diamond performed at 4 T. We can note on (a) that we are able to detect the higher electron occupation numbers B_4, B_5 and A_3. We can also note crossings between different electrons in the two conductance plots vs. (V_b, V_g), as the one circled in red in Fig 2.4 but were not investigated during this work, as the two dots are almost independent for this width. A decrease of the device width would probably enhance the tunnel coupling between the two dots and could lead to an interesting regime for spin and charge manipulations[2].

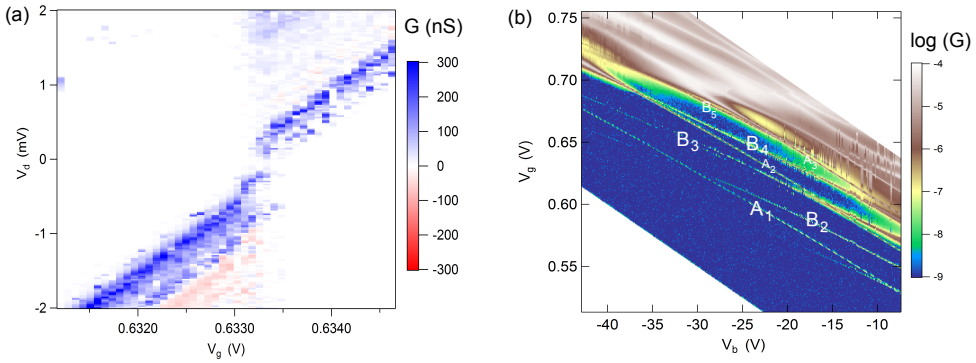

Figure 2.10 *(left) diamond (differential conductance) for the resonance B_3 taken at 4 T. Because of the noise, no statement can be done on its spin state. (right) same than Fig 2.4, for lower values of V_b. One can identify higher dots occupation numbers, up to five electrons for dot B.*

We now discuss the nature of this excited state and the spin-filling that we observe.

2.1.4 Nature and evolution of the first excited state

The spin magnetospectroscopy we have performed in our silicon transistor not only gives information about the spin states of the dots but also allows to directly have access to their energy spectrum. Identifying an excited state by classical spectroscopy (*i.e.* lines parallel to the edge of a diamond) doesn't give information about the degeneracy of the ground level of the dot or about nearby excited states to the ground state which wouldn't be electrically detectable, because of the thermal or intrinsic broadening of the resonances. Nevertheless the magnetospectroscopy will be sensitive to these excited states because it will affect the spin filling of the dot according to the scheme presented on Fig 2.11. We

[2]However a decrease of the width can also induce a loss of back-gate sensitivity due to the screening of the surrounding top-gate.

take the two first levels of the dot (in blue and red) and supposed that they are separated by an energy Δ_1 (which can be null for a degenerate ground state). At zero magnetic field, the spins are degenerate resulting in a triplet state if $\Delta_1 = 0$ and a singlet state if $\Delta_1 > 0$ (we assume no exchange). Then we switch on the magnetic field. It is clear that if a degeneracy still remains (if $\Delta_1 = 0$), the triplet state will be conserved and the resonance due to the addition of the second electron will also shift towards lower energy (negative V_g as for the first electron. However a different result is obtained for $\Delta_1 > 0$: for low field ($B < B_c$) on (b), the two spin states of A^0 are still lower in energy than A^* and therefore we obtain a singlet state. The second resonance will be shifted to higher energies, due to the addition of $g\mu_B B(s_{triplet} - s_{down}) = +1/2 g\mu_B B$ to the charging energy. Increasing the magnetic field will induce a crossing between $A^*_\downarrow$ and $A^0_\uparrow$, resulting in the two-electron ground state to become a triplet, as shown on (b). The critical field B_c at which the transition is observed directly gives the energy of the first excited state.

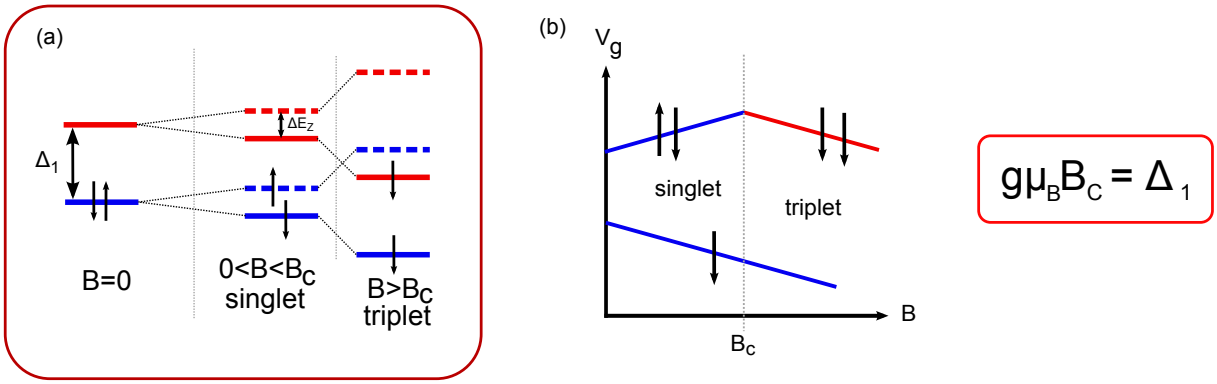

Figure 2.11 *Scheme of singlet-triplet transition. A non-degenerate state (except spin) (blue) is located below the first exited state (red) with an energy difference Δ_1. Increasing the magnetic field will lead for the two-electron ground state to change from a singlet to a triplet when the Zeeman energy equals Δ_1.*

Such a procedure was used by Lim *et al.* [60] who found a critical field of 0.86 T, attributed to a valley-orbit splitting of 0.10 meV. Hu *et al.* [45] also identified singlet state and a large valley splitting of 1.6 meV, although they were not able to probe the singlet-triplet transition, occurring at a too high magnetic field. On the contrary, Xiao *et al.* [119] measured a parallel spin filling independently on the field. Although unclear, they attribute this result to a higher spin exchange coupling. Finally, Takashina *et al.* measured a giant valley splitting of 23 meV [110], which isn't fully theoretically understood. In our case, the potential singlet/triplet transition couldn't be reached either because of a limited field of 5.5 T in this experiment, compared to the first observed excited state for A_1 ($\Delta E_1^A = 0.95 \pm 0.10$ meV) and B_1 ($\Delta E_1^B = 0.55 \pm 0.10$ meV).

We move to an other sample (sample #3) on which a V_b dependence of this valley splitting has been performed. We first show on Fig. 2.12 (a) a diamond recorded at $V_b = -10$ V corresponding to the first electron in the channel: we even measured for this configuration the first excited state at 2.20 ± 0.1 meV. We check that this lines splits with magnetic field as previously, by measuring the conductance at $V_g = 0.589$ V as a

function of V_d and B (b). This energy is even higher than the ones measured for sample #2. Then we followed the excited state energy Δ_1 as a function of V_b.

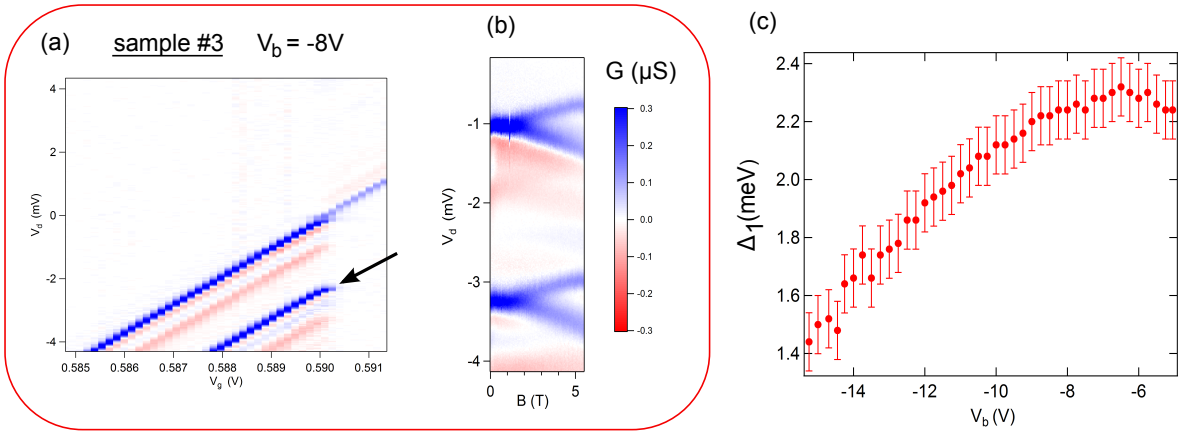

Figure 2.12 *Dependence of the first excited state measured for sample #3 as a function of the back gate. The left panel shows a diamond (a) of the first electron at $V_b = -8\,V$ and a magnetic field dependence vs.* V_d *done at* $V_g = 589\,mV$ *(b). (c) shows the energy of the excited state depicted by an arrow vs.* V_b*. We observe a decrease of* Δ_1 *when the back-gate is decreased, not compatible with an increase of the electric field.*

We can observe a decrease of this energy from about 2.2 meV for $V_b = -5V$ to 1.4 meV at $V_b = -15V$. A simple picture would be to consider that we increase the electric field in the nanowire when we decrease V_b, because at the same time one needs to increase V_g for the quantum level to stay in the bias window (see equation 1.6). Therefore a stronger electric field should enhance the potential confinement of the dot and results in larger excitations energies. Here this is inconsistent with our observations. To be more quantitative, a simulation of the electric field and of the wave functions extensions in the channel as a function of the gate voltages would be very helpful.

Nevertheless we have demonstrated that we have fully lifted the bulk valley degeneracy thanks to a strong electron confinement in the nanowire corners, in order to obtain a singlet for the two-electron ground state. It is established that the silicon six-fold degeneracy is lifted to a four-fold set of Δ-valleys and a two-fold set of Γ-valleys when electrons are confined to a Si/SiO_2 interface [4] (see chapter 1), which can be enhanced thanks to strain as in SiGe heterostructures. Many efforts have been devoted to the study of the lifting of these remaining Γ-valleys. First, the sharpness of the interface induces a potential deep which can lift this degeneracy. This is difficult to account on a theoretical point of view as it strongly depends on the details of the interfaces: a rough interface tends to suppress the splitting [26] but on the contrary, the presence of interface states and their mixing with the conduction band states can enhance it [98]. Furthermore this splitting can be enhanced thanks to an external electric field, inducing a stronger electron confinement at the interface [98, 97, 86]. All these theoretical works, based on Tight-Binding simulations and effective mass approach, result in a valley splitting in the order of 1 meV for strong electric fields (>1 V/nm), which is close to the oxide breakdown values. This complex interplay between interface disorder and electric field is a probable first lead to explain our experimental observation about the evolution of Δ_1 with V_b. We can also note that

all the theoretical frameworks we have mentioned, apart from the simulations presented in the previous section, have so far concerned SiO_2 oxide layers, whereas in our sample the oxide is mainly composed of HfSiON.

An other type of dot excitations are obviously the orbital levels. Usually in Si/SiO_2 inversion layers, one considers a 2D well potential. Here, due to the strong confinement in the corners of the nanowire, even at 77 K as illustrated by the simulation presented on Fig 2.5, we rather consider a 1D density of states. The level spacing between the two first orbitals is thus given by the formula (with N=1 and L=74 nm, the length of the front gate):

$$\Delta E_{orb} = \frac{N^2\hbar^2\pi^2}{2m^*L^2} \approx 210\,\mu eV \tag{2.7}$$

This value is far below the energy of the measured excited state. This may be due to the transverse confinement which may occur on a length L_{eff} lower than the actual gate length, for example due to the surface disorder as presented in Fig. 2.5 (c) and (d). In order to recover $\Delta E_{orb} \sim 1\,meV$, one should take $L_{eff} \sim 34\,nm$. Nevertheless we see here that the orbital and the valley splitting are of the same order of magnitude in our device. This could result in a mixing between orbitals and valleys which should be taken into account for a further quantitative analysis of the corner state spectrum.

To conclude on this section, we have measured large valley-orbit splittings in these device from 0.55 to 2.2 meV, which represent large values as compared with the existing theories. These latter also predict an increase of this splitting with electric field, which doesn't correspond to our observations.

2.2 Interactions with the reservoirs

2.2.1 Valley cotunneling and Kondo effect

On the first section of this chapter, we have focused on negative back-gate voltages, where the electrons are pulled towards the top corners of the nanowire. We now move to another regime at $V_b > 0$ where the electrons are on the contrary attracted towards the body of the channel. This can be seen on Fig. 2.4 for $V_b > 5\,V$ where we can observe two features: first a strong increase of the conductance and secondly a cusp in the onset of the conduction band which becomes more sensitive to the back-gate (with a steeper slope in the (V_b, V_g) plan). These observations point towards a higher coupling with the leads and with an electron gas which has been pushed towards the body of the channel or even on the back interface. We plot in Fig. 2.13 (a) a diamond in differential conductance for the first electrons in the channel at $V_b = 9\,V$. We focus on the first blockade region: we can observe conductance resonances. We further plot on (b) the SD conductance as a function of V_d, for $V_g = 477\,mV$. We observe three peaks: the central one is attributed to a spin Kondo resonance, discussed further. The two satellite peaks, also presenting a Kondo behaviour are attributed to Γ-valleys Kondo as described below.

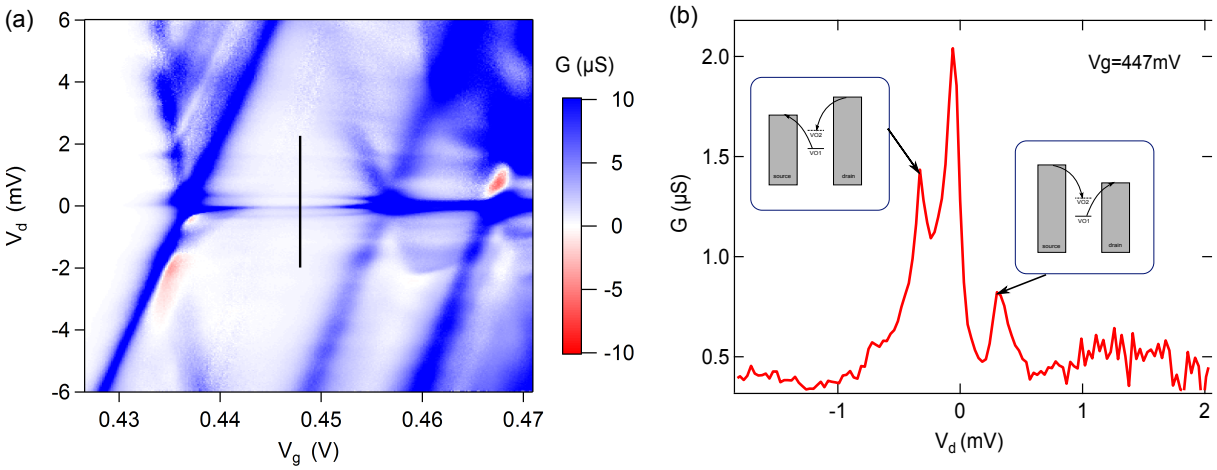

Figure 2.13 *(a) diamond (differential conductance) recorded at* $V_b = 9\,V$ *with no magnetic field. (b) Cut along the black line of (a) showing the Kondo ridge and the satellite peaks attributed to inelastic valley cotunneling.*

Now we focus on the central peak at $V_d = 0$, attributed to a Kondo resonance. The Kondo effect is a well-known many-body problem in condensed matter physics. It was initially observed in the 30's by an anomalous logarithmic increase of metal resistance at low temperature in presence of magnetic impurities. But it took about thirty years and strong debates before a satisfactory explanation of this phenomena could be given. Using a perturbative approach, Jun Kondo explained the effect as the result of an effective exchange interaction between the localized spin of a magnetic impurity and the delocalized electrons spins of the metal [52]. In 1988, Ng and Lee [70] and Glazman and Raikh [32] suggested that the Kondo effect could manifest also in a single-electron transistor confining a spin-1/2 state [32]. In this case, the coherent exchange interaction between the localised spin state and the delocalized reservoirs effectively increases the tunnel rates and hence the conductance. The first experimental signature of the Kondo effect in a quantum dot were reported by Goldhaber-Gordon *et al.* [34], followed by the achievement of the Kondo unitary limit (a dot conductance of $2e^2/h$) by Van der Wiel *et al.* [116].

Importantly, the spin can actually be replaced by any other degree of freedom as for instance orbital or valley degeneracy. This can give rise to exotic Kondo effects, with a higher Kondo ground state symmetry, *e.g.* from SU(2) symmetry if only spin is involved to SU(4) symmetry if both spin and two degenerate orbitals are involved. Such a Kondo effect was measured in carbon nanotubes by Jarillo-Herrero *et al.* [46], inducing transitions between pure orbital and pure spin Kondo resonances thanks to the magnetic field. The case is silicon is thus also very attractive thanks to the valley degree of freedom [104]. But yet only few realizations have been performed in silicon devices [94, 107]. This is due to the difficulty to have a sufficient coupling between the first electrons of the dot and the reservoirs. Only recently, some possible experimental evidence of such SU(2) orbital Kondo resonance was claimed to be observed for an As donor embedded in a FinFET [59, 113].

In this manuscript, we will mostly focus on the spin Kondo resonance. We turn to the

sample #1. The corresponding Coulomb diamond (in differential conductance) is plotted in Fig. 2.14(a). This sample showed similar features than sample #2 but with higher tunnel rates, allowing to observe Kondo ridges at $V_b = -5V$, where this measurements were performed. The SD conductance is shown in Fig. 2.14(b) as a function of the bias voltage at $V_g = 560\,mV$ (along the black dotted line of (a)), for several temperatures from 900 to 40 mK. We can indeed observe an increase of the SD conductance at low temperature. To confirm that this peak is related to Kondo physics, we have plotted in Fig. (c) the maximum conductance (extracted from a Lorentzian fit of the peak) as a function of the temperature. We have fitted this behaviour with the empirical law given by [33]:

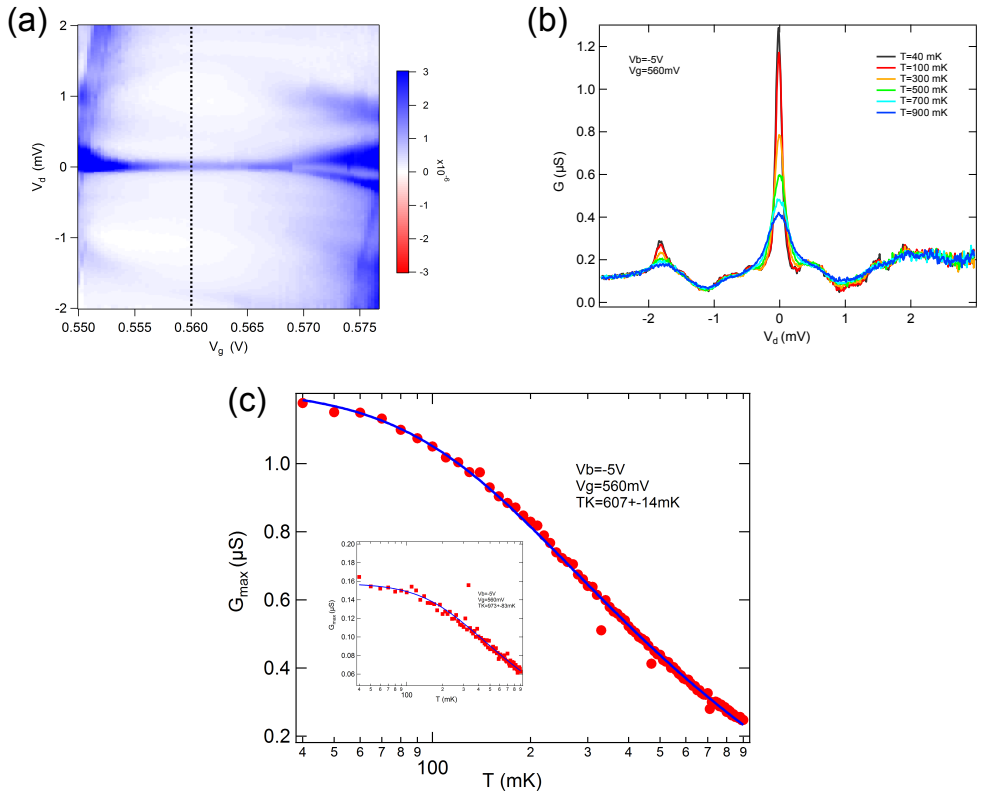

Figure 2.14 *Temperature evolution of a Kondo ridge. Sample #1. (a) diamond recorded at* $V_b = -5\,V$. *(b) cut along the black dotted line of (a) at several temperatures. We can identify the spin Kondo resonance at* $V_d = 0\,mV$ *and one faint valley Kondo at* $V_d = -1.8\,mV$, *both increasing when the temperature is lowered. (c) Temperature fit of the maximal conductance of the spin Kondo resonance. Inset: similar fit for the valley Kondo peak at* $V_d = -1.8\,mV$.

$$G_{max}(T) = g_0 + G_{max}\left(\frac{T_K'^2}{T^2 + T_K'^2}\right)^s \tag{2.8}$$

with $T_K' = T_K/\sqrt{2^{1/s} - 1}$, T_K the Kondo temperature and s a constant equal to 0.22. The very good agreement between this law and our experimental results confirms the Kondo nature of this resonance at zero bias. We have found a Kondo temperature $T_K = 607 \pm 14\,mK$. This Kondo temperature can be related to the tunnel rate $\Gamma = \gamma_S + \gamma_D$,

the charging energy E_C and the detuning ϵ_0 of the level with respect to the Fermi level thanks to the Haldane relation:

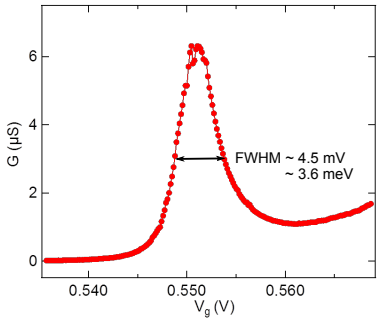

Figure 2.15 *Estimation of* Γ*, taking the FWHM of the first electron resonance.*

$$T_K = \frac{\sqrt{\Gamma E_C}}{2} exp\left(-\pi \frac{\epsilon_0(\epsilon_0 + E_C)}{2\Gamma}\right) \tag{2.9}$$

We can give an order of magnitude of these parameters. For this back-gate, the charging energy was estimated to be around 10 meV. Furthermore we can estimate Γ from the Full Width at Half Maximum (FWHM) of the first electron resonance from its conductance at zero bias, we found $\Gamma \approx 3.5\, meV$. Finally, we performed the temperature dependence approximately in the middle of the Coulomb blockade region, meaning $\epsilon_0 = -E_C/2$. Finally equation 2.9 yields an effective Kondo temperature of $T_K \approx 3.6\,K$, which is 5 times more than the experimental one. We can note that this relation is very sensitive to Γ, $\Gamma = 2\,meV$ gives $T_K \approx 500\,mK$. Nevertheless the fact that we can reach the Kondo regime in such small systems illustrates the very low access resistances of the devices, which allow to obtain such high tunnel couplings.

We can also identify in the inset of Fig 2.14(c) a tiny increase of the conductance of the resonance attributed to the valley Kondo peaks. We obtained with the similar fit procedure $T_K^{valley} \approx 973 \pm 83\,mK$, of the same order than for the spin Kondo resonance.

We performed on sample #2 a magnetic field dependence on such spin Kondo resonance. The Zeeman energy lifts the spin degeneracy and hence destroys the spin Kondo coherent state. As a result the Kondo resonance is expected to vanish with the magnetic field.

We plot in Fig. 2.16 the results of such a measurement. In (a) is plotted a diamond performed at $V_b = 7\,V$ on sample #2. One can identify the three peaks corresponding to the spin Kondo resonance and the satellites peaks attributed to the valley Kondo resonance. In (c) we present the SD differential conductance as a function of the magnetic field B and the bias V_d. As expected the central peak vanishes for a small magnetic field (less than 0.5 T). However for a finite magnetic field we clearly identify inelastic cotunneling steps [18] in the differential conductance (see also the diamond on (b) at B=2.8 T), as marked by the white dotted lines and labelled from 1 to 3. These steps are also visible in (d) where the SD conductance is plotted vs. V_d for 0 and 2.8 T, denoted by the black arrows. We explain these steps thanks to the schemes of Fig. 2.17. We represent the two valley orbitals (VO1 and VO2, respectively in blue and red), assuming a Zeeman splitting larger than the valley splitting. The down spins are represented by solid lines and up spins by dotted lines. It is important to notice that all these states are in parallel, as they belong to the same dot, we have only set an horizontal shift between VO1 and VO2 for clarity.

We start with the line labelled 1. We see that its position in V_d is independent of the

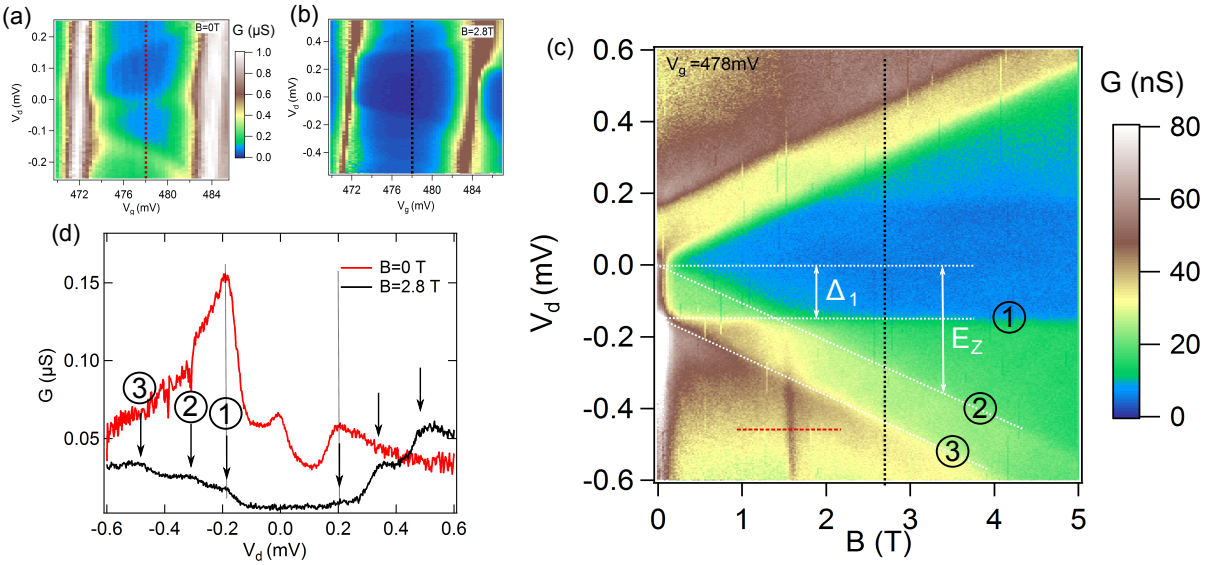

Figure 2.16 *Magnetic field dependence of the Kondo and valley resonances. Sample #2. (a),(b) Diamonds at B=0 and 2.8 T. (c) Differential conductance vs. B and* V_d*. The spin Kondo vanishes with the magnetic field, but lines of different slopes appear, attributed to inelastic cotunneling process as explained in Fig 2.17. (d) SD conductance vs.* V_d *for B=0 and 2.8 T. At 2.8 T we observe the steps (labeled from 1 to 3) due to the inelastic cotunneling.*

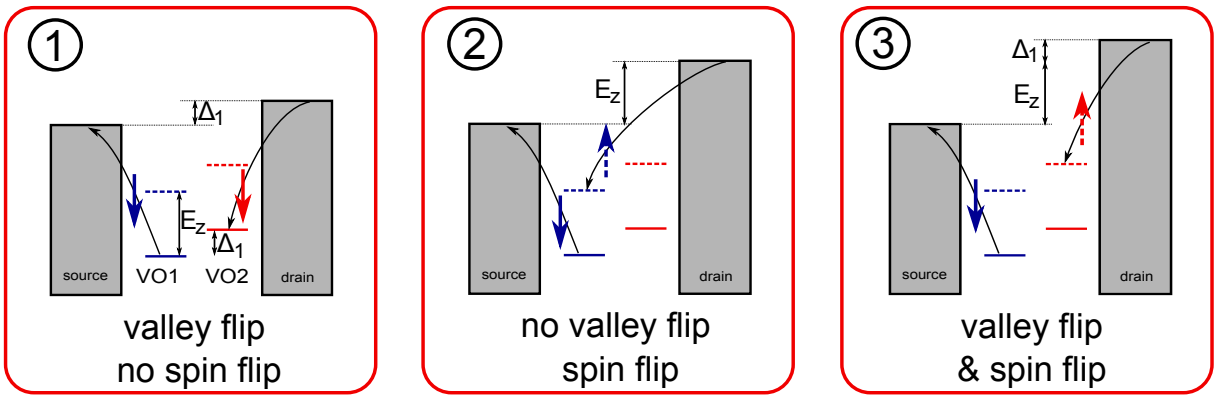

Figure 2.17 *Schemes illustrating the process involved for each inelastic cotunneling step 1 to 3 of Fig. 2.16, assuming* $E_Z > \Delta_1$*. To our knowledge, we identify in this experiment the first signature of an inelastic cotunneling process involving both a valley and a spin flip (3).*

magnetic field. This line corresponds to the onset of inelastic cotunneling processes involving a flip in the valley but not in the spin. Therefore its bias-voltage position provides a measure of the valley-orbital splitting, which is independent of B. On the contrary the line 2 evolves with the magnetic field and its energy corresponds to the Zeeman energy. We then attribute this line to a cotunneling process involving a spin flip within the same valley. Finally, the line 3 runs parallel to line 2: it also has a contribution from the Zeeman energy but it is shifted towards higher energies (in absolute value) by the amount of the valley splitting. We conclude that line 3 represents a cotunneling process involving both a spin and a valley flip. To our knowledge, such a process has not been reported in the literature. All these lines can be identified at both bias polarities, with some small

asymmetries arising from possible asymmetries in the tunnel rates.

2.2.2 Fermi-edge singularity

In this part we present an other type of interactions between a localized state and the reservoirs. We start from an experimental observation: we plot in Fig. 2.18 (a) a diamond for sample #3 at $V_b = -15\,V$. It is very important to notice that we have plotted the SD current and not the differential conductance.

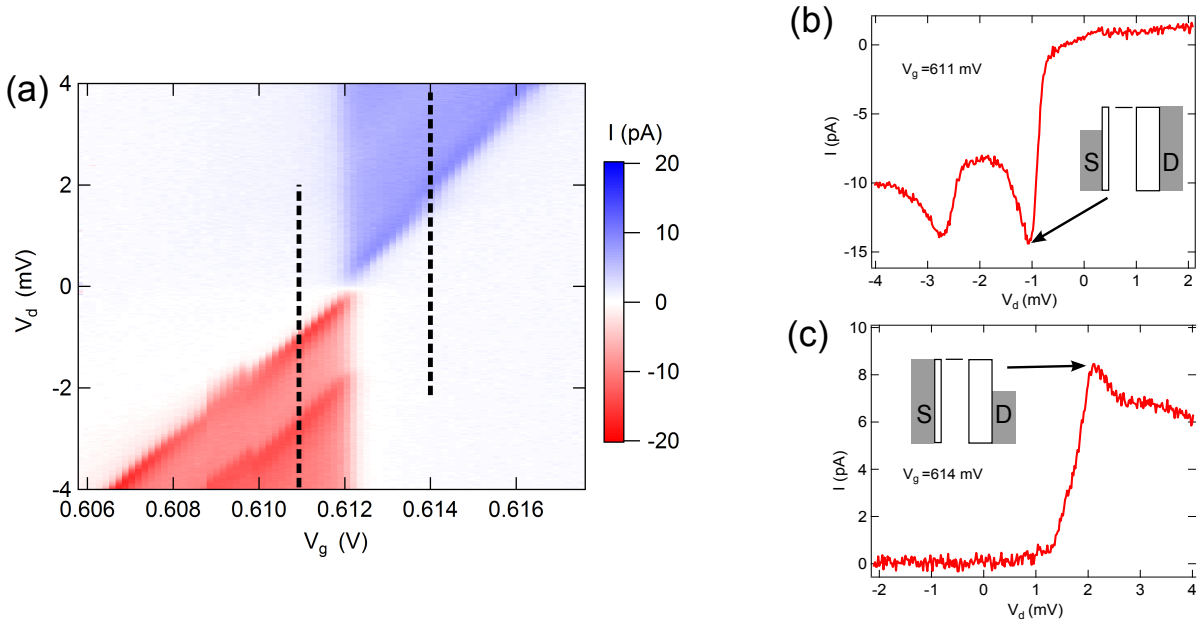

Figure 2.18 *Sample #3. (a) diamond (d.c. current) at* $Vb = -15V$. *(b) (resp. (c)) d.c. current at* $V_g = 611\,mV$ *(resp.* $V_g = 614\,mV$. *One observes a strong increase of the current when the level is aligned with the Fermi level of a reservoir.*

First we note that we observe an excited state, with an energy of about 2 meV, only for the negative polarity. This suggests that for this configuration $\Gamma_S > \Gamma_D$. Secondly we extract a cut of the current for $V_g = 611mV$ in Fig.(b): we can observe a strong increase of the current when the level is aligned with the Fermi level of the drain: the current reaches 14.3 pA at the Fermi level and drops to 8.5 pA inside the diamond. Such a peak can also be observed with the excited state on the same polarity. The same phenomena occurs for the positive polarity although the peak is much less pronounced.

A classical master equation as developed in section 2.1.3 can only result in current steps when several levels enter the bias window. The effect of a Local Density Of States (LDOS) can also be ruled out: this LDOS results in modulation of the current not only at the Fermi level of the reservoirs but on the whole bias window. Moreover the amplitude of the observed modulation (50% of current increase) does not correspond to the modulations arising from LDOS. Secondly we believe that this resonance at the Fermi energy cannot correspond to Van Hove singularities, which also lead to a divergence of the density of states at the Fermi energy in one dimensional systems, because our reservoirs are

fully three-dimensional.

Here we describe an other type of mechanism to explain this phenomena. Matveev and Larkin investigated the effect of the Coulomb interaction between the localized state and the electrons in a reservoir [64]. When an electron tunnels from the localized state to a reservoir, it leaves a hole which creates a scatterer for the conduction electrons of the reservoir as depicted in Fig. 2.19.

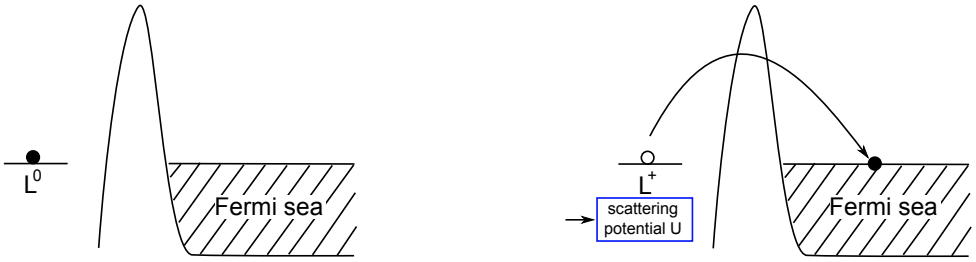

Figure 2.19 *Schemes to explain the core-hole potential. When an electron tunnels from the localized to the reservoir, it leaves a hole which affects the wave function of the conduction electrons of the reservoir. This potential leads to a modification of the tunnel rate.*

They consider a first order theory to calculate the tunnel rate, taking into account this scattering potential for the electron and find a power-law dependence of the tunnel current:

$$I(V_d) \propto \Theta(E_F - E_L)(E_F - E_L)^{-\gamma} \tag{2.10}$$

This exponent α can further be expressed as function of the phase shifts δ_{ij}, i for the momentum and j for the spin, of the conduction electrons scattered on the core-hole potential:

$$\gamma = \frac{2\delta_{01}}{\pi} - \sum_{(ms)\neq(01)} \left(\frac{\delta_{ms}}{\pi}\right)^2 \tag{2.11}$$

Here, two competing effects appear: The first term in γ describes the increase of the tunneling rate due to the hole potential. The second term is always negative and hence contribute to decrease the tunneling rate. It is related to the abrupt change of the reservoir many-particle wave function when the hole potential is created. This effect is know as the Anderson orthogonality catastrophe.

In this theory, Matveev et al. assumed a perturbative limit to a perfect diffusive Fermi sea and obtained in the case of a 3D confined reservoir that the γ exponent can be expressed as a function of the Fermi momentum k_F in the reservoir and of the distance d between the localized state and the reservoir: $\gamma \propto (k_F d)^{-2}$. In the limit of a perfect Fermi sea, this yields $\gamma \ll 1$, and then a very weak effect on the tunnel current.

On the experimental side tunneling FES has so far been reported in resonant tunneling vertical devices in III-V or II-VI heterostructures without control gate [31, 25, 95]. An exception is the FES between a defect state in the SiO_2 gate oxide and a bound state in

the accumulation channel of a MOSFET studied using random telegraph noise[17]. In all these vertical devices $(E_F - E_L)$ is only varied by changing the drain voltage and there is no gate to control it. The state L is either a nanometric quantum dot in barrier [25] or a localized state at the bottom of the potential well in a resonant tunneling diode [31]. All these works report for higher γ exponent (as instance 0.22 for [31] and 0.54 in [95]) than expected from the perturbative theory.

Because there is no control gate when $(E_F - E_L) \simeq 0$ (E_F either in the source or drain) E_L is far above (or below) the Fermi energy in the other electrode. Therefore the FES anomaly observation can be affected by the non-linearities of the tunnel rates and the LDOS effects in the other electrode. Moreover the strong electric field can induce a space charge region or a potential well in the electrode [25]. Because doping is necessary either to adjust the resonant level or to provide good contacts in these vertical structures, under strong electric field donors in the electrode are ionized randomly with the bias voltage [30]. Therefore observing the FES in a lateral structure with a control gate to shift E_L on demand is very recommended. Unfortunately up to now the FES has not been observed in these structures, probably because the metallic gate used to control the tunnel rates reduces strongly U by screening and also induces a larger distance d between the localized state and the Fermi seas.

Here we believe than our devices could represent a very interesting alternative to these geometries. Indeed we are in presence of a localized state which is well controlled by a surrounding gate. Moreover the hole potential the screening of the hole potential on the conduction electrons should be reduced thanks to the very proximity of the SD. We present preliminary results on these γ exponents extracted from our experimental data presented in Fig. 2.18. In order to fit the SD current, we have used the same function derived in [64] and used in [31], assuming that $\gamma_S \gg \gamma_D$ from the asymmetry in the current between the two polarities:

$$I(V_d) = \left(\frac{D}{\sqrt{e^2(V_d - V_{d0})^2 + \Gamma_S^2}} \right)^{\gamma} \left(\frac{\pi}{2} + arctan(\frac{e(V_d - V_{d0})}{\Gamma_S}) \right) \tag{2.12}$$

V_{d0} is the onset of the current and depends on the gate voltage. D and Γ_S are related to the bandwidth of the system. We plot on Fig. 2.20 the result of such fits for the negative polarity. On (a) is the same cut than for Fig. 2.18 at $V_g = 611mV$ and obtained $\gamma = 0.55$. On (b) we plot the dependence of this exponent as a function of the gate voltage. On the diamond of Fig. 2.18 we can identify a shift around $V_g = 609mV$ (reproducible over different sweeps), attributed to an offset charge in the SD. We see that γ is affected by this charge and decreases to ≈ 0.2 at this point. This illustrates how a gate could be used to modify the electrostatic environment of the device and then tune the γ exponent. For the tunnel rate, we estimate $\Gamma_S \approx 30\,GHz$ from those fits and $\Gamma_D \approx 30\,MHz$ which represents a giant asymmetry. Again a major issue arises from the LDOS which stochastically appears in the current and has prevented up to now from performing further investigation of this exponent, as a function of the back-gate for instance.

Nevertheless we also find large γ-exponents, compatible with the other experimental

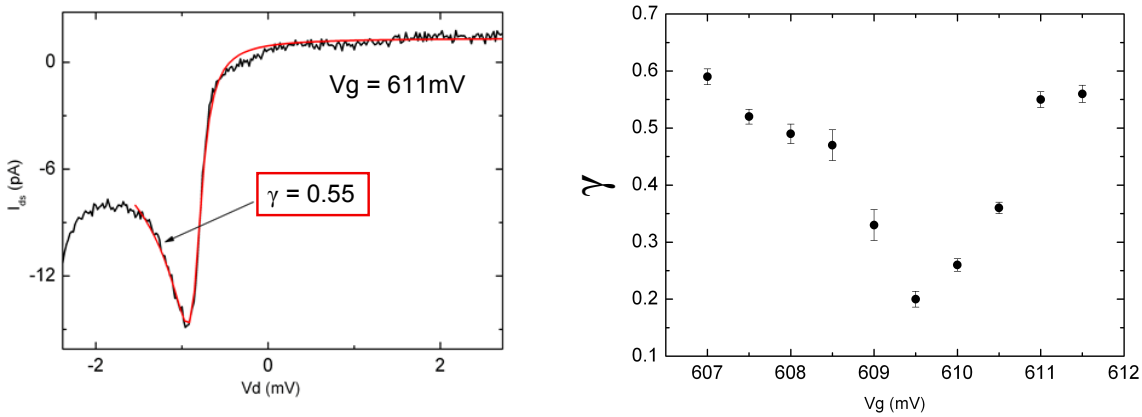

Figure 2.20 *(a) Fit of the tunnel current at* $V_g = 611\,mV$*. We obtain* γ*=0.55. (b) Dependence of* γ *with* V_g*. We observe a decrease of the exponent to 0.22 at* $V_g = 609\,mV$ *when the electrostatics is modified by a time-fluctuating charge (see Fig. 2.18 (a)). This reveals the sensitivity of the Fermi-edge singularity to the microscopic details of the reservoirs.*

realizations described above. Many investigations have been carried out in order to improve the theoretical model and explain these large exponents. Some works point their attention on the effect of a strong backscattering in the reservoirs [41, 1]. In this situation γ exponents could increase up to 1. This point could be relevant in our system as our reservoirs are heavily doped silicon and then subject to disorder. As a consequence, the exponents are really sensitive to the microscopic details of the reservoirs, as our experiment seems to reveal.

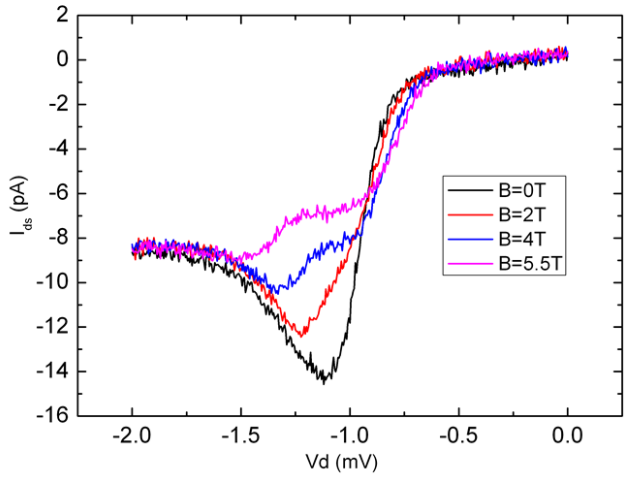

Figure 2.21 *Magnetic field dependence of the current at* $V_g = 611\,mV$*. The current peak at the Fermi level vanishes, and we recover the usual Zeeman splitting of the current.*

Finally, we show in Fig. 2.21 current traces as a function of V_d, taken at $V_g = 611mV$ for several magnetic fields. We clearly observe the Zeeman splitting of the current, with the presence of two steps at 5.5 T. Interestingly, the peaks in the current vanishes when one increases the magnetic field. This is rather unexpected as the Fermi-edge exponents should change only if the orbital of the many-body wave function of the conduction electrons is affected [25]. This should occur at higher magnetic field (above 10 T) when high Landau levels are pinned.

Conclusion

The corner states from a new kind of quantum dots in silicon. We were able to reach the few electrons regime and perform a careful addition and excitation spectroscopy. We evidenced large valley splittings up to 2 meV, although such large values as well as their dependence with the back-gate remain unclear. These quantum dots also allow to investigate the physics of electronic correlations with the Kondo effect in an original valley-orbit regime and the Fermi-edge singularity.

Chapter 3

Dopant ionization in short trigate MOSFETs

Contents

Introduction

We have seen in Chapter 1 that we are now able to perform resonant tunneling through individual donors. The presence of different interfaces and electric field also affect their properties, as their ionization and the stability of the double occupied state D^-. We will extend this work in this Chapter, being able to vary this electric field on a same donor, thanks to variations in the front and in the back gates. This work, supported by numerical simulations of the actual device geometry, will reveal the complex interplay between the donor position in the nanowire, the large transverse electric field and the impact of the different interfaces, insisting on the screening role played by the metallic SD.

3.1 Description of the samples

3.1.1 Fabrication specificities

The samples we are going to present in this chapter slightly differ from the fabrication process we have described in Chapter 1. Indeed, as we aim to study dopants and their interactions with the nanostructure, we need a device with a few donors in the channel. This goes somehow to the opposite direction compared to the current microelectronics objectives presented in Chapter 1, aiming at avoiding any dopant in the channel, which is a cause of variability.

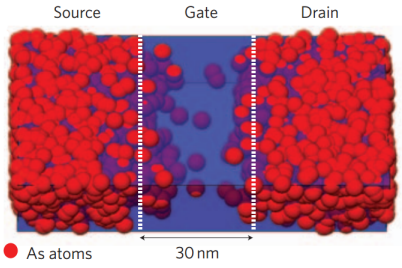

Figure 3.1 *Simulation of a boron doped sample including the whole fabrication process. The red spheres represent the As atoms which diffused from SD to the middle of the channel during the annealing step. From [63].*

However we fabricated such devices in the past few years [63]. They consist in FD SOI MOSFETs ($L_{ch} \times T_{Si} \times W = 30 \times 17 \times 50\,nm^3$), with a surrounding gate covering 3 faces of the nanowire trigate. The channel is isolated from the gate thanks to a 4 nm-thick SiO_2 layer and from the substrate, thanks to a 400 nm-thick BOX. Then, for those samples, no spacers were grown. This has a dramatic influence on the doping profile of the samples: instead of diffusing during the activation annealing step from the leads to under the spacers, keeping the channel under the gate practically undoped, they will diffuse from the leads towards under the gate: we obtain a channel which stochastically contains a few dopants. A pre-implanted channel doping is also performed, either with Bore or Arsenic. We finally obtain an effective channel length (∼10-20 nm) much smaller than the nominal one (30 nm). This short channel allows any dopant in the channel to have sufficient tunnel couplings to SD and thus to be detected by resonant tunneling. The Figure 4.2 presents a simulation of the geometry for a Boron doped device taking into account all the fabrication steps. These simulations will be developed in chapter 4, the point here is to illustrate the diffusion of the As donors (red spheres) to the middle of the channel.

3.1.2 Room temperature variability

We have fabricated around 100 identical devices with the same gate lengths and channel thickness but various widths. Semi-automatic current measurements performed at 300 K give us the yield of working devices and also enable us to draw their $I_d - V_g$ characteristics. This is done on Fig. 3.2, with panel (a) presenting boron doped and (b) Arsenic doped samples. Two points should be emphasized here. First, a change in the width of the device should only cause an increase of the ON-current (more current with a larger width as the resistance of the channel decrease) but shouldn't affect much the threshold voltage or the sub-threshold slope. Here we can observe a huge variability in the characteristics of those devices in both panels, some of them presenting a slope close to the maximum slope expected at room temperature ($k_B T \ln(10) \simeq 60\,\mathrm{mV/decade}$ at 300 K, represented by the black dotted line on these panels) but other presenting a clearly degraded slope, which can't be correlated with a change in width.

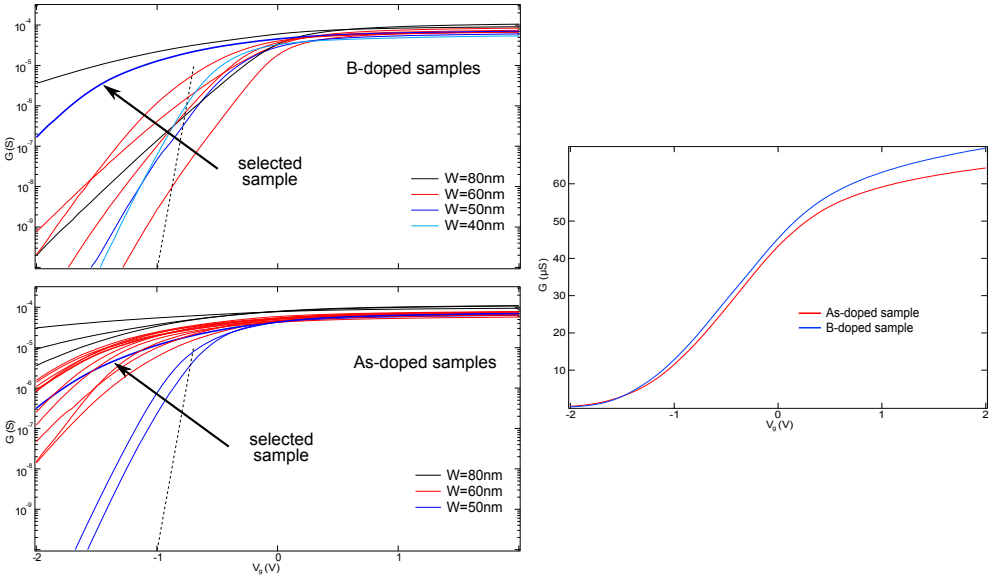

Figure 3.2 *(a) Differential conductance vs.* V_g *for the boron-doped samples. A strong variability is observed, not related with a variation of the width. Most of the sample present a degraded sub-threshold slope compared to the ideal one, represented by the black dotted line. (b) Same characteristics for the arsenic-doped samples. A even more pronounced degraded behaviour than for the B-doped is observed. (c) The two samples measured at low temperature.*

Pierre *et al.* [63] effectively explains this degraded slope by the presence of a dopant in the middle of the channel. Cooling down such a device from 300 K to 4 K results in the presence of a resonant peak under the silicon conduction band. This peak is attributed to transport through a dopant. It is broadened at room temperature and leads to a shift of the threshold voltage towards lower $V_g = -2$V values and a degraded slope according to the usually weak level arm parameter α of the donor ($\alpha = 0.19$ for the donor observed in [63]).

Secondly, we note that the As-doped samples present more degraded characteristics than for the B-doped ones (this can be quantitatively measured taking for example the

average conductance at $V_g = -2V$, which is higher for the As samples). This suggests that there is on average more donors in the channel in the As case. One has to be very cautious with this last statement, as we will see in the following that their position is the channel plays a major role.

Some questions remained open following this work. First, Pierre *et al* didn't fully investigate the role of the donor position in the channel as they were probing only the donors close to the BOX. The question of the double occupation of a single donor also remained elusive in this work. We will investigate these question in the next sections, taking advantage of the back-gate voltage and of numerical simulations.

3.2 Resonant tunneling through dopants

3.2.1 Varying the transverse electric field

We first explain the advantage of having a dual-gate device. With only one front gate, a dopant gets ionized (i.e. its ground level is aligned with the Fermi energy) for a unique value of V_g, corresponding to a fixed environment around the dopant: a certain number of other ionized/neutral donors and a certain electron density distribution in the channel. If we move away from this gate voltage, we will change these parameters but the dopant will also move from the resonant condition, and no current will flow through it. If one wants to change these parameters to study their influence on the dopant, one needs a second gate to keep the electric potential locally constant on the dopant. As an illustration we draw two sketches on Fig 3.3, where two donors (with $E_I = E_{bulk} = 53.7meV$) are placed at different distances from the top and back gates: the dopant named 1 is closer to the top gate than the dopant 2. We consider two situations corresponding to two different couples (V_b, V_g) where the dopant 2 is resonant. In situation (i), with $V_g^{(i)} < V_b^{(i)}$, the dopant 1 is ionized (D^+) and no inversion layer is present at the top gate interface. But in situation (ii), with $V_g^{(ii)} < V_b^{(ii)}$, while B is still at resonant condition, the dopant 1 ground level lies under the Fermi energy and is neutral. One can also note that an inversion layer has been created under the top gate. The environment in the channel dramatically changed between the two situations and this will have a strong impact on donor B properties as seen in the next section. We will see however that these simple schemes, representing a one dimensional picture and neglecting the metallic SD are not sufficient to account for our observations.

We are able to tune the transverse electric field (meaning perpendicular to the SD current) to modify the environment of a donor. Considering only one donor, Verduijn *et al.*[117] shows that a change in the electric field moves the wave function of the electron from the bulk case to an interface-hybridized state. This transition modifies the valley mixing of the ground state and probed by the tunnel current.

On a macroscopic scale, Ono *et al.*[75] studied the effect of the vertical electric field on P doped SOI films. They observe a cusp in the threshold voltage going from $V_b < 0$ to $V_b > 0$, attributed to the ionization of the donors in the body of the channel.

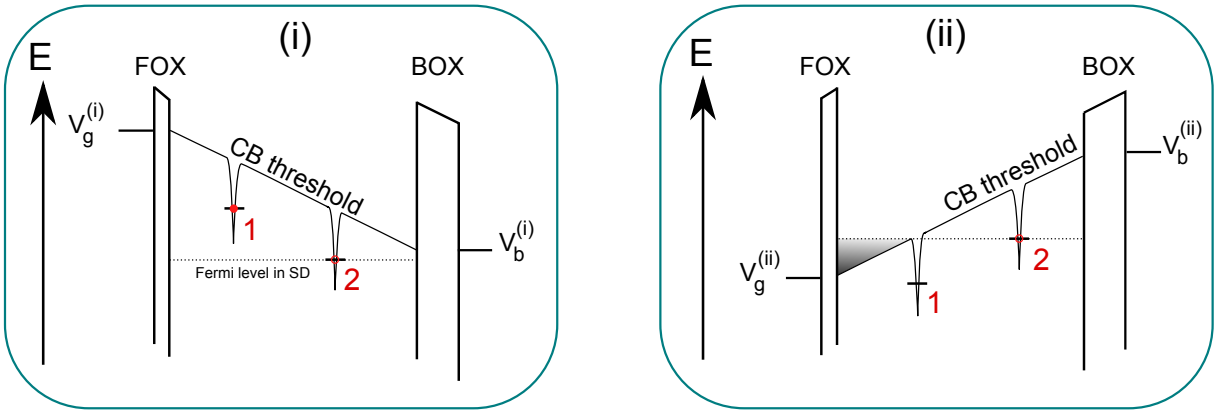

Figure 3.3 *Schemes illustrating the key point of being able to tune the transverse electric field in the channel thanks to the back-gate. From situation (i) to (ii), the dopant 2 remains on resonance but its environment has been dramatically modified: the ionization state of the dopant 1 has changed from ionized to neutral and a 2DEG has been formed under the top gate as the Conduction Band (CB) threshold lies below the Fermi level defined by the reservoirs.*

We aim at making a bridge between these two works, studying the influence of the vertical electric field in a nanoscale device, where only a few donors are implanted. This allows to experimentally investigate the influence of the environment according to the donor position in the channel and also the interactions between donors. From the room temperature measurements we measured two samples, drawn in blue on Fig 3.2, one was boron doped and the other Arsenic doped.

3.2.2 Low temperatures measurements

We start with the As doped sample (sample #4). We have measured the differential conductance as a function of the two gate voltages (V_b, V_g) at 4K with a standard lock-in technique with $V_{ac} = 300\,\mu V$. The result is plotted on Fig.3.4 on a 2D map, similarly to Chapter 2. For those samples, we expect the onset of the conduction band to occur at $V_g = V_{th} \simeq \Delta\phi_i + \frac{E_g}{2|e|}$ for a n^{++} silicon gate at $T = 0\,K$ [112]. $E_g = 0.55eV$ is the silicon band gap and $\Delta\phi_i$ is the work function between the gate electrode and intrinsic silicon, which gives in our case between a n^{++} gate and an undoped body $\Delta\phi_i = -\frac{E_g}{2|e|}$. Finally we obtain $V_{th} \simeq 0$ (for $V_b = 0\,V$). We attribute the onset of the conduction band to the continuum of SD current observed above the broken line, which corresponds to the simulation of this onset discussed below. Contrarily to the devices presented in Chapter 2, here the onset doesn't exhibit isolated resonances: this is due to the very short gate length and the absence of spacers which prevents any confinement of the conduction band electrons. We clearly identify a very pronounced cusp of the onset when going to from negative (where the onset is flat, independent on V_b at $V_g \approx 0.2V$), to positive back-gate voltages where it strongly decrases to $V_g \approx -1V$ at $V_b = 20V$. In the macroscopic case, this cusp arises from the ionization of donors in the body of the channel when a vertical electric field is applied [75].

We can clearly observed resonant transport below the conduction band. These resonances, labelled A, A', B, B', C, C' (the denomination "'" and the numbering will be

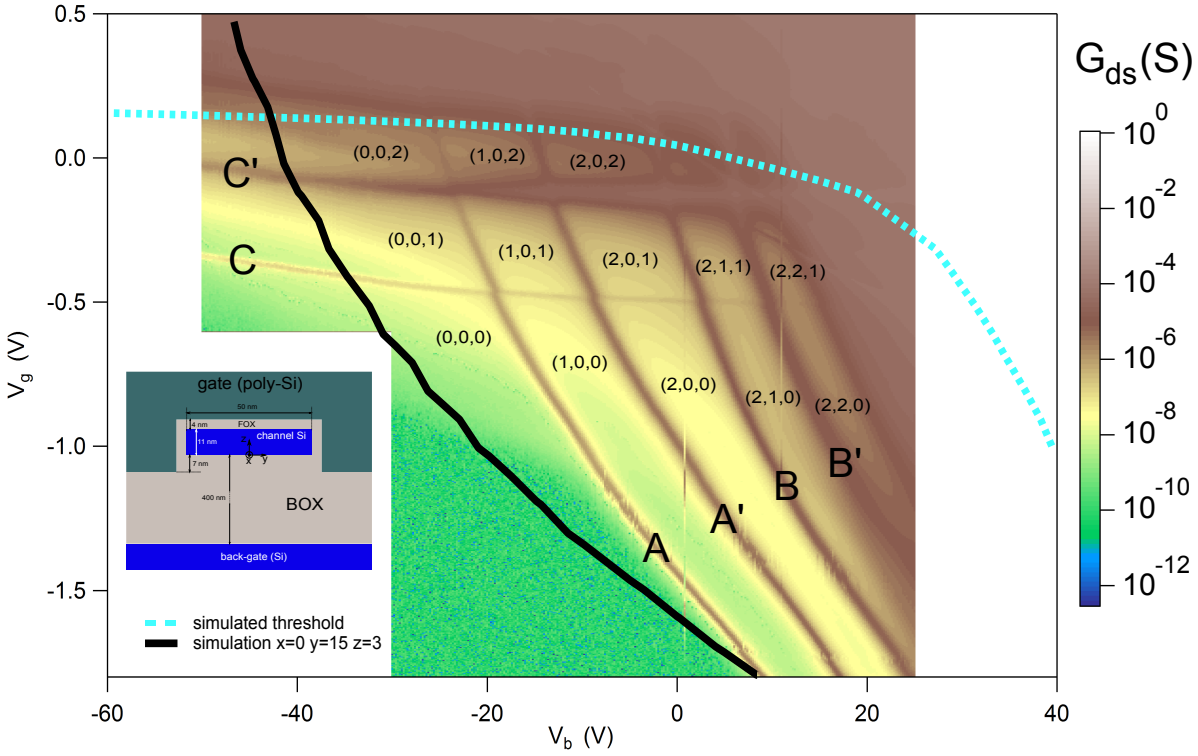

Figure 3.4 *differential conductance (in log scale) vs.* (V_b, V_g) *for the As-doped sample. Inset: scaled schematic view of the sample.*

discussed further) are attributed to resonant transport through donors. First, one can notice that these lines present a completely different curvature compared to the conduction band threshold. Starting from positive V_b, lines A, A',B and B' are parallel to the threshold but then going to negative V_b voltages, they present an opposite curvature to become perpendicular to it and less sensitive to V_g. Lines C and C' don't present any curvature and are almost insensitive to V_b on this back-gate voltage range.

The dopant A ionization line presents a clear upward curvature in the (V_b, V_g) plane, when decreasing V_b. If we take back the formula 1.6 giving the gate voltages conditions (V_b^A, V_g^A) for the dopant to be at resonance, we obtain the linear relation 3.1, with K being a constant depending on the ionization energy of the dopant. Therefore the curvature of the ionization line can't be explained with this simple model assuming constant capacitive couplings, which would lead to straight ionization lines in the (V_b, V_g) plan.

$$C_b V_b + C_g V_g = K \tag{3.1}$$

3.2.3 Comparison with numerical simulations

Donor A actually shows an opposite curvature as compared to the one of the conduction band threshold: it becomes more and more vertical when lowering V_b. This indicates that the donor is gradually screened from the top gate and becomes insensitive to it. This can be qualitatively understood: when one decrease V_b, one has to increase V_g,

not through a linear relation as we have just shown, in order to keep the donor's ground state on resonance. But increasing V_g also leads to an increase of the electron density at the interface between the channel and the FOX, which is responsible for the screening of the gate potential on the donor. Note that for $V_b > -25V$, its ionization occurs in a region where the 2DEG isn't completely formed (because lying under the white dotted line). Still we believe that increasing V_g extends the SD regions creating wings on this FOX interface, which can be seen as precursors of the 2DEG. Hence this electron cloud is responsible for the collapse of the constant coupling model: instead of considering the geometric capacitances as fixed in the whole (V_b, V_g) plan, they evolve in a non-trivial way following the ionization of a dopant. In our geometry, the very proximity of the SD and most importantly their disordered metallic behaviour induce a screening of the electric field which changes significantly with the different gate voltages.

We can reasonably think that the same situation qualitatively occurs for dopant B, according to its ionization line, which presents a similar behaviour. However the situation is much different for the dopant C: it presents an almost horizontal ionization line with no curvature. This means this donor is only controlled by the top gate and no screening effect is observed. Indeed we will see that it presents a much higher α_g, which isn't dependent on the ionization point (see table of Fig. 3.8).

We attribute these different behaviours to different positions in the nanowire. The dopants A and B, which are screened from the top gate at high V_g due to the electronic extensions of the SD close to the FOX interface, but not symmetrically at high V_b must be located close to the BOX. On the contrary, the donor C must rather be located close to the top gate. To perform an accurate tomography through tunnel current remains very difficult due to the microscopic details of the sample, especially concerning the dopant distributions in the SD regions. Nevertheless we have performed 3D simulations of the electrostatic potential as a function of the different electrode voltages in a geometry as close as possible to the real device to help us understand these screening effects and the ionization behaviour of a donor depending of its location in the channel.

Model

To calculate the potential in a three dimensional region requires to solve the 3D Poisson equation. This becomes analytically impossible when several boundary conditions (electrodes, oxides) and singularities (dopants) come into play. Still we can use numerical simulations to estimate the potential landscape in the nanowire as a function of the two gate voltages (V_b, V_g). These simulations were performed in collaboration with Yann-Michel Niquet and Manuel Cobian, working in the SP2M at CEA Grenoble. We used a 3D-Poisson solver combined to a Debye-Hückel model for the silicon nanowire to compute the potential in the device. This is a continuous model, where singularities in the potential arising from the presence of dopants are absent. Instead we take into account a continuous concentration of dopant corresponding to the expected number of dopants within the channel volume. The ionization of donors at the edges of SD is also explicitely considered in the simulation in a mean-field approach, therefore neglecting Kondo and Fermi-edge singularity effects.

In order to know the ionization state of donor, we locally compare this simulated potential to the ionization energy (we took the bulk value 53.7 meV at first order) of an arsenic atom. A dopant at a given position is then ionized (*i.e.* D^+) if the potential at this position is higher than the ionization energy of the dopant:

$$|e|V(\vec{r}) > E_I(\vec{r}) \tag{3.2}$$

Finally we repeat this procedure for various (V_b, V_g) couples, allowing us to follow the ionization state of the dopant.

Lonely dopant

We start with the most basic example, which is a single donor in the channel. It is placed at the position (x=0, y=15, z=3 nm), where x represent the distance from the middle of the channel along SD direction, y is the transverse direction and z is the vertical position (z=0 is the BOX interface,see the inset of Fig. **??**). As for the experimental measurements, we draw a 2D map versus V_b and V_g and identify the points where the state of the donor changes. We obtain a line in this plot, shown in black in fig 3.5. Crossing the black line while increasing V_g, the donor will go from ionized (D^+) to neutral (D^0) state. We also represent with the blue dotted line the onset of the conduction band, when the electron density reaches 10^{11} cm^{-2}, this value being equivalent to 1 electron in the channel.

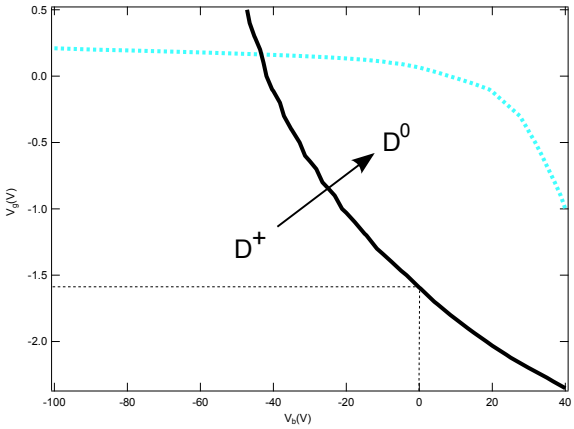

Figure 3.5 *Simulated ionization of one donor located at (x=0, y=15, z=3) as a function of* V_b *and* V_g*. From below to above the black line, the state of the donor changes from* D^+ *to* D^0*. The position in* (V_b, V_g) *as well as the curvature of this line almost corresponds to the ionization measured for the donor A and B. The blue dotted line represents the onset of the conduction band, with an electron density of* 10^{11} cm^{-2}

For this donor's position, we recover the main properties for the evolution of the ionization as a function of the electric field. First, the values in the (V_b, V_g) plane almost correspond to the ones observed experimentally: at $V_b = 0\,V$, the donor gets ionized around $V_g = -1.5\,V$. Secondly we also recover the curvature of the ionization line in the (V_b, V_g) plan. Going to negative V_b values, the lines becomes almost vertical, meaning

that the donor becomes almost insensitive to the front gate voltage. However for the simulated donor, the curvature seems to be constant in the whole V_b range, whereas in the experiment, the ionization line seems to become a straight line, parallel to the conduction and threshold for $V_b > 10\,V$. This seems to indicate that in the simulation, the donor is gradually screened from the back-gate, which is not the case, or in a smaller amount in the experiment.

We will now investigate the influence of the donor position on its ionization and try to reproduce the behaviour of the donor C.

3 dopants with different position in x

We now add two other donors in our system. We place them at several positions around the first dopant, discussed above, in order to understand the role of each dimension of the problem. For a several dopants system, degeneracies can appear when two dopants get ionized for a same couple (V_b, V_g). We then also take into account the Coulomb repulsion between dopants to lift these degeneracies, as one usually does for a double-dot system.

To begin we put them at the same y and z coordinates (y=15 nm and z=3 nm) but we change the x coordinate: the "red" dopant is placed at x=3 nm (closer to the drain) and the blue at x=-5 nm (closer to the source). Fig 3.6 shows the ionization lines for such a configuration. It is striking to observe that one obtains parallel ionization lines, all presenting the same curvature as for the single dopant simulation and for lines A to D in the experimental measurement. The derivative of those lines, giving access to the ratio C_b/C_g, is then unaffected by a change in the x position. Therefore we understand that these donors have the same couplings to the gates, which is reasonable as their distances to the front and back gates are the same.

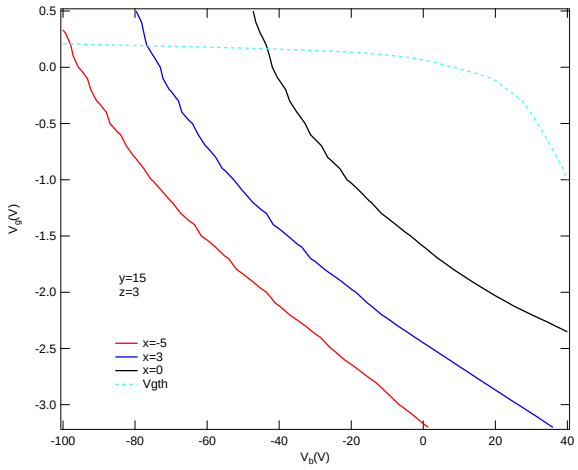

Figure 3.6 *Ionization evolution in the* (V_b, V_g) *plan for 3 donors located at different x coordinates. The lionization lines run parallel to each other. The light blue dotted line represents the onset of the conduction band.*

3 dopants with different position in (z,y)

We now move these two dopants around the first one, and especially change their distances to the gates. One can observe on Fig 3.7 that this dramatically affects the curvature of their ionization lines. They become completely horizontal for the red donors, which are the closest from the front gate (with coordinates ($y = 23\,nm$ and $z = 12\,nm$). This means that the coupling to the front gate is increased as compared to the other capacitances of the problem. One can notice that this effect is enhanced for the position variation in the z direction, which is reasonable because we also moved the donor away from the back gate and decreased C_b.

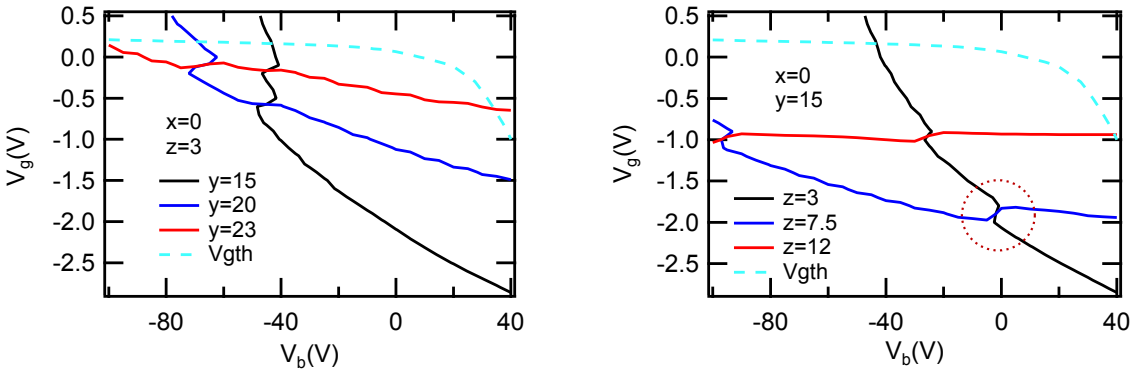

Figure 3.7 *Simulated ionizations lines for three donors located at different y (left) or z (right). The ratio C_b/C_g decreases when the donor is closer to the top gate.*

Beyond the constant coupling model

A first correction to the CCM is actually to come back to the original definition of the level arm parameter α and then to make assumptions on the system. α expresses the local energy variation (here, "local" means on the donor) when one sweep a gate voltage. Therefore we can define two different α parameters α_b and α_b defined as following:

$$\mathrm{dE} = \alpha_\mathrm{g}(\mathrm{V_b}, \mathrm{V_g})\mathrm{dV_g} + \alpha_\mathrm{b}(\mathrm{V_b}, \mathrm{V_g})\mathrm{dV_b} \tag{3.3}$$

We focus on α_g which is more coupled to the donors, due to thin front oxide (4nm) compared to the buried oxide (400 nm). The only measurement we have access to is the resonant current through the dopant. We measure α_g according to the following method: we measure the ionization of the dopant vs. $(\mathrm{V_b}, \mathrm{V_g})$ applying a finite bias $\mathrm{V_d} = 10\mathrm{mV}$. The gate voltage difference $\Delta\mathrm{V_g}$ between the edges of the corresponding diamond (as shown on fig 3.9 (a) for example), gives directly access to the level arm factor:

$$\alpha_\mathrm{g} = \frac{\mathrm{V_{DC}}}{\Delta\mathrm{V_g}} \tag{3.4}$$

This last equation assumes that α_g is constant over this V_d range: this is valid according to the diamonds plot presented in Fig. 3.9, with straight line edges from 0 to, at least, 10 mV. We estimate the accuracy of this method to be better than 10% for α_g. We performed this dependence from $V_b = -18$ to 15 V. For lower voltages, the measurement is perturbed by the crossing with C and for higher voltages, the ionization occurs for $V_g < -2.2$ V, with a high risk to break the oxide layer.

We only measured this factor at the resonance: we then plot its dependence versus V_b^* in fig 3.8, with V_b^* meaning that we also change V_g along the ionization trajectory in the (V_b, V_g) plan. α_g drops by a factor of two going from $V_b = 15$ V to $V_b = -15$ V, where the dopant is screened from the front gate. This is consistent with the upward curvature observed for the ionization line. This result is surprising: at first, we could expect that decreasing V_b would push the electron towards the top gate and then increase α_g.

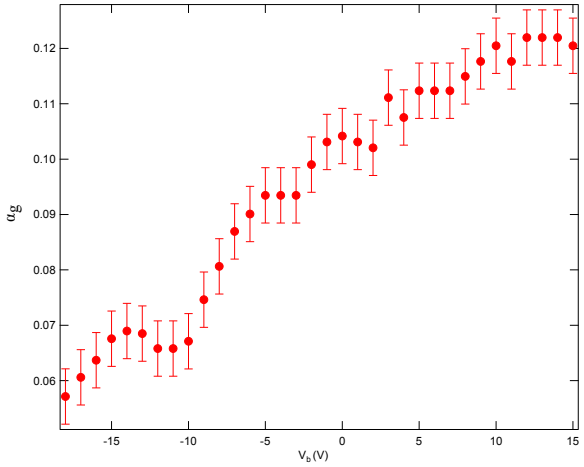

Figure 3.8 *Evolution of the α_g parameter for the donor A as a function of Vb*

We can confirm these qualitative results by studying the evolution of the different capacitances for the donors A and E as a function of V_b. We remind that these ratios are only valid for a small (V_g, V_d) range around each different V_b. We plot in Fig 3.9 four diamonds at respectively $V_b = 15$, 10, 0 and -15 V (resp. (a),(b),(c),(d)) for the donor A and two diamonds for the donor C at $V_b = -15$ and -30 V ((d) and (e)). These were measured at 4 K with an a.c. excitation of 300μV, except for (c) which is measured at 1 K with a 100μV $-$ excitation. As we have seen in Chapter 1, we can deduce the capacitance ratios C_g/C_s, C_g/C_d and α from the edges of these diamonds by calculating the slopes of the white dotted line for (a), shown as an example. This has been done for each plot and then we summarise the different ratios in the table (f). The diamond (c) was recorded during a different run from (a) and (b) (with a thermal cycling in between), with inverted source and drain. Still we can identify the same pattern of lines running parallel to the edges of the diamonds than (a) and (b) but in the opposite bias and direction (see for example the black dotted line in these diamonds).

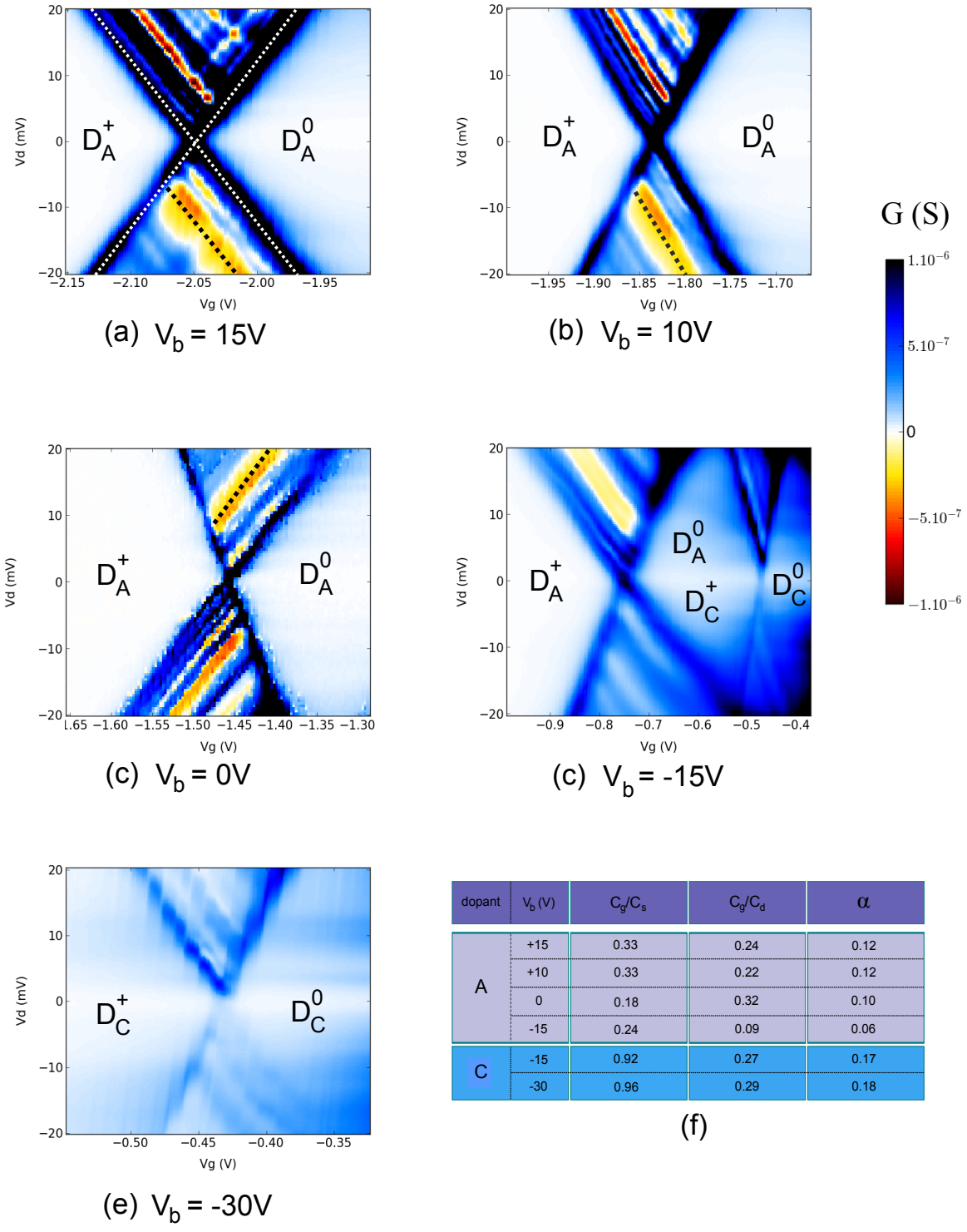

dopant	V_b (V)	C_g/C_s	C_g/C_d	α
A	+15	0.33	0.24	0.12
	+10	0.33	0.22	0.12
	0	0.18	0.32	0.10
	-15	0.24	0.09	0.06
C	-15	0.92	0.27	0.17
	-30	0.96	0.29	0.18

(f)

Figure 3.9 *(a)-(c) Diamonds (in differential conductance) vs.* (V_b, V_g) *for the donor A at four different back-gate voltages (d) diamond of donor C at* $V_b = -30\,V$*. From the edges of the diamonds at low bias voltage we extratc the different coupling ratios and the* α *parameters.*

We first discuss the evolution of donor A. Of course we recover that α_g decreases with V_b as previously discussed. We also observe that the ratios C_g/C_s and C_g/C_d decrease.

This is also a signature that there is a loss of gate control as compared to the coupling to SD when one decreases V_b. It is also striking to notice that this screening isn't symmetric with respect to the flatband condition $(V_b, V_g) \sim (0, 0)$: we could expect for $V_b > 10V$ for the ionization line to become quasi horizontal, as the result of the screening from the extensions of the SD, created here rather at the BOX interface. Instead we observe that the ionization rather seems to run in parallel to the threshold voltage, meaning that we keep a good electrostatic control by the back-gate. This behaviour corresponds to the interfacial regime described by Rahman *et al.* [87] (see Chapter 1). For the donor C, we measured a higher α parameter, around 0.17. The ratios C_g/C_s and C_g/C_d are also higher than for donor A. Its ionization line is almost horizontal ans does not seem to be affected by the creation of the 2DEG at the BOX interface for $V_b > 0$. Therefore we conclude that this donor C is also in the interfacial regime but at the front gate interface.

Anti-crossings between donors

A second point is also enlightened thanks to the simulations showing the ionization lines of donors with different y and z coordinates. On can observe degeneracy points, where two atoms get ionized for a same couple (V_b, V_g). We represent such anti-crossings in Fig.3.10, one extracted from the experimental measurements on the left, between donors A and C, and one extracted from the simulation on the right (circled point in Fig 3.7. Due to the Coulomb repulsion between the two donors, the ionization lines are shifted after crossing the triple point. This shift, expressed in terms of front gate voltage, is given by the following formula:

$$\Delta V_g^i = \frac{U_{ij}}{\alpha_g^i} \tag{3.5}$$

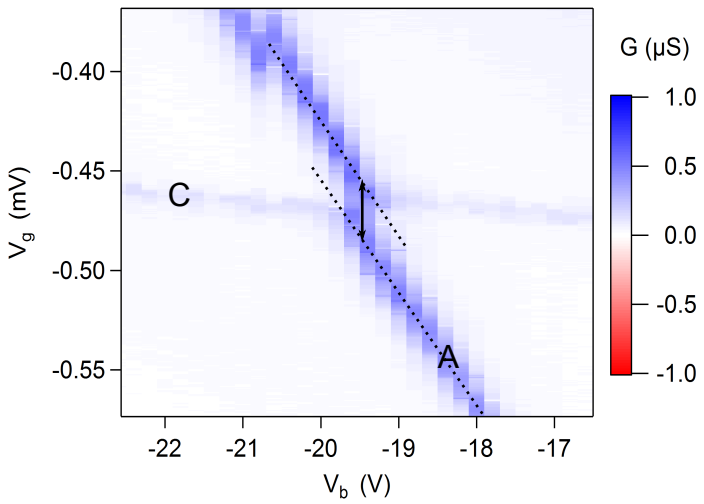

Figure 3.10 *Zoom on an experimental anti-crossing between the donors A and C. We can extract the mutual charging energy, corresponding to a screened Coulomb interaction between the donors.*

where U_{ij} stands for the screened Coulomb repulsion between the two electrons i and j (screened by the nearby gates and SD), then translated into gate voltage with

the respective alpha parameters alpha_g^i. The shift direction can also be understood: at $V_b = -10\,V$, the dopant A (in black) gets ionized when the donor A (in blue) is already in the neutral state(D^0). But at $V_b = +10\,V$, the situation is inverted and A gets ionized when B is still positively charged (D^+), and then benefits from this attractive potential for an electron, lowering its ground state. We can also observe such anti-crossings in our device as between A and C. From the experimental anticrossing on Fig. 3.10, we calculate a mutual charging energy between donors A and C of about 1.5 meV (taking $\alpha = 0.06$ for this back-gate voltage.) If one takes the bare Coulomb interaction, we could deduce the distance between these donors thanks to :

$$r_{AC} = \frac{e^2}{4\pi\epsilon_0\epsilon_{Si}E^{bare}_{Coulomb}} = 82\,nm \tag{3.6}$$

This result suggests that the donors would be located at the complete opposite edges of the channel, which is rather improbable as the donor A is expected to be rather centered in the channel, close to the BOX. More likely the bare Coulomb interaction is screened by the SD electrodes, distant by at most 5-10 nm of silicon from each donor, or by the gate(separated from the channel by the 4 nm-thick SiO_2 gate dieletric.

3.3 Double occupation of the donors

3.3.1 Parallel ionization lines

According to the simulation results we can attribute ionization lines to donors and deduce the relative position of the donors responsible for the six ionization lines of Fig. 3.4, named A,A',B,B',C,C', with respect to the FOX and the BOX.

A striking observation on Fig. 3.4 is that the A-A' then B-B' then C-C' ionizations lines run approximately parallel to each other. Couples of parallel lines can be due either to:

- 2 separate donors, differing by their distance x to the SD electrodes (with y and z constant) as in fig. 3.6.
- the double occupation of a single donor (As^+/As^0 and As^0/As^-) ionization lines, separated by the intra-donor charging energy.

We consider that the 3 couples of lines running exactly parallel to each other will be very rare for a 6-donor configuration. Therefore we attribute the 3 couples of lines to the double occupation of 3 separated arsenic donors. We will now develop this point, extracting the charging energy of the donor according to their position in the channel.

The shape of the ionization lines A-A' and B-B' indicate two donors near the BOX and centered in the channel, *i.e.* small y and z. By contrast lines C-C' are attributed to a donor close to the front gate (large y or z as the red lines in fig.3.7). The shift between A and B can have its origin in a small variation (of a few nm) of the distance to SD electrodes, as shown in Fig. 3.6, which changes the lever arm parameter.

3.3.2 Charging energies

The strong electric field in the channel combined with the small number of donors also makes more likely to populate the As^- state of a donor rather than the ground As^0 state of another distant donor. We estimate the energy separation $\simeq$ 50-60 meV between the ground state for the two donors A and B ionized at V_b=10 V. This separation can be due to the large electric field in the region separating the two donors. In our simulation such a separation in energy is obtained for two donors with the same E_I but separated by few nanometers only: at V_b=10V, $\Delta V_g \simeq$=0.7V for x=0 and x=3nm (see fig. 3.6). Taking into account a level arm factor of about 0.1, we estimate an electric field in the SD direction about 20 mV/nm. A more careful study of the electric field in the 3 dimensions from the simulation is on-going.

Fig. 3.11 shows the diamonds for the donor A and B at $V_b = 10\,V$. They provide a direct measurement of the energy separation between ionization lines A/A' (a) and B/B' (b), attributed to the charging energy E_C. This measurement corresponds to the V_d value at the tip of the rhombus separating to ionization regions: 31 ± 2 meV for A-A' and 21 ± 3 meV for B-B'. For C-C' we can only provide an underestimation $E_C \geq 30$ meV for the charging energy because the lack of contrast of the second resonance is too close from the threshold. The lever arm parameter is smaller for A' than for A : we found $\alpha_g^A = 0.12$ and $\alpha_g^{A'} = 0.08$ for this back-gate, meaning that As^- is more strongly coupled to SD than As^0. Either the electronic orbital for the less bounded As^- is more extended towards the SD and the SD themselves are more extended at higher gate voltage. The differential conductance lines appearing at finite V_d are due to local density of states fluctuation in the SD [80]. Their patterns are approximately identical for A and A' but they are smoothed for A' due to the lower lever arm parameter. We can also extract the level arm parameter for B and find $\alpha_g^B = 0.04$, lower than α_g^A. Here only the larger extensions of the SD at this higher front gate voltage accounts for this reduced level arm factor, increasing C_s and C_s with respect to the gate C_s.

Several conclusions derive from our observations: first the doubly charged state exist for the 3 donors. Second, the charging energy depends on the actual donor. This is expected as the mesoscopic environment influences both the binding and the charging energies. The dielectric confinement or the presence of nearby metallic electrodes make both E_I and E_C fluctuating. Third the measured E_C is much smaller than the ionization energy for As donors in bulk ($\simeq$ 51 meV). The double occupied state is well separated from the conduction band threshold in the channel (see for instance the large separation between the A' line and the conduction band) meaning that the double occupied state of a donor is more stable in our nanostructure-in presence of a strong electric field- than in the bulk case. Finally the charging energy does not significantly depend on the electric field controlled by V_b, as the pair of ionization lines run parallel. According to [85], this indicates that the electric field is always large in this V_b range, before these donors get screened from the front gate for $V_b < -15\,V$. Thus the single and doubly occupied states are mainly surface states.

The stability of double occupied state on shallow donors in presence of interface has

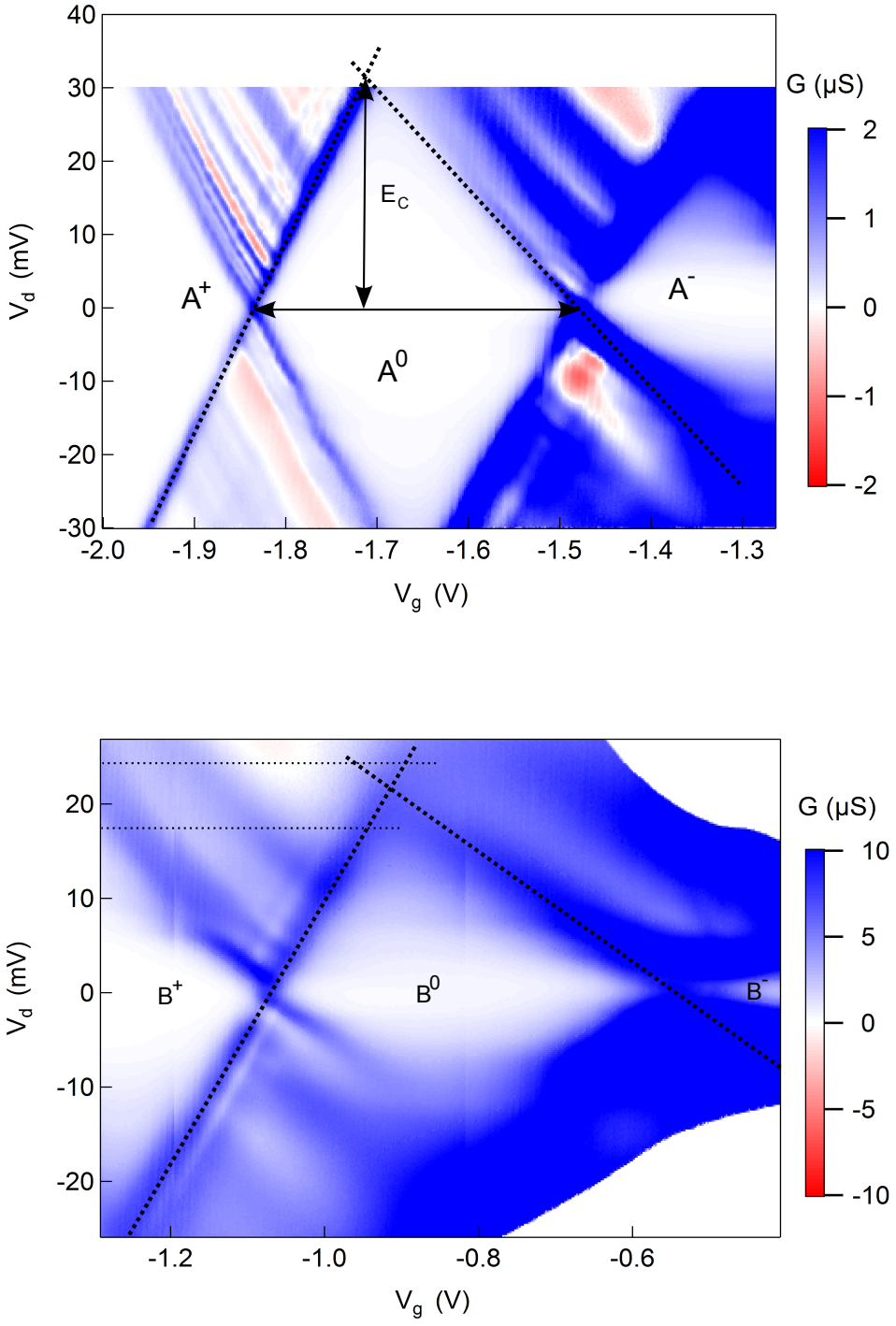

Figure 3.11 *Estimation of the charging energy for the donor A, from the SD differential conductance plotted vs.(Vd, Vg).*

been the subject of intense research citeHao2009,Calderon2010,Hao2011. Several differences are expected compared to the bulk case similar to the H^- ion as we have seen in Chapter 1. A reduced charging energy can be due to the screening by a metallic gate electrode separated from the silicon by a very thin dielectric barrier [14, 39, 117]. The predicted effect should be small in our case where the gate oxide is 4 nm-thick. Moreover the

binding energy for the doubly occupied state is predicted always very small. The donors are always more capacitively coupled to the SD than to the gate in our geometry (see above) and the screening by the SD electrodes [77] should be important. The charging energy can also be reduced if the donor state is hybridized with a Si/SiO_2 surface state in the presence of a strong electric field [88]. The electric field pulls the electron cloud away from each other and if the first electron is put in the interface state, the second electron still feels the full attractive potential of the donor, contributing to lower the charging energy. This is consistent with our results but does not include the screening effects which can further decrease the charging energy. Overall, we find a good agreement with other experimental values, as measured by Lansbergen *et al.* [58] over six donors from different devices, between 29 and 31 meV. On the contrary, Fuechsle *et al.* measured in a single atom device STM designed by STM a charging energy of 47 ± 3 meV, a value much closer to the bulk value. This suggests that the environment of a MOSFET always leads to a decrease of the charging energy because of the electric field and of the screening from the SD and the leads.

Finally, we describe the charging sequence of the hybride states. At such high electric fields, an As ion located a few nanometers from the interface is always ionized. It creates a local positive potential which forms a donor-induced potential deep at the interface to attract an electron and form the singly occupied state As^0. It is important to notice that the first electron *does not fully screen the* As^+ *ion but rather forms a dielectric dipole with it* (transverse to x). This dipole produces a local attractive field which is larger than the screened central potential which would results from the singly occupied state in absence of electric field. The doubly occupied state As^- is then stabilized. This scenario explains also why the lines A and A' run parallel to the conduction band edge at large positive V_b, because the interface 2DEG and the Coulomb island have exactly the same coupling to the substrate and to the front gate. Both effects- the shift of the electron under large transverse electric field (along y,z) and the screening by the SD electrodes (along x)-explain the reduction of the charging energy and the stabilization of the As^- state. A full simulation is lacking for a more quantitative analysis.

Nevertheless we have tested the reproducibility of such devices by cooling down and performing again the measurement on the very same device than ref[80], which is a Boron doped device (no As pre-doping channel). We have performed the same measurement, the differential conductance vs. (V_b, V_g) and plotted it in Fig. 3.12. For this sample we can also identify curved ionization lines, which are then attributed to resonant transport through individual donors. However, there are more lines in this sample than in the As-doped device presented before. Even if some o these lines also run in parallel here, it is more difficult to identify the double occupied state of a donor.

The studied case of few electrons on few donors inside a MOSFET channel is strikingly different from the case of lightly doped compensated macroscopic semiconductors where there is no screening by electrodes [22]. For energies between -E_i and $\simeq$-3 $\times$ E_i (E_i is the binding energy for isolated donors), Efros and Shklovskii have shown that long range fluctuation effect dominates over the immediate environment charge (for a Poissonnian distribution of donors)[23, 22]. Thanks to the efficient screening by SD electrodes in our

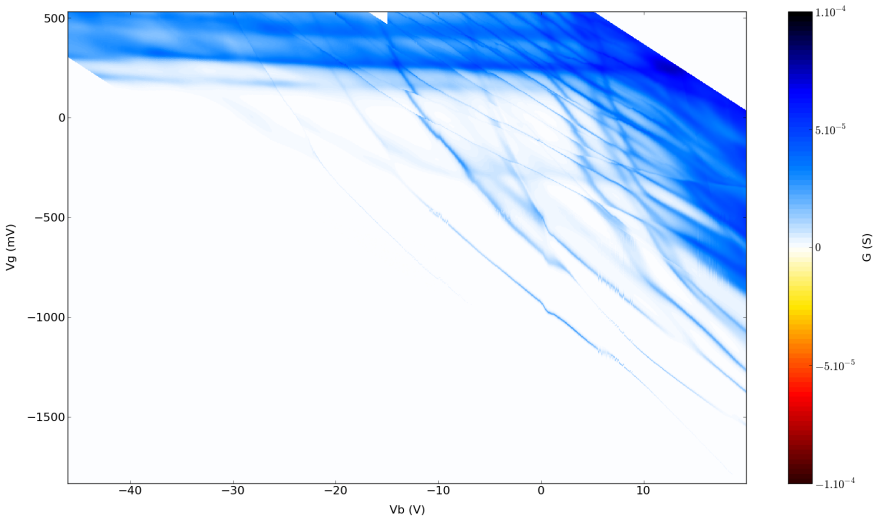

Figure 3.12 *Differential conductance for the B doped device.*

geometry, it is possible to avoid the complexity arising from the many body problem of a Coulomb glass, and to treat the charging of a specific donors taking the ionization state of other donors constant over a large gate voltage range- and numbering the stability diagram (see fig.3.4). This complexity can be a serious obstacle to the scaling of devices even with a moderate number of dopants.

Chapter 4

Coupled-atom transistors

Contents

Introduction

We present in this Chapter the main results obtained concerning the first Coupled-atom devices in silicon. The first part will present results of process simulations, which will help us to understand how the donors can diffuse from SD to the channel. The second part will focus on the spectroscopy which can be done with thanks to a two-atom device. This will allow us to draw a comparison with results obtained in Chapter 2 on the valley-orbit splitting of corner states.

4.1 Doping the channel

4.1.1 Channel pre-doping and diffusion

We come back on the section 1.1.4 which has described the main fabrication steps of a device. Here we focus on the dopant implantation and detail the different paths to obtain single donor devices. According to the actual CMOS technology, two main paths can be chosen:

- Before the channel etching step, we can perform a pre-doping step with any type of dopant (n-type with phosphorous or arsenic or p-type with boron atoms). We can choose the dose to obtain any desired dopant concentration in the channel, homogeneous in the whole Si film.
- After the gate and the spacers etching steps, high dose of As donors are implanted in the Si film to further create the SD reservoirs. Normally, any dopant implanted at this stage should then not be present in the channel, as the gate and the spacers protect this latter. But some donors can stochastically diffuse towards this region during an annealing step as described below. We will also see in the following that unusual device geometry and dopant implantation techniques give us some control over this process.

Usual ion implantation systems create ion beams with an energy varying between a few keV and tens of keV. From these high energies arise two challenges. First defects, as vacancies for example, can be created when the ions penetrate the Si film. Secondly one has to control the final position of the ions for all of them to be located in about a 10 nm-thick film. This represents a strong restriction on the ions final vertical position, which has to be very accurate. In order to fulfil these conditions, sacrificial oxide layers, with about a 5 nm thickness are deposited on the Si film before each implantation step. These layers will lower the energy of the ions before entering the Si film. This will prevent the creation of defects and also allow for a precise location of the final position of the atom as this energy lowering is performed very close to the Si film. As a result we plot in Fig. 4.1 the simulated concentration of dopants in a 20 nm-thick channel, after an implantation done at 30 keV, with a dose of 3.10^{12}cm^{-2}. We can observe a bell-like concentration evolution, with a maximum in the middle of the film. These sacrificial layers are then removed.

The donors are not inserted in substitution sites during the implantation, but are located in vacancies. To insert the donors in substitution of silicon atoms, an annealing

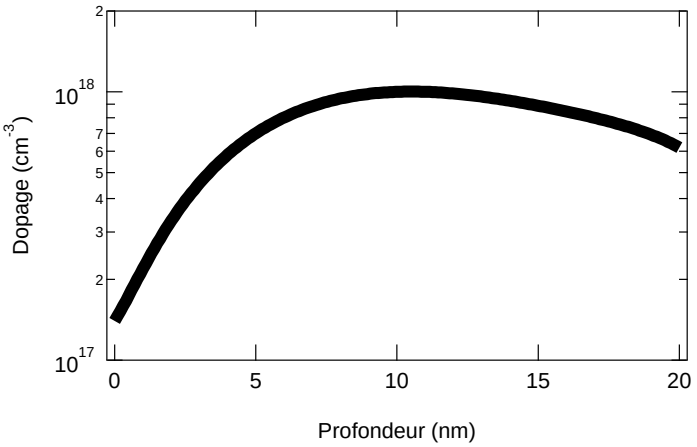

Figure 4.1 *Simulation of the dopant concentration profile in a 20 nm-thick Si film, with an initial 30 keV ion beam energy. 5 nm of* SiO_2 *and 5 nm of* Si *were used as sacrificial layers.*

step around 1000°C is performed. A drawback of this high temperature is to also induce a diffusion of the dopants in the three dimensions, and especially towards the edges of the film. To limit this effect, the annealing time doesn't exceed a few seconds. During this step the dopants can diffuse from the SD towards the middle of the channel as for the As atoms present in the channel of the boron-doped device described in Chapter 3.

We have investigated in Chapter 1 and 3 the strong influence of the donors position on its properties. Process simulations will give us a further analysis of the distribution of the dopants positions in the nanowire.

4.1.2 Kinetic Monte-Carlo simulations

We have performed atomistic simulations of the dopant diffusion using Kinetic Monte-Carlo (KMC), module of the Sentaurus Process software. This was done by O. Cueto and B. Sklénard at LETI. These simulations are three-dimensional and include all the implantation and thermal steps causing the final dopant distribution. First, following the work done in ref [80], we have simulated the final dopant profile for this boron-doped sample. The result is presented in Fig. 4.2 showing different views of the device. The boron atoms, represented by the green spheres, don't participate to transport as the leads are p-type, but just cause a shift in the threshold voltage of the transistor. But one can also identify As atoms, represented with red spheres, which have diffused from the SD towards the middle of the channel. This diffusion results in the channel to be effectively reduced from 20 (nominal length) to 10 nm leading to strong screening effect as mentioned in Chapter 3. The concentration of Boron atoms is rather homogeneous in the whole channel (under the gate and in the contacts) whereas concerning the As atoms, their concentration is above the Mott transition in the SD (to create the contacts) but only a few atoms can be identified under the gate. This proves the protecting role of the gate (no spacers were grown for this devices) against a massive implantation of As donor in this region. As for the few remaining As atoms, they illustrate the impact of the diffusion during the annealing step.

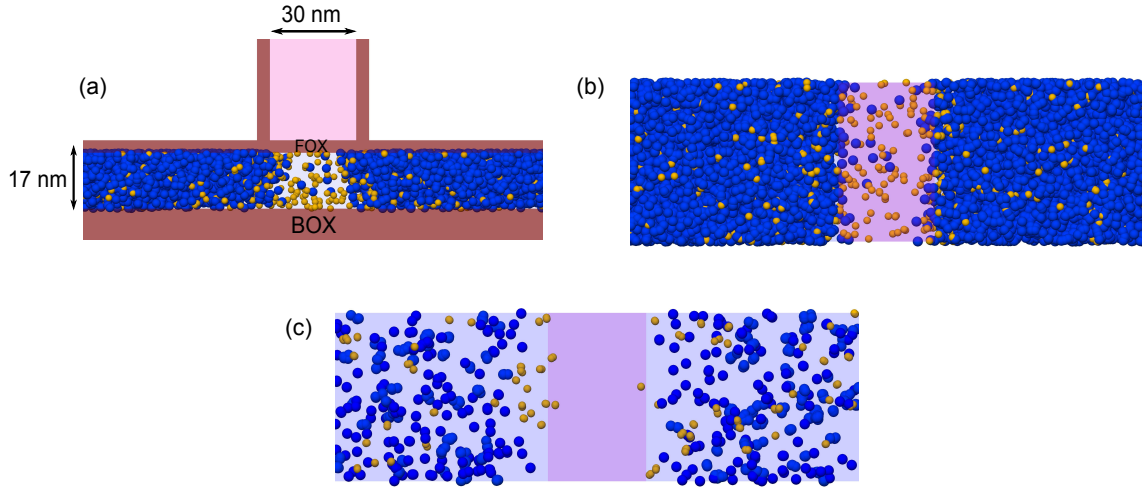

Figure 4.2 ***KMC simulations of the fabrication process*** *(a) Cut view along the channel. The As atoms, which diffused from the source an drain to the center are represented with blue spheres. The green spheres represent the B atoms. (b) Top view, same representation (c) Top view of the channel, representing the B (green) and As (blue) molecular systems (i.e. two atoms closer than their Bohr radius). No As cluster has been identify under the front gate (thus which could contribute to current) over the 150 simulations of the process.*

We took a look into the statistical properties of this diffusion phenomena running 150 simulations of the same device with different random seed numbers to obtain different numerical realizations. This allows us to draw the histogram, represented in Fig 4.3, of the number of As donors present in this region, meaning in a box whose dimensions are the device's ones for the thickness and the width and 17nm-long (blue dotted line). We have fitted this histogram with a Poissonian law, with the following probability mass function:

$$P(k \in \mathbb{N}) = e^{-\lambda}\frac{\lambda^k}{k!} \tag{4.1}$$

λ represents the average value of the number of As atoms and is found to equal 3.7 ± 0.1. This fit is represented with the red points on Fig 1.2. Only 3 simulations present no dopant and one can observe up to 8 dopants which have diffused into this box.

Furthermore, one can extract from the final atomic positions the mean distance between dopants as well as the nearest neighbour for each one. The mean distance between dopant obviously corresponds to the concentration of dopants (8 dopants for this simulation) within the volume of the chosen box. No simulation presents a situation with two dopants close to each other by less than 4 nm, therefore less than the Bohr radius of the atom ($2nm$). We consider that no As cluster is present in our system, meaning we remain in a dilute regime with no molecular state which is formed.

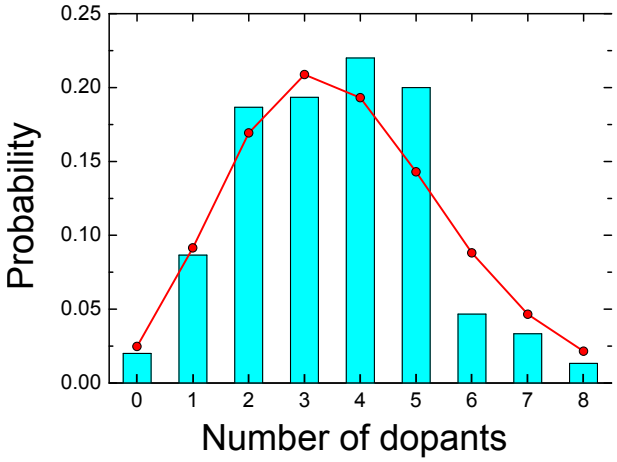

Figure 4.3 *Histogram of the probability to find N dopants in the channel at the end of the process. A Poisonnian fit gives on average around 4 dopants ($\lambda = 3.7$). No simulations show more than 8 dopants.*

4.1.3 Tilted implantation on dual-gate devices

Finally we have two last available parameters. The implantation is never performed perpendicularly to the nanowire but with an angle in order to avoid ion collimation. This angle can be varied as well as the direction with respect to the device. We present the effect of these parameters on a specific device geometry presented on Fig. 4.4. This scanning Electron Micrograph showns the gate which usually surrounds the whole nanowire is here splitted into two gates V_{g1} and V_{g2}. The gate length is 40 nm, the width 60 nm and the Si thickness 20 nm. Here the distance between the two gates was set to 30 nm, which corresponds to twice the thickness of the spacers, which one can identify in light grey around the gates.

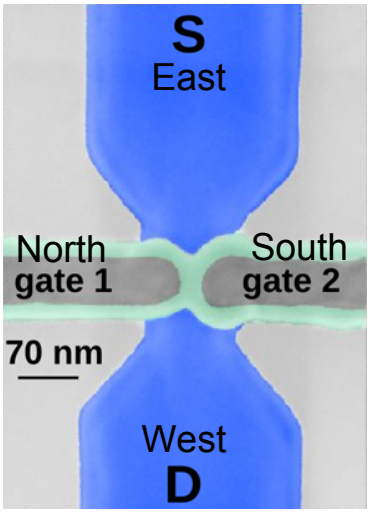

Figure 4.4 *Scanning Electron Micrograph of a dual gate device. Two gates, facing each other, surround the nanowire.*

We have also investigated the channel doping profile of such devices with KMC simulations. The results are presented on Fig. 4.5. The angle of the implantation can be 7°

or 55°[1]. This tilted implantation can be performed along two directions: either along the North-South direction(case (a))or along the East-West direction (case (d), *i.e.* in the SD direction). In the first case the channel under the gate remains undoped (apart from a channel pre-doping), as the direction of the implantation and of the gates are the same. However in the second case, the implantation angle allows for the donors to penetrate under the spacers and the gate.

These effects are illustrated thanks to the device simulations (b),(c),(e),(f) and (g) corresponding to different situations. (b) and (c) correspond to the case of a North-South doping with a 55° angle. The As atoms are represented by the blue spheres. In both cases, differing by the gates separation length (35 nm for (b), 30 nm for (c)), no As atoms is present under the gates and the spacers around them (not represented). We can only observe a limited diffusion of the donors at the edges of the reservoirs. For (c), a phosphorous pre-doping was performed and we can indeed observe these donors (red spheres) in the whole channel. The results are completely different in the case of an East-West implantation along SD ((e) to (g)). First, we note that a small angle (7°, (e)) induces a tiny effect of the doping profile, as it almost follow the shape of the spacers. However if we increase this angle to 55° (f) (with a boron-pre doping, green spheres), we can see the donors start penetrating the middle of the channel. Finally there is a strong impact of the distance between the the gates for this angle and implantation direction: on (g) it has been increased to 35 nm, resulting in the creation of two donor tip-shaped profiles pointing towards the middle of the channel, again between the two gates. Finally, we can also focus on the donors which have diffused far away from the SD.

The doping profile difference between between the configurations (b) and (g), which only differ by the implantation orientation is striking with the creation of this donors tips in the latter. However in reality, those devices remain challenging to fabricate for the microelectronics: one needs a perfect alignment of the two gates on the nanowire in order for both of them to control the electrostatics of the channel. The distance between the two gates is also not as accurate as for simple gates, which can become dramatic as we have shown. Nevertheless we believe that the combination of this tilted implantation techniques and of such complex device geometries open new perspectives to investigate the role of the reservoirs in these atomic scaled devices. In the following we will develop low temperature measurements performed on samples corresponding to the simulations (c) and (f).

[1]The implantation is actually done in two steps with a 180° horizontal rotation of the wafer between them. This insures a symmetric doping of the SD.

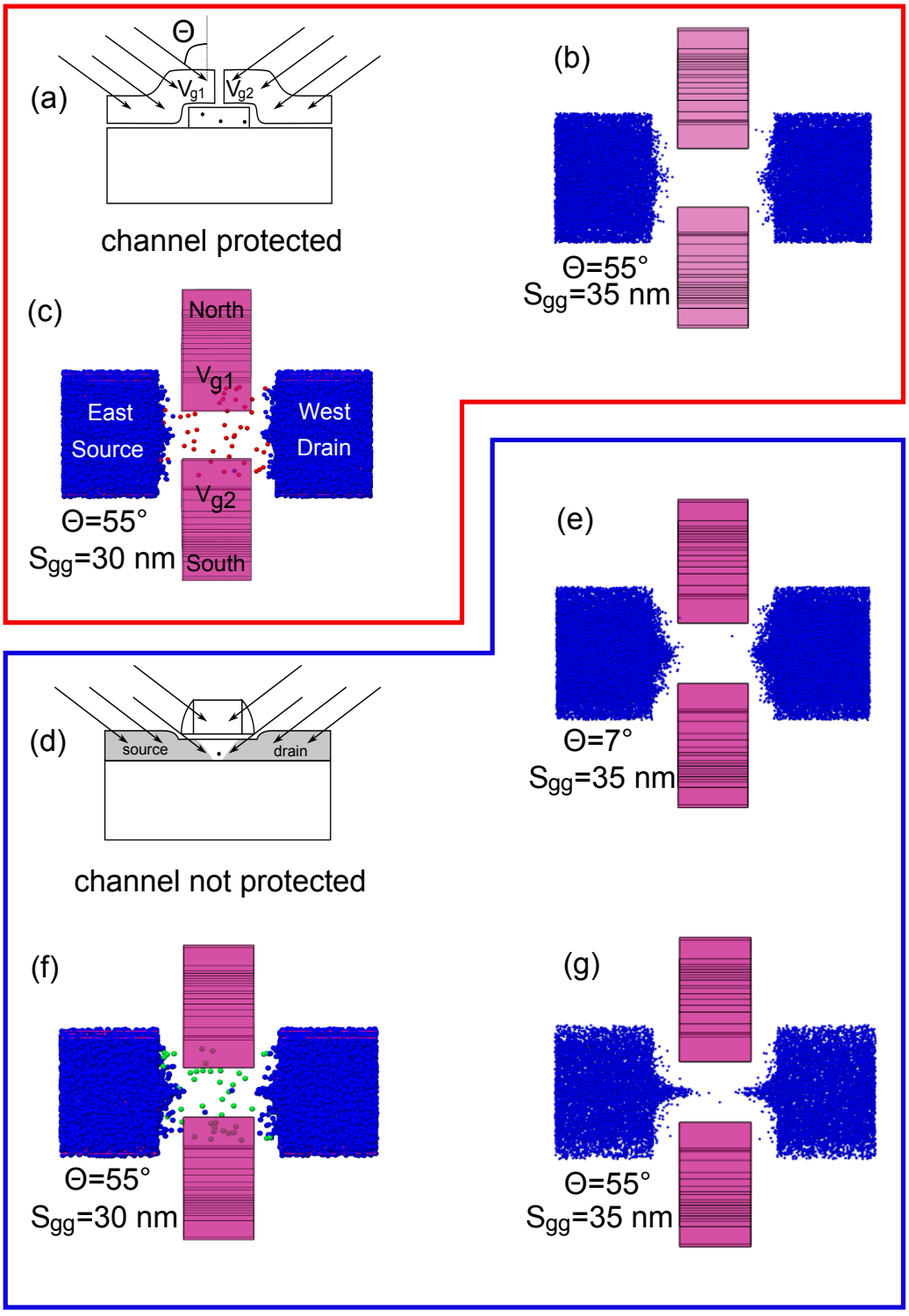

Figure 4.5 *Results of KMC process simualtions. Different geometries with different implantation angles a,d directions. Simulations (b) and (c) correspond to a NS implantation. The gates and the spacers protect the channel in this case. For simulations (e) to (f), the implantation is done along SD: the channel is less protected, which induces a n increased implantation in the middle of the channel between the gates.*

4.2 Coupled-atom transistors (CAT)

In this section we will investigate how we succeeded to create the first coupled-atom transistors in such devices. It represents a development of the article "Detection of a Large Valley-Orbit Splitting in Silicon with Two-Donor Spectroscopy", **PRL** 108, 206812 (2012).

4.2.1 Working point for the CAT

In Chapter 3 we investigated the influence of the very proximity of the SD on dopants ionization. A drawback of this strong coupling is the large screening of the coupling between two donors, as we have seen between donors A and C. Secondly, all the donors in the channel have strong couplings to the leads and can be electrically addressed. Therefore this situation prevents from investigating direct electron exchange between two coupled atoms. This issue can be solved by increasing the effective gate length of the device. To increase this length reduces the tunnel coupling between the donor and the reservoirs: it can become more favourable to tunnel through two donors in series if they are well balanced between SD. Moreover we have seen that the back-gate, although it can induce degeneracies between donors levels, has a strong impact on the reservoirs and then on the coupling between the donors and the front gate. Here we take advantage of having splitted this front gate into two: this will allow to finely tune the energy of the two levels without inducing a strong change of the couplings to the leads.

We now mix all these ingredients and evidence that we can indeed induce resonant tunneling through a pair of donors embedded in series. First we present results on a sample corresponding to the KMC simulation (c). For this sample we don't expect any As donor to have diffused under the channel. However this sample was phosphorous pre-implanted with a concentration of $10^{18}\,\mathrm{cm}^{-3}$. We plot in Fig. 4.6 the SD current as a function of the two front gates (V_{g1}, V_{g2}), at T=100 mK with a finite bias $V_d = 2\,\mathrm{mV}$ and a back-gate voltage ($V_b = 11.5\,\mathrm{V}$. We first describe the top right corner of the figure one can observe a honeycomb structure, typical of a double dot in parallel [115]. These dots are located under the two front gates, forming the 2D Electron gas (2DEG) in the silicon conduction band. We can note that these 2DEGs are created at negative front gate voltages due to the positive back-gate voltage. Now we lower V_{g1} and V_{g2}. We enter the depletion region with no more electron in the 2DEGs[2]. In this region, no current is detected through single donors as a result of the longer gates. Nevertheless we can observe a pair of current spots, called (P1,P2) and circled in black. This current is attributed to resonant transport through two P donors in series as described in the following.

4.2.2 Two atoms in series

[2]For this samples with no optimization of the contacts, we don't detect the first electrons as we were able to do for the samples presented in Chapter 2.

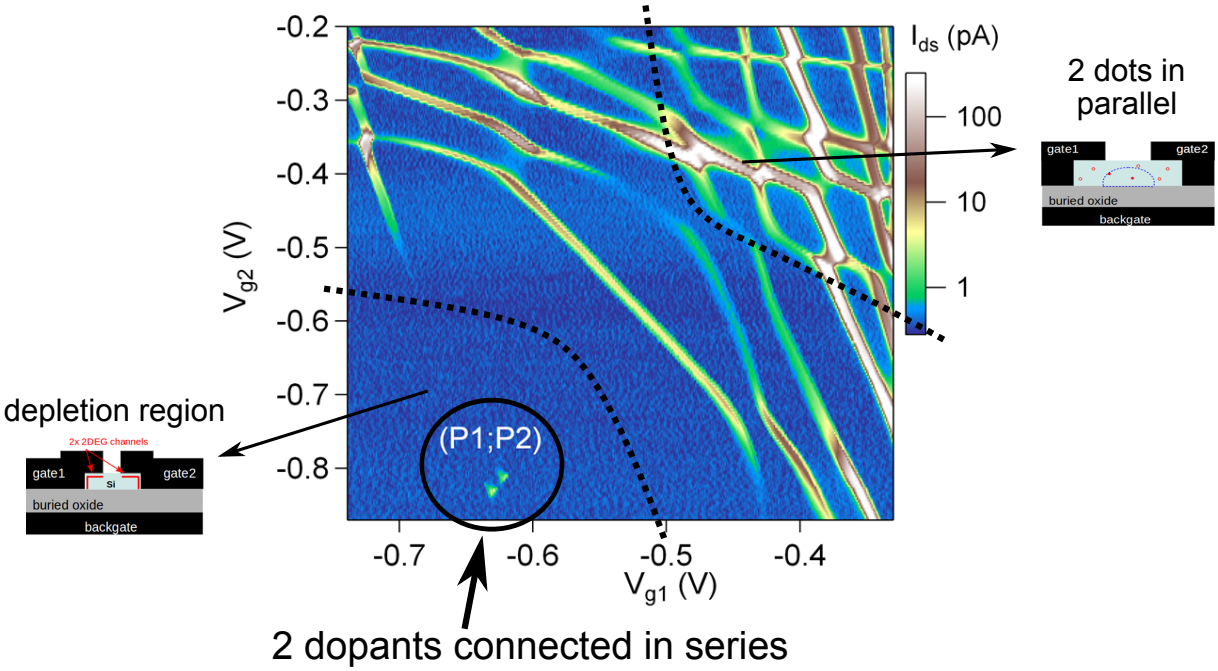

Figure 4.6 *sample #5. Current measured at 100 mK, with* $V_d = 2\,mV$ *and* $V_b = 11.5\,V$*, as a function of* V_{g1} *and* V_{g2}*. On the top right corner of the figure, two dots unedr the two front gates are created. In the bottom left corner, we are in the depletion region and, given the length of the device, current can only occur by resonant tunneling through two atoms embedded in series.*

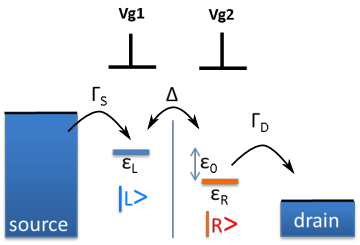

Figure 4.7 *Scheme and conventions used for the CAT.*

Now we focus on this region in Fig.4.8 (a), showing a similar current plot recorded with ($V_d = 3\,mV$. We observe two triangles, whose edges are marked by the black dotted lines. We first describe the lower triangle. The position of this triangle corners correspond to different alignments of the two donors ground levels with the Fermi levels of the SD [115]. This is explained thanks to the different schemes surrounding the figure. The bottom left corner corresponds to a situation where the two levels are aligned with the source. Similarly the bottom right corner (scheme 2) corner corresponds to a situation where the two levels are aligned with the drain. At the last corner, on top left of the figure (scheme 3), the left level is aligned with the source and the right one with the drain. Inside triangle the two levels are in the bias window, but they are separated in energy (energy further called detuning ϵ_0): the current measured in this region is thus inelastic. The tunnel rates Γ_S, Γ_D, Δ and $\Gamma_i n$ have been largely discussed in [93, 91]. We will come back on Δ later. Outside of this triangle, either one of the two levels is outside of the bias window or the two levels are detuned with a negative energy (*e.g.* the left donor is lower in energy that the right donor) and no current is measured.

The relative positions of these corners allow to extract the conversion factors between energy variations and gate voltage variations. Up to now we had only one level and one

front gate. This conversion was done thanks to the level arm factor α. Here we have two levels and two gates, defined according to Fig. 4.7: α becomes a 2×2 matrix called M, with the following definition:

$$\begin{pmatrix} \Delta\epsilon_L \\ \Delta\epsilon_R \end{pmatrix} = \mathbf{M} \cdot \begin{pmatrix} \Delta V_{g1} \\ \Delta V_{g2} \end{pmatrix}. \tag{4.2}$$

In order to determine this matrix M, we take as instance the gate voltages differences between corners 1 and 3, with $\Delta\epsilon_L^{1-2} = 0$ and $\Delta\epsilon_R^{1-2} = eV_d$ and between 2 and 3 with $\Delta\epsilon_L^{2-3} = -eV_d$ and $\Delta\epsilon_L^{2-3} = 0$. As an example we give the matrix M corresponding to this sample in order to illustrate the fact that both gates control both donors:

$$M^{\#6} = -\mathrm{e} \begin{pmatrix} 0.303 & 0.072 \\ 0.147 & 0.151 \end{pmatrix} \tag{4.3}$$

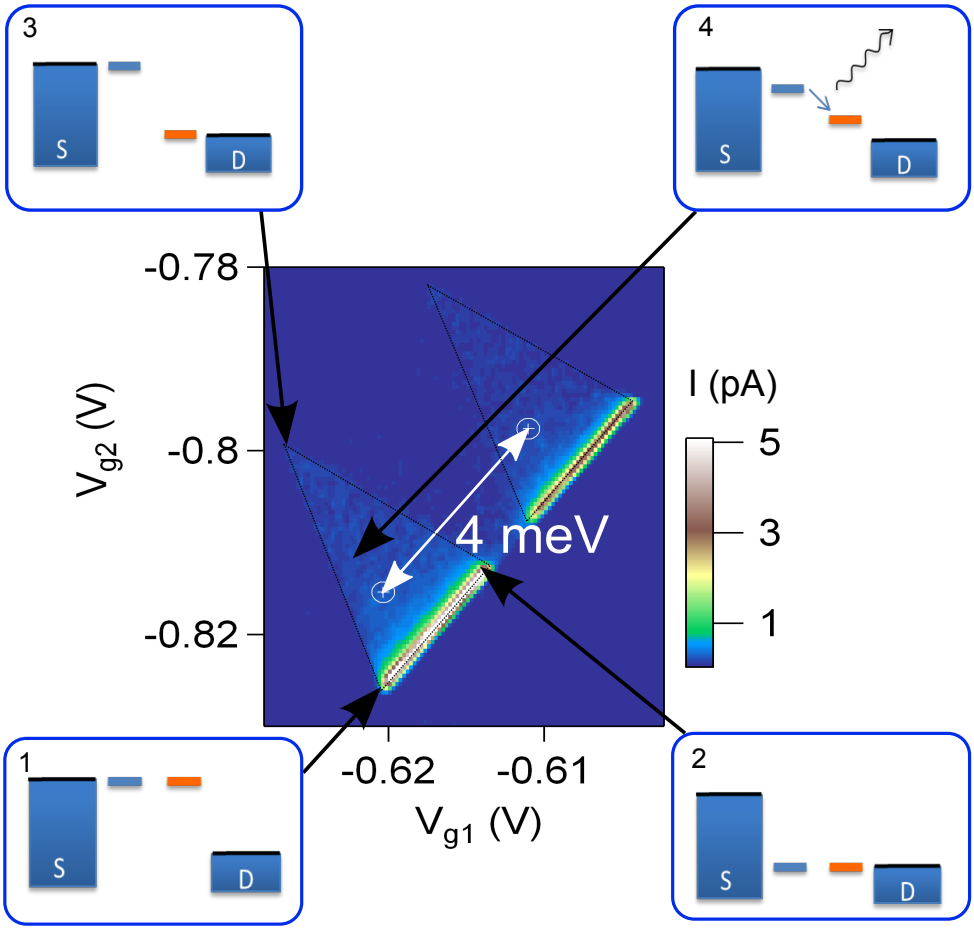

Figure 4.8 *zoom on the circled region of Fig. 4.6. Here* $\mathrm{V_d} = 3\,\mathrm{mV}$. *We observe a pair of triangles, characteristics of transport through two objects (here P atoms) in series. The edges of these diamonds correspond to different alignements of the levels between SD. We can measure the Coulomb repulsion between the two donors.*

We note (m,n) the charge state of the system with m (resp. n)=0 or 1 the number of electron on the left (resp. right) donor. For this lower triangle, there is only one or zero

electron in the system. Therefore we deduce the following charge state sequence for an electron to tunnel between source an drain through the donors:

$$(0,0) \rightarrow (1,0) \rightarrow (0,1) \rightarrow (0,0) \tag{4.4}$$

A second sequence exists where there is 1 or 2 electrons in the system:

$$(1,1) \rightarrow (1,0) \rightarrow (0,1) \rightarrow (1,1) \tag{4.5}$$

The last step of this sequence requires to pay the mutual Coulomb energy between the two donors E_C^m: this energy is the analogous of the one determined in Chapter 2 for the corner states. The current associated with this second sequence corresponds to the upper triangle of Fig. 4.8(b). Thanks to the matrix M, we are able to determine this energy, which yields: $E_C^m = 4\,\text{meV}$[3]. This energy is 3 times larger than for the one obtained for the corner states described in Chapter 2 ($\approx 1.5meV$) or between the dnors A and C from Chapter 3. In the latter, we have attributed this reduced energy to the screening of the Coulomb repulsion between the two dots from the metallic gate. Here, taking the bare Coulomb interaction in silicon, these 4 meV correspond to a distance between the two donors of 30 nm. This is in good agreement with the expected mean distance between two donors, which is around 10-20 nm, according to the concentration of implanted phosphorous atoms. Therefore we conclude that the screening effect isn't as strong in these devices. This seems reasonable as the donors are not stuck to the FOX interface as in the case of the corner states (deduced from a large valley-splitting, see below) and with further away source and drain, compared to the anticrossing experimentally observed in Chapter 3 between donors A and C (moreover also in the interfacial regime).

4.2.3 Valley-orbit splitting

We now increase the bias voltage to 16 mV and measure again the current as a function of (Vg1, Vg2). The result is plotted in Fig. 4.9. First the two triangles have grown, as expected from the matrix M, and now overlap as the bias voltage is larger than the Coulomb repulsion between the donors. Inside the triangles, we observe an additional current line (marked by a red cross), which is parallel to the base line (blue cross). Following the schemes of Fig. 4.9, this line corresponds to the alignment of the left donor ground state with the right donor first excited state. Using the matrix M it is straightforward to determine the energy splitting Δ_1^R between the ground and the first excited states of this donor: we found $\Delta_1^R = 10.3 \pm 0.5\,\text{meV}$. Similarly, we obtained Δ_1^L measured at negative bias: $\Delta_1^L = 9.3 \pm 0.5\,\text{meV}$. We see here the advantage of having a double donor system to perform spectroscopy: the first donor acts as an energy filter and prevents the spectroscopy of the second donor of being masked by the LDOS or by the temperature broadening of the leads as it was the case in ref [80] and in Chapter 3.

[3]This energy also corresponds to the bias voltage start overlapping each other, see Fig. 4.9

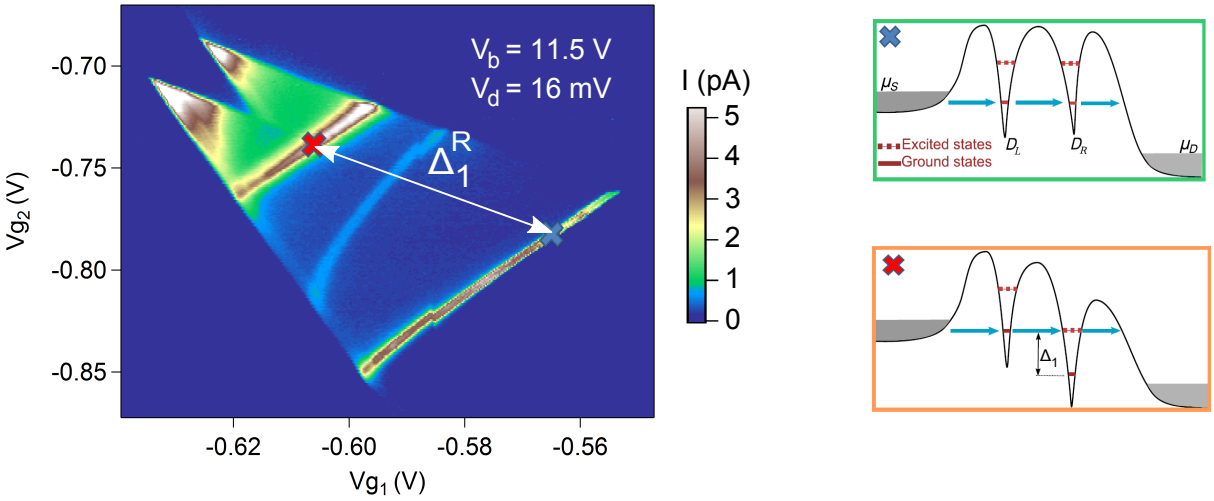

Figure 4.9 *Same than Fig. 4.8 for aa larger bias* $V_d = 16\,mV$. *The line parallel to the base line corresponds to the alignement of the goudn state of the left donor and the first excited state of the right donor. We measured a valley splititng of about 10.3 meV.*

From Chapter 1 we know that the spectrum of a donor is affected by the presence of a mesoscopic environment [87, 86]. In bulk silicon, the steep donor potential induces a lifting of the valley degeneracy and result in a non-degenerate ground state and the first excited state 11.7 meV above it (for phosphorous). Our experimental result of 10 meV is about twice the maximum other valley-orbit splittings (VOS) reported in the literature [101, 58]. Apart from [110], it is also much larger than those observed in silicon quantum dots, as discussed in Chapter 2. This large VOS indicates that the donors are in the Coulomb confined regime with the electron screening the attractive donor potential. According to our results of Chapter 3, the double occupied states of these donors are thus not stabilized and should occur very close to the onset of the conduction band, and should be hardly distinguishable. We did not point our attention to the double occupation issue in this work.

These results are supported by numerical simulations presented in section 1.3.2 performed by Cobian and Niquet. They compute the electronic structure of P impurities i a 20 nm-thick Si film embedded in SiO_2 using a $sp^3d^5s^*$ tight-binding model [71]. We plot in Fig. 4.10 the VOS as a function of the donor distance to the interface, for several electric field. We estimate the electric field to be of the order of 5-10 mV/nm in those samples. We see indeed than a 10 meV VOS corresponds to a donor located at more than 3 nm of the Si/SiO_2 interface. Because of the dielectric, the electronic wave function is shifted away from the donor, thus reducing the central cell correction and the VOS.

We have measured a second sample exhibiting transport through two donors in series. This sample corresponds to the KMC simulation (f) of Fig. 4.5 (with a 12 nm-thick Si film). We plot in Fig. 4.11 two current map recorded at $V_b = -0.5\,V$ and respectively at $V_d = 5\,mV$ (a) and $V_d = 15\,mV$. On (a) we observe the onsets of the 2DEGs created under the front gates, around 120 mV for V_{g1} and 50 mV for V_{g2}. Below these regions we observe spots of current, marked by the white circle. Increasing the bias in the region to

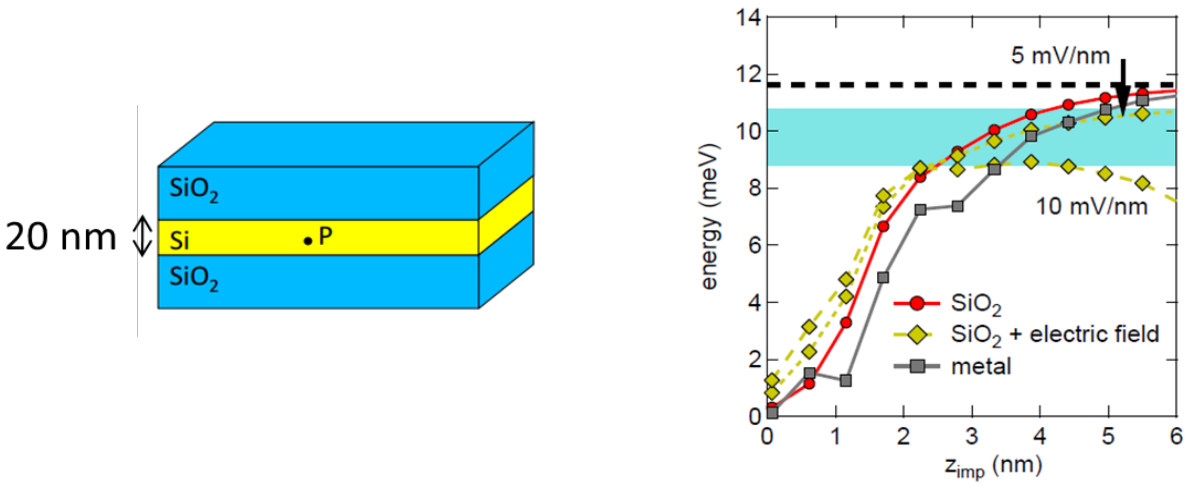

Figure 4.10 *Numerical simulations of the valley-orbit splitting for a P atom in a 20 nm-thick Si film, as a function of the distance to the interface for different electric fields. The measured VOS for this sample correspond to the edge of the blue stripe.*

$V_d = 15\,mV$ leads for these spots to form a pair of triangles as for the previous sample. Here we attribute these triangles to resonant transport through two As atoms embedded in series, which have diffused from the SD during the annealing step. Again the large bias measurement allow to extract the VOS for one of the donor: $\Delta_{\#7} = 7.4 \pm 0.4\,meV$ and a Coulomb repulsion of 4.5 meV between the donors. The second donor's VOS couldn't be measured because of a too weak current.

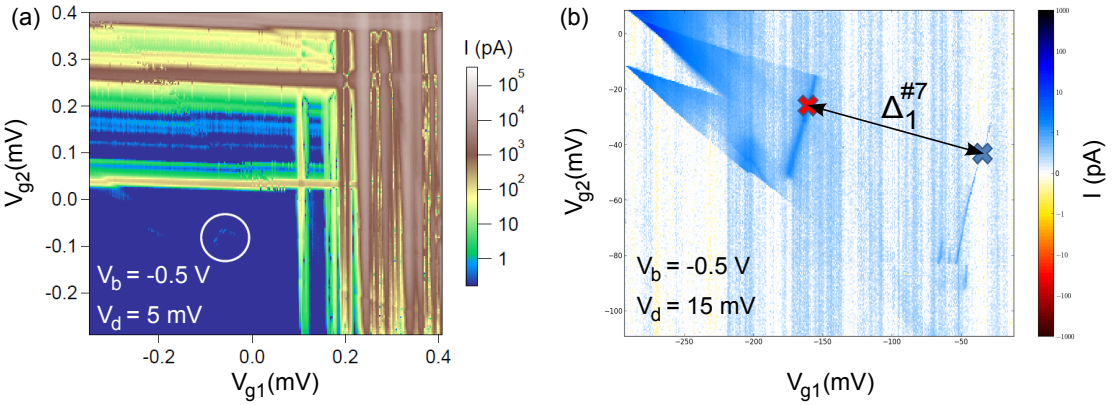

Figure 4.11 *Sample #7. (a) Current at $V_d = 5\,mV$, $V_b = -0.5\,V$ as afunction of (Vg1, Vg2). We observe spots of current below and close the onsets of the 2DEGs. (b) Zoom on the circled region of (a) at $V_d = 15\,mV$ We observe a pair of triangles, attributed to the transport through two As atoms in series. We measured a VOS of 7.4 meV, three times less than the bulk value.*

For an As atom, the VOS is around 21 meV in bulk. Here we measure a reduction by a factor of 3 of this VOS. For this sample we believe that at least this donor could be in the hybridized or interfacial regime which would explain this reduction. We can also note that between the two samples presented in this Chapter were measured in different back-gate and front gates conditions. For the P-doped $V_b = 11.5\,V$, with strong negative V_g. This

pulls the electrons towards the body of the channel and the BOX interface. Whereas for the As-doped sample, we have set $V_b = -0.5\,V$ and V_g close to 0. The electronic wave function of these atoms should be rather located close to the FOX interface.

Conclusion

In this Chapter we have seen that we succeed in coupling two atoms in series, thanks to a fine tuning of the electrostatic potential of the channel with two front gates facing each other. This situation is very interesting as it gives access to a clear spectroscopy of the excited states, and to functionalities as electron pumps, demonstrated by Roche *et al.* [91] (not developed here). For the future, the double occupation problem would have to be seriously investigated in these systems as it opens the way to singlet and triplet physics as the Pauli spin blockade mechanism [56] for instance.

Chapter 5

Spin and charge manipulations in transistors

Contents

Introduction

We have well characterized the spin states of a corner state and the coupled-etom transistor in the previous Chapters. Here we try to manipulate such states with high-frequency signals in order to take a look into their coherence. First we will try to measure the relaxation time of a corner state spin up using a three-step pulse protocol. Secondly, we will induce Landau-Zener transitions between the two levels of a CAT showing that an electron can be coherently transferred between two donors in silicon. These experiments will appeal for the development of charge-sensing techniques for the future.

5.1 Experimental setup

5.1.1 Description

To perform these experiments, we need to send high frequency (HF) signals to the sample. This is achieved using two coaxial lines on a dilution fridge, going from room temperature (RT) to the mixing chamber of the fridge. Attenuators are placed all along these lines, according to the sketch presented on Fig 5.1, to ensure a good thermalisation of the HF signal, to preserve the electronic temperature of the sample when a high frequency signals are applied. They also prevent some unwanted reflections in the lines which could occur.

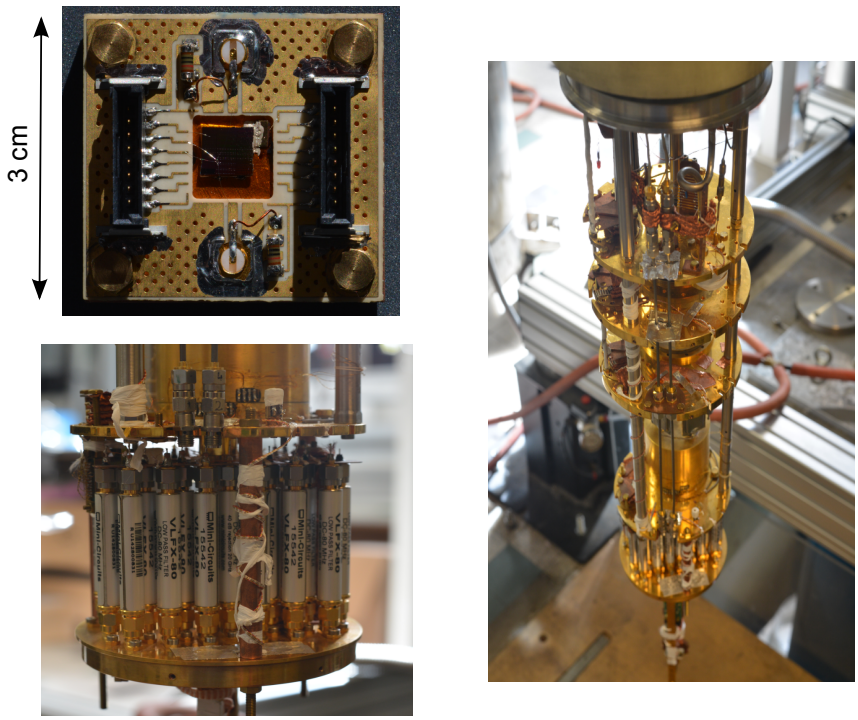

Figure 5.1 *Pictures of the setup used for the high-frequency experiments. (top left) The sample holder with the RF connector (middle top and bottom), the DC connectors (middle left and right) and the resistance used for the bias-tee. (bottom left) The mixing chamber stage with the 80MHz-low pass filters. We also see the ends of the HF lines with a 3 dB attenuator. The thermal anchor is not shown. (right) The whole IVC stages.*

Throughout this chapter, we will apply HF signals on the top gates of the samples. Thus, the HF signal must then be added with the DC voltage used to gate the device. This is done using a bias-tee, which is directly on the sample-holder, which we designed for that purpose. One can see a picture of this sample-holder on Fig 5.1 with one the DC line which is linked to the HF signal, coming from a RF mounting panel connector, through a $10k\Omega$ resistor. A DC block (not represented), with a 50 kHz-bandwidth, is also added on the HF line to prevent a DC voltage drop on the sample, the output of the HF signal generator being, on average, grounded. Finally, both DC and HF signals are sent from the sample holder to the sample gate pad with usual bonding wires. All the DC lines are filtered with 500 Hz low-pass filters at room temperature and 80 MHz low-pass filters at the base temperature.

5.1.2 Room temperature characterisation

We then need to characterize this setup, to check that there is no ringing in the lines, which could be caused by the presence of defects or cavities. We present on Fig. 5.2 two graphs allowing to extract the time and frequency domains characteristic scales. The graph (a) presents the attenuation of each line as a function of the frequency. We observe that the attenuation increases with frequency and that the lines totally cut frequencies above 20 GHz as expected. The graph (b) presents the time response of the lines (back and forth) to a voltage square pulse with the sample holder included. A long bonding wire was soldered between the two sample-holder RF connectors to minimize the loss and the possible reflections and be as close as possible to the actual setup. We then were able to extract the raise time of the lines and found it to be equal to 340 ps.

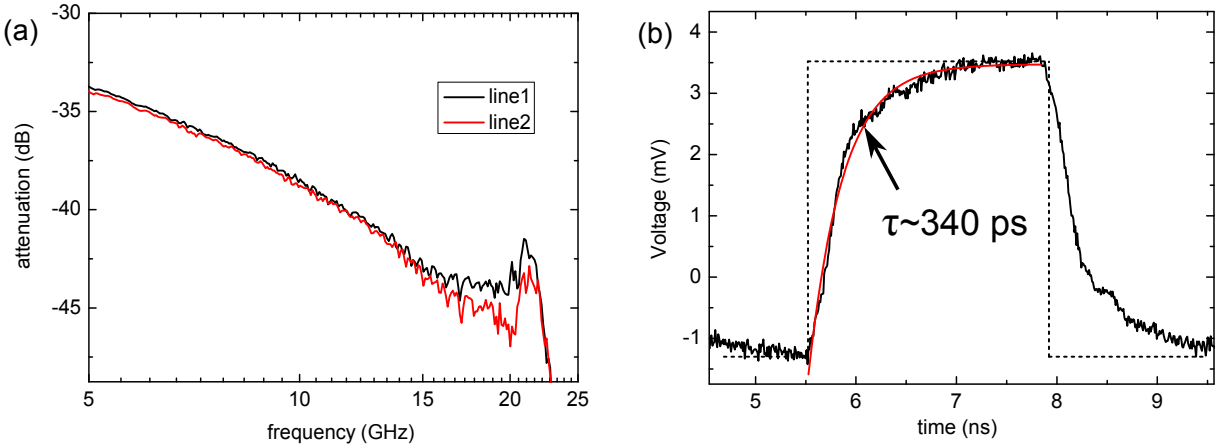

Figure 5.2 *(a) Attenuation of each high-frequency line as a function of the frequency. (b) Raise time of the line measured to 340 ps.*

5.2 Spin manipulations on a corner state

5.2.1 Setup for T1

We consider again the sample #2 measured in Chapter 2. We evidenced at negative V_b a spin filling of the first electrons and a singlet as the two-electron ground state. We cooled down again this device in this fridge equiped with HF lines. It has to be noted that the sample slightly changed during the thermal cycle but we were still able to recover the main features: a degenerate ground state which is Zeeman splitted under a magnetic field and a first excited state above 1 meV and which will be neglected throughout this chapter. All the results presented in this subsection were performed at $V_b = -10V$ on the first electron of the second corner state, which appeared to be much less noisy (probably charge noise) after a second cool down than the first one. A fit of the peak conductance resulted in an electronic temperature of 100 mK. It is impossible to flow a current only through the spin excited state (called spin up) when the spin degeneracy is lifted by a magnetic field) if one performs usual d.c. experiments, but only through the spin ground state (spin down) or spins up and down, when these two levels are in the bias window (see for instance Fig.**??** for a positive bias). In order to further characterize this spin up, we thus have to implement a dynamical setup. We performed d.c. measurements based on a repeated pulse protocol, following the work of Hanson *et al.* [37].

We used a typical three-step pulse for this experiment, whose protocol is described on Fig. 5.3.

We apply a small bias V_d, here negative and vary the gate voltage according to (c) and (d). First, on step E, we empty the dot putting any electron up or down into the drain, which is supposed to have a larger tunnel rate than the source ($\Gamma_D >> \Gamma_S$). Then we bring the two levels below the Fermi level: an electron is loaded either in state up or down. We wait at this stage a certain amount of time (W) before bringing the up state into the bias window. This is the read-out step (R). Here different situations can occur:

- An electron down was loaded during (W). Then no current will flow at (R) as the elctron remains below the Fermi level.
- An electron up was loaded during (W) but as relaxed to down during (W). No SD current will be detected during (R) as well.
- An electron up was loaded during (W) and remained in this excited state. It is thus the only situation where a current will occur during step (R), the dot being unloaded into the source.

We can identify on Fig. 5.3(c) the gate voltage positions for these three steps, represented by the different crosses. We repeat this sequence infinitely and measure the average current per cycle with a classical multimeter.

We see that requirements should be fulfil for this protocol:

- First one needs an asymmetry in the tunnel rates as high as possible. Indeed, the only DC current that we want to flow between SD is the current associated with the spin up. The only process which involves the source side must be the tunneling event of the up state to the source. Every other tunnel process must involve the

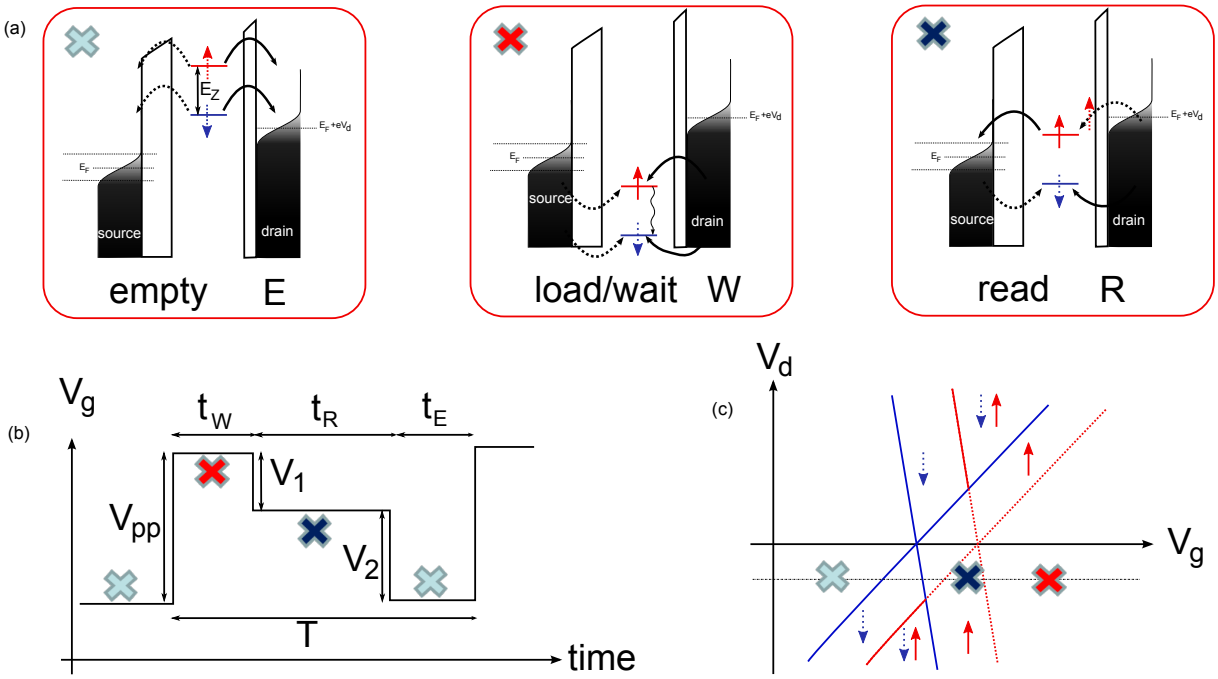

Figure 5.3 *Description of the three-step pulse. (a) Configurations of the dot during the three steps: empty (E), load and wait (W) and read (R). (b) Time evolution of the gate voltage during the pulse. (c) Positions of the levels for the three steps. The red dotted lines indicate that the diamond due to the spin up state doesn't exist in d.c. measurements because of the Coulomb blockade.*

drain, especially the unwanted loadings to the down state. In that case we can neglect the processes depicted by the dotted arrows of Fig. 5.3, which could result in a parasitic current. In 2DEG heterostructures, these tunnel rates can be easily controlled thanks to the different gates. In our system this not the case even if asymmetries can occur as we have seen in the section 2.1.3. Here for this back-gate voltage, we found that the best situation was to work at negative polarity. For sure the asymmetry in the tunnel rates was not optimized during these experiments. Nevertheless we will evidence the transport through the up state.

– Secondly, the Zeeman splitting has to be larger than the thermal broadening of the reservoirs. We evaluated this broadening to be $40\,\mu$eV for this resonance, meaning that we need to work at magnetic fields higher than around 0.5 T. Again this will prevent a current through the down state to flow during the read-out. For the same reason, the bias voltage should be less than the Zeeman energy., we will therefore work with $V_d = -50\,\mu V$.
– There are requirements on the step amplitudes. First the energy difference between steps (R) and (E) has to be larger than the Zeeman energy, in order for the spin down to be sent back to the drain: $|e|V_2 > E_Z$. Secondly, one needs $|e|V_1 > |V_d|$ for the two levels to be effectively under the Fermi levels during step (W).

Assuming that these requirements are fulfilled, we can easily calculate the DC current which will flow between SD. We call T_1 the phenomenological relaxation time of the

electron up to the ground state. Therefore the probability to still be in the spin up state at a time t after its loading is simply given by:

$$p_{\uparrow}(t) = exp(-t/T_1) \tag{5.1}$$

Secondly we consider that all the other processes which result in parasitic SD current (for instance due to non perfect asymmetry) are independent of this relaxation process and thus to the time spent during (W). Moreover, we could draw a list of these parasitic processes and see that their sum actually should lead to zero current. We give here only one example of two processes which cancel each other: an electron down can be loaded during (W) from the source with probability $p_1\Gamma_S/(\Gamma_S+\Gamma_D)$ and released to the drain during (E) with probability $p'_1 = \Gamma_D/(\Gamma_S+\Gamma_D)$. This gives raise the SD current $I_1 = |e|p_1p'_1f$ where f=1/T is the repetition frequency. On an other hand, an electron down can be loaded during (W) from the drain with probability $p_2 = \Gamma_D/(\Gamma_S+\Gamma_D)$ and released to the drain during (E) with probability $p'_2\Gamma_S/(\Gamma_S+\Gamma_D)$, and results in the SD current $I_2 = -|e|p_2p'_2f$. It is straightforward that $I_1 + I_2 = 0$. Processes involving the same reservoir for the loading and the unloading events naturally give no SD current. Nevertheless, it is still comfortable to work with asymmetric barriers, as the tunnel rates may also evolve as a function of the different gate voltages, which hasn't been taken into account here.

Finally we conclude with this simple model that the evolution of the current only depends on the relaxation of the up state and then on the waiting time t_W. We will record the current as a function of this waiting time, keeping the repetition frequency constant: one should obtain an exponential decrease of the current due to the relaxation of the up state:

$$\boxed{I(t_W) = I(t_W = 0)exp(-t_W/T_1)} \tag{5.2}$$

This last equation can be translated into an average number of up electron per cycle flowing between SD: $< n_{\uparrow}(t_W) >= I(t_W)/(ef)$ and hence:

$$\boxed{< n_{\uparrow}(t_W) >=< n_{\uparrow}(t_W = 0) > exp(-t_W/T_1)} \tag{5.3}$$

5.2.2 Experimental results

Working point of the measure

We now turn to the experimental results. First one has to find the working point for the gate voltages and the different pulse amplitudes to correspond to the situation described on Fig. 5.3 (c). It has to be noted that we apply the DC and the AC voltages to both sides of the gate, in order to avoid any current to flow through the gate, which would results in heating effects (the gate typical resistance is around 100 Ω).

We start working with a magnetic field of 1.5 T and a clock frequency of 7.81 MHz (T=128 ns). We have tuned the pulse amplitudes in the following way: $V_{pp} = 530\,\mu V$, separated into $V_1 = 150\,\mu V$ and $V_{pp} = 380\,\mu V$, thus satisfying the criteria found in the

previous section, and $t_w = 88\,ns$, $t_E = t_R = 20ns$. Fig. 5.4(a) shows a diamond of the resonance taken at B = 1.5 T, without pulse. Then we turn on the three-step pulse and record the current along the black dotted line of (a) at $V_d = -50\mu V$. This is shown on (b): We observe four peaks in the current which can be explained following the schemes of the array (d): the peaks 1,2,4 respectively correspond to the alignment of the down state with the bias window for the three different steps (resp. W, R and E). The amount of current is then linear with the amount of time spent at these steps, as no Coulomb blockade can occur. We can also check that the gate voltage differences between these peaks are in agreement with the amplitudes of the pulses: as instance we recover the $180\,\mu V$ between 1 and 2. We now focus on the third peak: we attribute it to the current through the up state as described in Fig 5.3. This is confirmed by a magnetic field dependence of this peak presented on (c): the voltage difference with the peak 2 (spin down in the bias window at the same step R) increases linearly with the magnetic field, evidencing once again the Zeeman splitting of the level (black dotted lines).

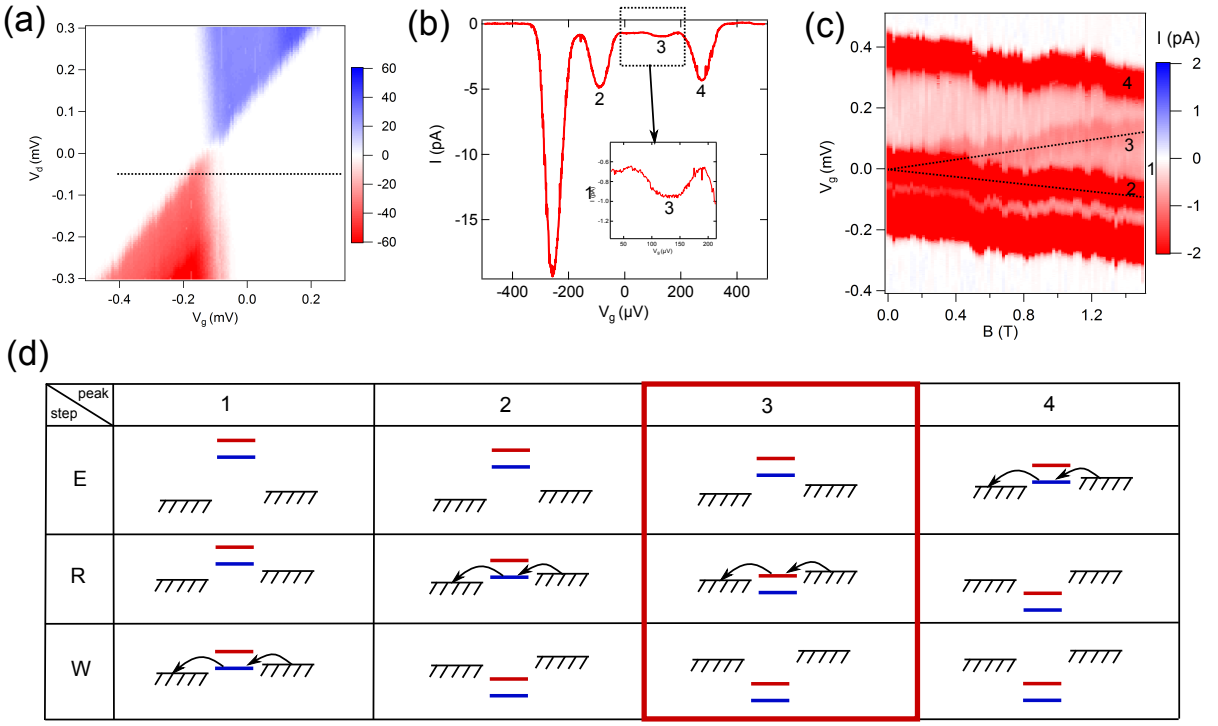

Figure 5.4 *(a) diamond (in d.c. current) carried out at B=1.5 T, without pulse. (b)current trace at* $V_d = -50\mu V$ *,along the black dotted line of (a), with pulse. The peak 3 (inset) corresponds to the current int he up state, as described in Fig. 5.3. (c) Current vs. magnetic field and gate voltage. The peak 2 and 3 are separated by the Zeeman energy as expected. (d) Sum-up for each peak (1 to 4) of the dot configuration, at each step of the pulse.*

We can also observe that the level of current does not decrease to zero between the peaks, for instance between peaks 2 and 3, whereas this should be the case according to the model developed above. We checked that this parasitic current was linear with the clock frequency and then attribute this current to pumping through the device. A possible explanation would be that the tunnel rates evolve asymmetrically with the gate voltage.

We now carry out a t_W dependence of this current associated with the spin up. We recorded the DC current for different waiting times, while keeping the clock frequency constant. Therefore we also need to change the other step size: we have chosen to keep a constant read-out step time and to change the unloading step accordingly to the waiting step. We compile in table 5.1 the parameters of these sequences.

sequence	clock frequency frequency (MHz)	magnetic field (T)	V_1 (μeV)	V_2 (μeV)
1	7.81	1.5	280	370
2	7.81	4	310	1010
3	7.81	8	310	1710
4	1.95	4	300	1050

Table 5.1 *Different sequences, where the waiting time changes, measured*

On Fig. 5.5 we show the results obtained with these sequences. On (a) we present a 2D map of the current plot as a function of V_g and of t_W. Taking a line cut for a fixed t_W, we recover the four peaks that we discussed previously. The overall shift towards positive gate voltage when t_W increases is simply due to the DC block which filters the DC component of the pulse (*i.e.* its average amplitude), which changes with t_W, before adding it to the DC gate voltage. The inset of (a) represents a cut taken at $t_W = 34$. In order to extract the current in the up state, we have fitted the peak 3 using a Gaussian function. We have also taken into account the parasitic current by superimposing a linear background to this Gaussian profile. We are then able to calculate the mean number of electrons up flowing per cycle between SD thanks to the relation: $< n_\uparrow >= I_\uparrow/(ef)$ where $I_\uparrow$ is the maximum of the fitted Gaussian function. This background was fluctuating from trace to trace and had to be adjusted in consequence. The final results concerning $< n_\uparrow >$ are plotted on Fig (b).

One can observe a general decrease of $< n_\uparrow >$ when one increases the magnetic field: around 0.30 at B=1.5 T (blue spheres), it drops to about 0.08 at B=8 T (black spheres). One possible mechanism accounting for this fact is a spin-dependent change of the tunnel rates with the magnetic field: at higher magnetic field, it would become more favorable to load the electron in the down state, because of a spin polarization of the reservoir. Then less electron are loaded in the up state during (W), resulting in less current observed during (R).

Secondly, for all the sequences, we don't see a decrease in $< n_\uparrow >$ within the t_W-range investigated. The only conclusion we reasonably draw from those measurement is that the relaxation time T_1 should be higher than 1μs at 4 T. This is illustrated on Fig. 5.5 (b) with the light blue solid curve, which represent the expectation for a $T_1 = 1\,\mu$s and with a initial $< n_\uparrow > (T_W = 0) = 0.18$. This line rapidly lies under the experimental points of the sequence 4, taking into account the variance of the maximal current fits. Here we

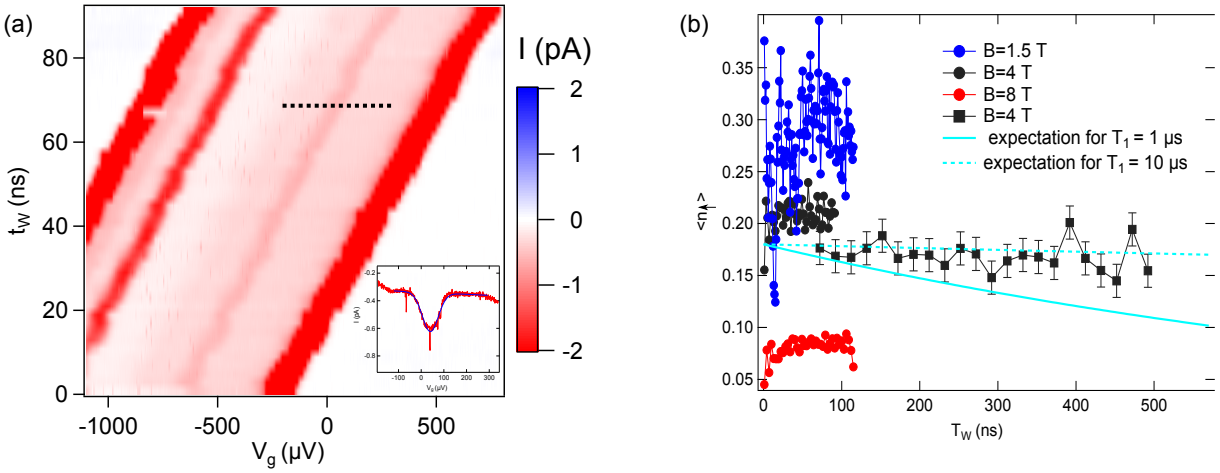

Figure 5.5 *(a) Current recorded as a function of* V_g *and the waiting time* t_W*. The clock frequency was set to 7.825 MHz and magnetci field to 1.5 T. Inset: current along the black dotted line showing an example of the Gaussian fit of the current. (b) average number of electrons in the up states as a function of* t_W*, for several magnetic fields. No accurate relaxation time could be measured because of the limited band width of the setup.*

naturally come to the experimental bandwidth limitation of the setup. The measurement is based on the direct record of the DC current, which has a resolution of about 20 fA averaging the DC current to 100 PLCs (*i.e.* current averaged over 2 s), due to an oscillating shift in the amplifier offset. It means that the peak can't be detected below this limit. This value correspond to a clock frequency of 1.25 MHz, assuming that we would need at least to detect $< n_\uparrow >$ of the order of 0.1 to be able to fit the relaxation. This means that we can't investigate much longer waiting time than the one presented on Fig.5.5 (c) to precisely measure the relaxation time of a corner state electron spin.

For the future, considering the very low level of current associated with very long relaxation times, one would need to implement charge sensing techniques, which are now widely used for spin state detection and manipulation. For instance, Morello *et al.* use a SET to probe the spin state of an isolated donor through a spin-to-charge conversion [65] and Simmons *et al.* used a Quantum Point Contact for the detector [105]. The developments of RF-SET, where the channel is embedded in a tank circuit [99], represents a great interest thanks to an increase measurement bandwidth over 10 MHz.

5.3 Landau-Zener interferences on the Coupled Atom Transistor

We have seen that investigate the spin coherence remains too challenging without improvements on the setup. Still, an other type of coherence can be studied in our system, which is the phase coherence of an electron. More precisely we studied the phase coherence of an electron shared between two quantum levels, spatially separated. The system we used is the coupled atom device presented on chapter 4, with the two donors coupled in series between source and drain. This system can be seen as a charge qubit, where

the two quantum states are the ground states of each dopant, with a tunnel coupling Δ between them. Hollenberg *et al.* [44] proposed to perform quantum computing with such charge qubits. Compared to spin qubits, where the information is encoded either in the electron [118, 82] or the nuclear spin [47, 83, 66], they have the advantage to be electrically addressable (no need for fast oscillating magnetic field) but, as the counterpart of it, they are more sensitive to charge and gate noise which result in shorter quantum coherence times. But even in the latter the coupling between different electrons is crucial, being the media to control entanglement. This section is a development from the article "Coherent Coupling of Two Dopants in a Silicon Nanowire Probed by Landau-Zener-Stückelberg Interferometry", Physical Review Letters **110**, 136802 (2013).

5.3.1 Principle of the experiment

We need to transfer an electron between two quantum states: the two-dopant system studied in the previous chapter is a toy-model for this. We cooled down an other As-doped sample with two gates facing each other. Tuning the back-gate, we again obtain on Fig ?? the characteristic triangles in the (V_{g1}, V_{g2}) current map. For this sample, the first excited state has been measured at 7.4 meV (see chapter 3), which still represents a huge energy window: one could perform operation up to 1 THz without exciting this state[1].

In general systems, one way to investigate the phase coherence is to induce interferences as the contrast of the fringes strongly depends on this coherence. In the following experiment we will perform an analogous to the Mach-Zehnder interferometer, which is the most basic interference experiment in optics.

We divide the principle of the experiment into three steps:

- First, an electron is loaded on the left dopant with the rate Γ_S.
- Secondly we will sweep the two levels with respect to each other
- Finally the probability for the electron to be on the right donor is read through the drain with the tunnel rate Γ_D.

It is important to note that this mechanism is not discretized as one could think, because the two levels will always be kept into the bias window. The levels are then continuously read and loaded.

5.3.2 Experimental results

Increasing the driving frequency

The sample used for these experiments is sample #7 presented on Chapter 4. We apply a $V_d = 5$mV and fix the DC gate voltages to the point in the middle of the base line of the first triangle.

[1] this is far beyond the scope of this thesis as it would deserve a complete modified and improved experimental setup to reach this frequency range.

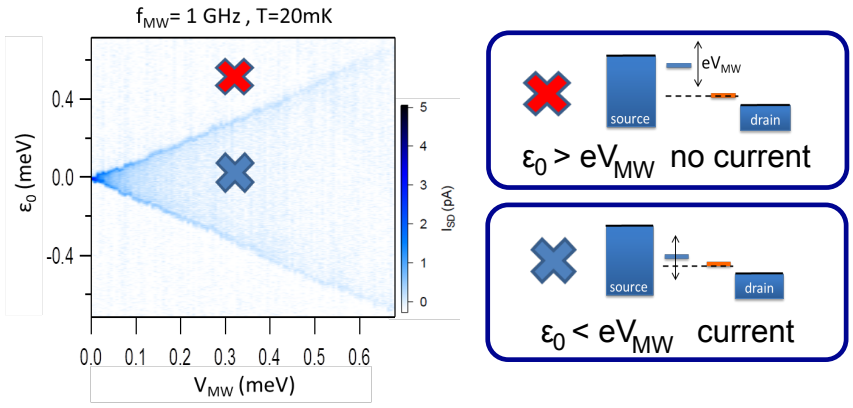

Figure 5.6 *Sample #7. Current vs. detuning and* V_{MW} *carried out at 1 GHz. Outside of the triangular region (red cross), the two levels don't cross and no current is measured. Inside the triangle, the two levels cross during the sweep which results in d.c. current.*

We first start with a slow frequency where we expect the system to be in an adiabatic regime: the electron always remain in the ground state, defined by the level which has the lowest energy. We plot in Fig. 5.6 the SD current in 2D map, as a function of the detuning (moving one front gate, converted in energy with the α parameter) and of the amplitude of the driving signal. At V_{MW}=0, we only have current on the base line, when the two levels are aligned. Increasing V_{MW}, we obtain a triangular shape for the current. In a region located outside of this triangle, for instance on the red cross, we have the condition $\epsilon_0 > |e|V_{MW}$. Hence the two levels are never aligned and no SD current flows. On the contrary inside the triangle (blue cross), the levels are aligned during the sweep and current can flow. The coherence is lost between successive crossings.

Now we increase the frequency. We plot the same maps in Fig. 5.7 at three different frequencies: 1 GHz, 3 GHz and 20 GHz from left to right. We see the that instead of a blurred and smooth current inside the triangular region, we can identify a structure which appears at 3 GHz and which becomes a real interference pattern at 20 GHz. We attribute this remarkable change in the SD current to the coherence which is preserved at such frequency between successive crossings.

Now we focus on this last measurement and will explain the main characteristics of this interference pattern.

5.3.3 Interferences from successive Landau-Zener transitions

We focus on the second step of the experiment, whose the aim is to built the interferences, using Fig. 5.8. We start with an electron on the left donor, supposed at lower energy than the right one. Hence the electron is in the ground state of the two-level system. Then, applying a pulse to the gate voltage, we move the two levels with respect to each other and when they cross, there is a probability for the electron either to tunnel from the left to the right donor, following the ground state of the two levels, or to remain and the left donor which becomes the excited state. This is known as the Landau-Zener transition [16], as depicted on Fig.5.8. After the crossing , the two levels R an L represent two paths

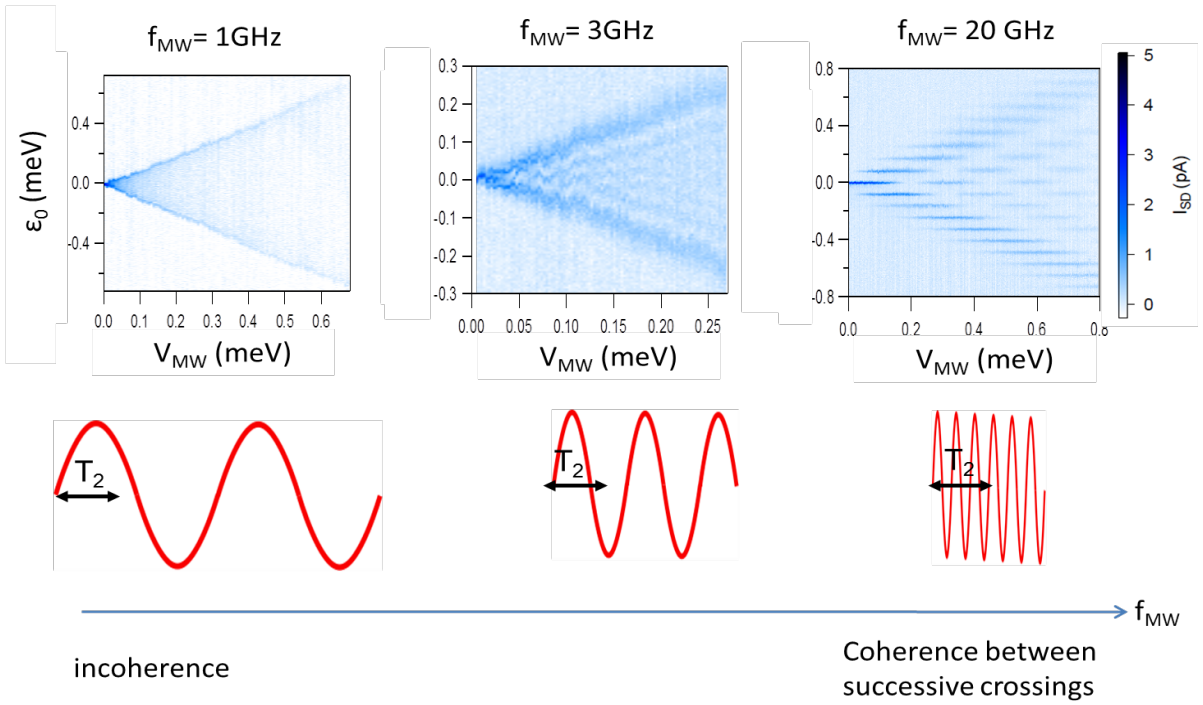

Figure 5.7 *Same measurements than Fig. 5.6 for increasing frequencie. At 20 GHz, a clear interference pattern appears, sign of coherent successive crossings.*

that the electron can go in, with a certain probability.

$$P_{LZ} = \exp(-\frac{\pi}{2}\frac{\Delta^2}{\hbar v}) \tag{5.4}$$

where v is the energy speed at the crossing point: $v = \frac{d\epsilon}{dt}$ and Δ is the tunnel coupling between the levels ($\Delta = \min|E_R - E_L|$). This transition doesn't affect the coherence of the electron but induces a spontaneous mechanical phase shift called the Stoke phase. In the following we will consider fast transition ($\Delta^2 \ll \hbar v$) and can neglect this Stoke phase. This Landau-Zener probability also assumes as initial and final conditions that the energy difference between the two levels is swept from $-\infty$ to $+\infty$.

Now we consider an oscillatory gate voltage sweep: after a Landau-Zener transition at a time t1, we assume that the electron remains coherent and that the evolution of its mechanical phase is adiabatic and hence follows:

$$\Delta\theta_i = \frac{1}{\hbar}\int_{t_1}^{t} \epsilon_i(t')dt' \tag{5.5}$$

where i=1 or 2 according to the considered level. Then comes a time t2 where the two levels cross again, resulting in an other Landau-Zener transition. This give raise to quantum interferences. If a more careful study of the DC current will be done in the next section, including decoherence processes, we describe here how these interferences are built.

In order to have constructive interferences, the phase difference between the two paths (i.e. left and right donor) has to be a even multiple of π between successive crossings. The

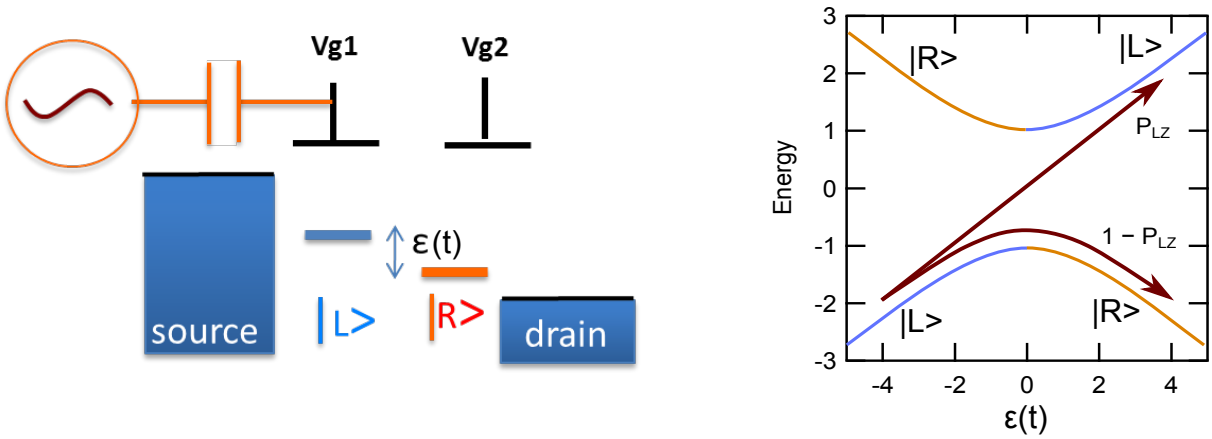

Figure 5.8 *(leftLnadau-Zener transition. (left) An oscillating signal is applied on one gate, resulting in crossings between the two levels. (right) Assuming the electron on the left donor, when the two level cross, the electron has the probability* P_{LZ} *to remain on the left donor and 1-*P_{LZ} *to tunnel to the right donor.*

energy difference is given by $\epsilon(t) = \epsilon_R(t) - \epsilon_L(t) \approx \epsilon_0 + eV_{MW}cos(\omega t)$. We follow the Fig. 5.9 which describes the evolution of the two levels during one period of the sweep. We consider that the first crossing occurs at $t = t_1$, the second at $t = t_2$ and finally a third crossing at $t = t_1 + T$, where T is the period of the oscillating signal. We respectively call $\Delta\theta_1$ ($\Delta\theta_1$ the phase difference between t_1 and t_2 (resp. t_2 and $t_1 + T$). Thus we find two conditions in order to build constructive interferences:

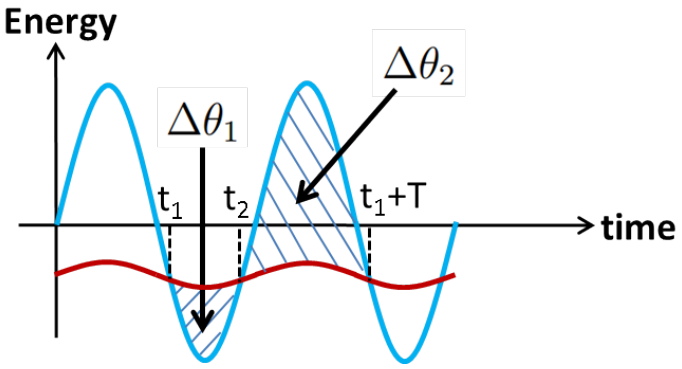

Figure 5.9 *Time evolution of the two levels (blue and red curves). Between two successive crossings, the mechanical phase differences* $\Delta\theta_1$ *and* $\Delta\theta_1$ *have to be multiples of* 2π *in order to build constructive interferences.*

$$\begin{cases} \Delta\theta_1 = 2\pi n = \frac{1}{\hbar}\int_{t_1}^{t_2}[\epsilon_0 + |e|V_{MW}cos(\omega t')]dt' \\ \Delta\theta_2 = 2\pi m = \frac{1}{\hbar}\int_{t_2}^{t_1+T}[\epsilon_0 + |e|V_{MW}cos(\omega t')]dt' \end{cases} \quad (n,m) \in \mathbb{Z} \tag{5.6}$$

These two equations are not easy to understand yet, as the time t_2 is defined only through an integral equation. Nevertheless this system is equivalent to the following one where we have replaced one equation by the sum of the two: we obtain that the total phase difference also has to be an even multiply of 2π.

$$\begin{cases} \Delta\theta_1 = 2\pi n = \frac{1}{\hbar}\int_{t_1}^{t_2}[\epsilon_0 + |e|V_{MW}cos(\omega t')]dt' \\ \Delta\theta_T = \Delta\theta_1 + \Delta\theta_2 = 2\pi(m+n) \end{cases} \quad (n,m) \in \mathbb{Z} \tag{5.7}$$

It is straightforward to calculate $\Delta\theta_T$ as the integral over the oscillating part vanishes. We then obtain a very simple condition to fulfil, which is that the initial detuning (without RF signal) has to be a multiple of the photon energy $\hbar\omega$:

$$\boxed{\epsilon_0 = k\hbar\omega\ ,\ k \in \mathbb{Z}} \tag{5.8}$$

Now we can come back to the measurement carried out at 20 GHz in Fig 5.10. First we identify horizontal ridges, equally spaced as a function of the detuning energy ϵ_0. The energy spacing between successive ridges is in total agreement with the photon energy $\hbar\omega$. Indeed the conversion factor from gate voltage to detuning energy was extracted from the triangles formed by the donors in the (V_{g1}, V_{g2}) plane at large bias voltage and is therefore not an adjustable parameter here. It is even striking that these two alpha parameters (α_{DC} with triangles at large bias and α_{AC} that we could deduce here) exactly correspond within 2%. We have recorded the position in energy of these horizontal ridges (for three different frequencies (10, 15 and 20 GHz)) and plot them in Fig.(b). We observe that the position of a ridge increases linearly with the frequency as expected. This modulation of the current as a function of the detuning energy is called Photon-Assisted Tunneling [114, 76]. It refers to the fact that the tunnelling event of an electron between the two donors is enhanced when the detuning energy equals a multiple of the photon energy.

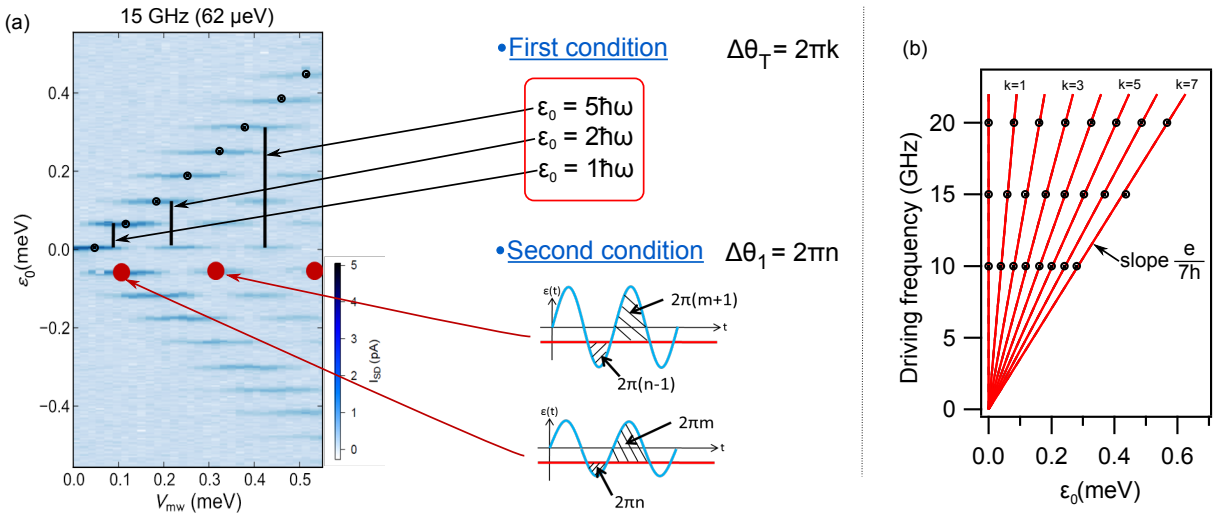

Figure 5.10 *Interferences explained by Landau-Zener-Stückelberg interferometry. (a) The current is modulated along the detuning axis following the photon energy, corresponding t the first resonance condition. Along the amplitude axis the second resonance condition also leads to current modulation. Overall we obtain these interference fringes. (b) Position of the 7 first current maxima as a function of the detuning and the driving frequency. We obtain a linear relation characteristic of a Photon-Assisted Tunneling process.*

Secondly one also observes an horizontal modulation of the current when increasing the driving signal amplitude at fixed detuning. This can be understood thanks to the second

requirement, which is that not only the total phase difference but also both the phase differences between successive crossings should be multiples of 2π. When we increase the driving amplitude, the total phase difference over one period $\Delta\theta_T$ remains constant but $\Delta\theta_1$ and$\Delta\theta_2$ are modified. If we start from a situation with $\Delta\theta_1 = 2\pi n < 0$ and $\Delta\theta_1 = 2\pi m > 0$ (red point on the left), one will have to increase the amplitude up to the point where $\Delta\theta_1 = 2\pi(n-1)$ and $\Delta\theta_2 = 2\pi(m+1)$ to recover constructive interferences and a maximum of current (red point on the right).

5.3.4 Derivation and fit of the current

We have qualitatively well explained the interference pattern which we measured for frequencies allowing to preserve the coherence between successive crossings of the two donor levels. Now we will describe the model used to calculate this current in order to extract the different parameters of our system.

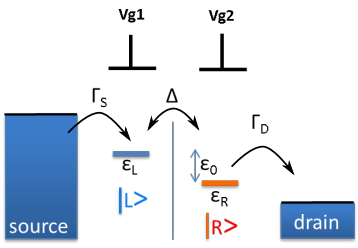

Figure 5.11 *Scheme and notation used for the CAT.*

We consider the same system as in Stoof and Nazarov[109] (see Fig. 5.11):

- Two discrete states $|L\rangle$ and $|R\rangle$
- $|L\rangle$ is connected to a left lead via Γ_S
- $|R\rangle$ is connected to a right lead via Γ_D
- The system is biased such that electrons can only enter the Two-Llevel System (TLS) from the left lead and only leave it into the right lead.
- The system is biased such that only 0 or 1 electron can be in the sytem.

We use the basis $|L\rangle$ (electron in the left level), $|R\rangle$ (electron in the right level), $|0\rangle$ (both levels empty) to describe the system.

We start from an ususal Hamilonian for an isolated TLS and note $\epsilon(t) = \epsilon_R(t) - \epsilon_L(t)$, assuming a real tunnel amplitude:

$$H = \begin{pmatrix} \epsilon(t)/2 & \Delta/2 \\ \Delta/2 & -\epsilon(t)/2 \end{pmatrix} \tag{5.9}$$

In our system, this TLS is continuously connected to the leads, with tunnel rates Γ_S and Γ_D. We then use the formalism of the density matrix to account for this phenomenological terms. The master equation for the 3×3 density matrix ρ_3 is:

$$\dot{\rho_3} = -\frac{i}{\hbar}[H, \rho_3] + \mathcal{D}\rho_3 + \Gamma_S\mathcal{L}(|L\rangle\langle 0|)\rho_3 + \Gamma_D\mathcal{L}(|0\rangle\langle R|)\rho_3, \tag{5.10}$$

$\mathcal{D}$ is a superoperator describing intrinsic decoherence of the TLS. Energy relaxation is dominated by the coupling to the leads (see below), therefore we consider only dephasing, i.e.

$$\mathcal{D} = \frac{1}{2T_\phi}\mathcal{L}(|R\rangle\langle R| - |L\rangle\langle L|). \tag{5.11}$$

$\mathcal{L}(X)$ are the Lindblad superoperators with

$$\mathcal{L}(X)\rho = X\rho_3 X^\dagger - \frac{1}{2}X^\dagger X\rho_3 - \frac{1}{2}\rho_3 X^\dagger X. \tag{5.12}$$

Note that all terms involving the $|0\rangle$ state are tunneling events from/to the Fermi seas in the electrodes which destroy coherence immediately. Therefore off-diagonal elements involving $|0\rangle$ will be 0 and we can write the density matrix in the following form:

$$\rho_3 = \begin{pmatrix} \rho P_1 & 0 \\ 0 & P_0 \end{pmatrix}, \tag{5.13}$$

where P_0 is the probability of state $|0\rangle$, $P_1 = 1 - P_0$ the probability of having 1 electron in the system, and ρ a 2×2 density matrix describing the states of the TLS formed by $|\mathrm{L}\rangle$ and $|\mathrm{R}\rangle$.

In this form the master equation reads:

$$\dot{P}_0 = -2\Gamma_\mathrm{S} P_0 + \Gamma_\mathrm{D}\langle \mathrm{R}|\rho|\mathrm{R}\rangle P_1 \tag{5.14}$$

$$\dot{\rho}P_1 + \rho\dot{P}_1 = \left(-\frac{i}{\hbar}[H,\rho] + \mathcal{D}\rho - \frac{\Gamma_\mathrm{D}}{2}\left(|\mathrm{R}\rangle\langle\mathrm{R}|\rho + \rho|\mathrm{R}\rangle\langle\mathrm{R}|\right)\right) P_1 + \Gamma_\mathrm{S}|\mathrm{L}\rangle\langle\mathrm{L}|P_0. \tag{5.15}$$

We note the asymmetric roles played by Γ_S and Γ_D: Γ_S fills the two-level system whereas Γ_D empties the TLS, which is considered as relaxation process causing decoherence.

We are interested in a TLS under continuous microwave drive but an otherwise time-independent Hamiltonian. The non-Hamiltonian terms in the master equation describe couplings to Markovian baths and therefore cannot introduce other time-dependences. According to Floquet's theorem the diagonal elements of the density matrix are then periodic in time with the same periodicity as the explicit time dependence in the Hamiltonian, due to the microwave drive [13]. If the microwave frequency is much faster than all other terms in the Hamiltonian as well as the decoherence rates like in Fig. 5.10, the density matrix will not be able to follow this fast time evolution and we can approximate $\dot{P}_0 = 0$.

Eq. (5.14) then yields:

$$P_0 = \frac{\Gamma_\mathrm{D}\langle \mathrm{R}|\rho|\mathrm{R}\rangle}{\Gamma_\mathrm{S} + \Gamma_\mathrm{D}\langle \mathrm{R}|\rho|\mathrm{R}\rangle}. \tag{5.16}$$

Putting P_0 in Eq. (5.15) and dividing by P_1 gives the following master equation for the TLS:

$$\dot{\rho} = -\frac{i}{\hbar}[H,\rho] + \mathcal{D}\rho + \Gamma_\mathrm{D}\left(|\mathrm{L}\rangle\langle\mathrm{R}|\rho|\mathrm{R}\rangle\langle\mathrm{L}| - \frac{1}{2}|\mathrm{R}\rangle\langle\mathrm{R}|\rho - \frac{1}{2}\rho|\mathrm{R}\rangle\langle\mathrm{R}|\right) \tag{5.17}$$

$$= -\frac{i}{\hbar}[H,\rho] + \mathcal{D}\rho + \Gamma_\mathrm{D}\mathcal{L}(|\mathrm{L}\rangle\langle\mathrm{R}|)\rho. \tag{5.18}$$

The term due to the leads, $\Gamma_\mathrm{D}\mathcal{L}(|\mathrm{L}\rangle\langle\mathrm{R}|)\rho$, simply describes relaxation of the TLS from $|\mathrm{R}\rangle$ to $|\mathrm{L}\rangle$ with a relaxation time $T_1 = \frac{1}{\Gamma_\mathrm{D}}$.

The current through the system,

$$\langle I\rangle = e\Gamma_S P_0 = \frac{e}{(\Gamma_D\langle \mathrm{R}|\rho|\mathrm{R}\rangle)^{-1} + \Gamma_S^{-1}}, \tag{5.19}$$

only depends on the $|\mathrm{R}\rangle$ state probability and on the tunneling rates Γ_S and Γ_D.

Considering the TLS under microwave driving, we label V_{MW} the amplitude of the microwave drive, f_{MW} the frequency of the drive and ϵ_0 the static detuning between the two states $|\mathrm{L}\rangle$ and $|\mathrm{R}\rangle$, expression (5.19) then writes as:

$$I(\epsilon_0, V_{MW}) = \frac{e}{\frac{1}{\Gamma_R p(\epsilon_0, V_{MW})} + \frac{1}{\Gamma_S}}, \tag{5.20}$$

where $p(\epsilon_0, V_{MW})$ is the probability for the electron to be in $|\mathrm{R}\rangle$ after an infinite number of crossings between the two levels. We use the probability derived by Shevchenko [103]:

$$p(\epsilon_0, V_{MW}) = \sum_n p_n(\epsilon_0, V_{MW}) = \frac{1}{2}\sum_n \frac{\Delta^2 J_n^2}{\frac{\hbar^2}{T_1 T_2} + \frac{T_2}{T_1}(\epsilon_0 - n2\pi\hbar f_{MW})^2 + \Delta^2 J_n^2}, \tag{5.21}$$

where $J_n = J_n(eV_{MW}/2\pi\hbar f_{MW})$ is the n-th order Bessel function of the first kind, $T_2 = (1/T_\phi + 1/2T_1)^{-1}$ the coherence time and Δ the tunneling rate between $|\mathrm{R}\rangle$ and $|\mathrm{L}\rangle$. For the rest of this section, J_n, p and p_n will always refer to $J_n(eV_{MW}/2\pi\hbar f_{MW})$, $p(\epsilon_0, V_{MW})$ and $p_n(\epsilon_0, V_{MW})$.

To simplify expression (5.20), we assume that the probabilities p_n do not overlap each other for any given ϵ_0. This is valid for sufficiently high frequencies where the interference fringes are well separated in energy, i.e. for frequencies that verify:

$$f_{MW} \gg \frac{1}{\pi T_2}\sqrt{1 + (\Delta/\hbar)^2 T_1 T_2}. \tag{5.22}$$

Thus we can assume that $p_n = 0$ for any order n but the one, called n_{ϵ_0}, which verifies the condition $|\epsilon_0 - n_{\epsilon_0} 2\pi\hbar f_{MW}| < \pi\hbar f_{MW}$. We can then bring the sum in expression (5.21) from the denominator to the numerator in expression (5.20) and get

$$I(\epsilon_0, V_{MW}) = \sum_n I_n(\epsilon_0, V_{MW}) \tag{5.23}$$

with

$$I_n(\epsilon_0, V_{MW}) = \frac{e}{2}\frac{\Delta^2 J_n^2}{\frac{\hbar^2}{T_2} + T_2(\epsilon_0 - n2\pi\hbar f_{MW})^2 + (\frac{1}{\Gamma_D} + \frac{1}{2\Gamma_S})\Delta^2 J_n^2}, \tag{5.24}$$

Under assumption (5.22), the I_n do not overlap and can be fitted individually to Lorentzian functions. I_n then describes the n-th horizontal fridge of Fig. 5.10.

The area A_n and the full width at half maximum w_n of this Lorentzian can be calculated with 3 independent parameters T_2, Δ and $\eta = T_2(\frac{1}{\Gamma_D} + \frac{1}{2\Gamma_S})$:

$$A_n = \frac{e\pi\Delta^2 J_n^2}{2\sqrt{\hbar^2 + \eta\Delta^2 J_n^2}}; \qquad w_n = \frac{2}{T_2}\sqrt{\hbar^2 + \eta\Delta^2 J_n^2}. \tag{5.25}$$

In absence of microwave driving, we obtain an expression for the stationary current $I_0(\epsilon_0)$ (all I_n with $n \neq 0$ vanish):

$$I_0(\epsilon_0) = \frac{e}{2} \frac{\Delta^2/T_2}{(\frac{\hbar}{T_2})^2 + \epsilon_0^2 + (\frac{1}{\Gamma_D} + \frac{1}{2\Gamma_S})\Delta^2/T_2} \tag{5.26}$$

If we assume no other decoherence process than Γ_D, then $T_2 = 2T_1 = 2/\Gamma_\mathrm{D}$ and eq. (5.26) yields:

$$I_0(\epsilon_0) = \frac{e(\Delta/2)^2\Gamma_\mathrm{D}}{\epsilon_0^2 + (\frac{\hbar\Gamma_\mathrm{D}}{2})^2 + (\frac{\Delta}{2})^2(2 + \frac{\Gamma_\mathrm{D}}{\Gamma_\mathrm{S}})} \tag{5.27}$$

which is exactly the expression derived by Stoof and Nazarov [109].

The stationary current given by eq. (5.26) was investigated in details by Roche [93].

Coherence time

We have fitted our experimental values at f_MW=15 GHz with equations (5.24). We have integrated the current of each ridge over the detuning energy and plot the resulting area in Fig. 5.12.

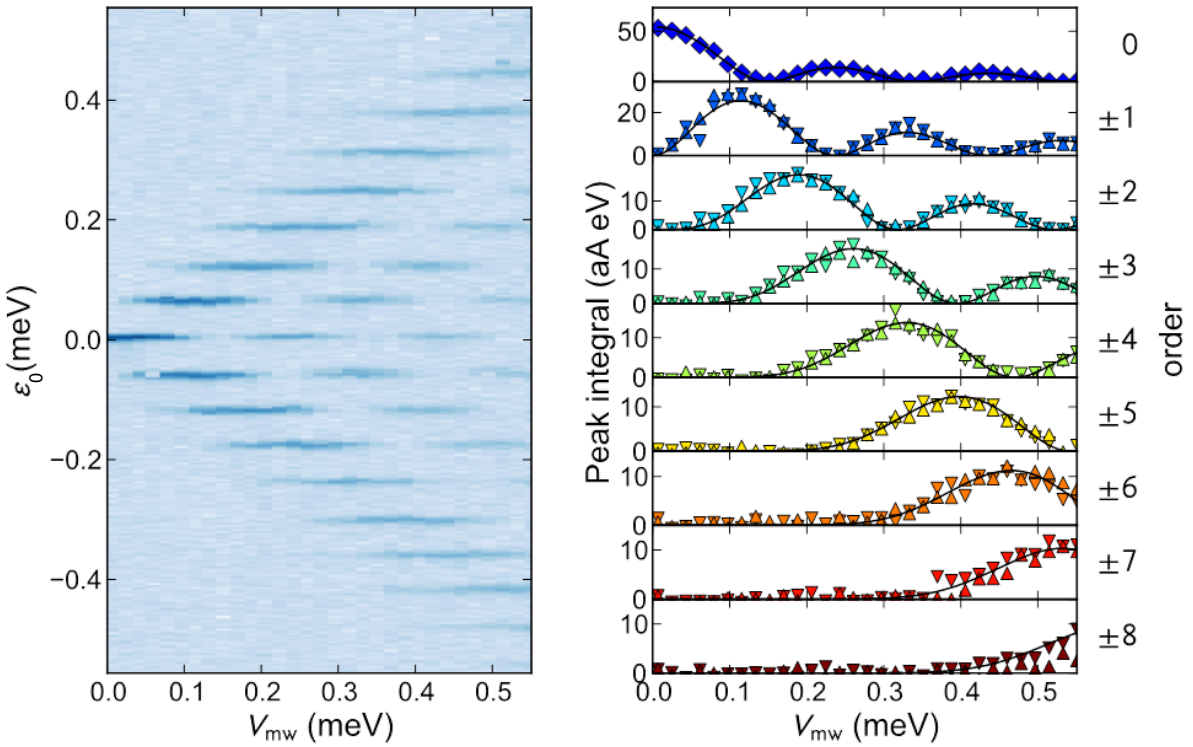

Figure 5.12 *Results of the fit for f=15 GHz. We have fitted all the fringes areas up to the* 8^{th} *for every amplitude with the same set of parameters* η *and* Δ.

We have used only one set of parameters η=$(4.1\,\mathrm{ns})^2$ and Δ=125 MHz to fit our data, up to the 8^{th} order. In order to extract the coherence time T_2, we fed back these values in

expression (5.23) and perform a high resolution of the tunneling current $I_{sd}(\epsilon_0)$ in absence of microwave excitation. We find:

$$\boxed{T_2 \,=\, 0.3 \,\pm\, 0.1\, ns} \tag{5.28}$$

Discussion

Landau-Zener-Stückelberg interferometry is a very general concept: Oliver *et al.* [74] used for example the same theoretical framework for strongly driven superconducting qubits.

The coherence time that we obtained is comparable to the other charge qubit found in the literature concerning GaAs systems [40, 108], which are of the order of the nanosecond. We note that in our case, the coherence time which we obtain includes the decoherence coming from the tunnel rate Γ_D and can't be separated. Nevertheless, following the definition of η, and the value of $\eta = 4.1\,\mathrm{ns}^2$ and $T_2 = 0.3\,\mathrm{ns}$, we can give a lower bound for Γ_D and Γ_S of respectively of about 70 and 35 MHz. On the contrary, if considering that Γ_D is the only source of decoherence, *i.e.* $T_2 = 2/\Gamma_D$, gives an upper bound for Γ_D of 6.6 GHz.

The decoherence of a charge qubit arises from different sources. First, the electron can emit a phonon: this process has been investigated by Barrett *et al.* [7], studying the phonon emission spectra as a function of the detuning energy. Other mechanisms are related to charge noise which modifies the electric field in the nanowire and then the detuning energy [69, 121]. These decoherence rates are difficult to calculate in practice as one needs the noise spectral density on the TLS, which is unknown here. Still the decoherence due to the gate noise can be ruled out as major decoherence source: taking into account the voltage spectral noise at the output of the voltage source, integrated up to 500 Hz (cut-off frequency of the low-pass filter), we obtain a gate voltage noise amplitude of $\delta V_g = 2\,\mu V$. With a level arm parameter of 0.1, this induces a broadening of the levels $\Gamma_2^{gate} = 0.1 * \delta V_g/h \approx 5\,\mathrm{MHz}$, far below the measured decoherence rate.

To further investigate the coherence of such a charge qubit, one would have to get rid of the tunnel rate Γ_D, by performing charge Rabi oscillations under the Fermi sea. The sequence would be very similar to the one presented in the first section of the Chapter: first, an electron would be loaded in the left donor, then coherent oscillations are performed under the Fermi sea when the two levels are aligned, with the period $\hbar/\Delta$. Finally the probability for an electron to be on the right donor is read into the drain. Again, such a measurement would need the setup of a charge-sensing technique in order to measure this possible long coherence time.

Conclusion

During this thesis we have investigated several aspects of the low temperature transport in nanoscale SOI- MOSFET transistors fabricated here in Grenoble by LETI. Thanks to the maturity and the constant developments of CMOS technology, these transistors allow to electrically contact either the very first electrons of the silicon conduction band or single dopants centered in the channel.

We have evidenced that the specific squared cross-section of such silicon nanowires leads for the first electrons to be confined close to the corners of the channel. Therefore we have observed a double-dot system when a negative back-gate voltage repeals the electrons at the top of the nanowire. The mean level spacing (about 1 meV), the charging energy (about 20 meV) and the inter-dot capacitive coupling (1 meV) are determined by transport spectroscopy. Such high energies confirm the very small size of the dots. A magnetic dependence of the addition spectra proves that the two-electron ground state for each dot is a singlet up to at least 5.5 T, corresponding to a double occupation of the lowest energy orbital. The observation of a singlet state shows that the valley degeneracy, a specific feature of silicon quantum dots, has been lifted by the confinement and electric field. This valley splitting is larger than those observed in usual 2DEG silicon heterostructures, which are about 0.1 meV, although the dependence with electric field and surface disorder remain unclear. Moreover we have exhibited the existence of electronic correlations between these confined electrons and the conduction electrons of the reservoirs through preliminary works on the Kondo effect and on the Fermi-edge singularity. This thesis opens new perspectives for silicon quantum dots with the interplay of valleys, orbital levels, spins and many-body correlations.

On a second part, we have extended the work of Mathieu Pierre on transport through single donors in silicon. We are now able to tune the transverse electric field while following the ionization of a donor in a very short trigate nanowire. The complex mesoscopic environment of a MOSFET channel affects the donor properties depending on its position in the nanowire: the usual large electric field induces for the donor to be in an interface regime with the electron pushed away from the donor nucleus. We have revealed the strong influence of the nearby metallic source and drain which screens the Coulomb interaction between two donors but could also contribute to the stabilization of a double occupied state. Here numerical simulations are very helpful to tackle this complex 3D issue, the next step to implement being to consider the double occupation issue. This is challenging as it requires to take into account electron-electron interactions.

Then we have realized the first Coupled-Atom transistors, in collaboration with the

previous student Benoît Roche. It consists of two atoms embedded in series between the source and the drain. In this work we have emphasised on the clear spectroscopy of the exited states which can be performed. Using one donor as an energy filter, we get rid of the temperature broadening of the leads and especially of the local density of states of the contacts in order to unambiguously determine the spectrum of the second donor. We have then measured large valley-orbit splittings up to 10 meV, *i.e.* five times larger than for confined electrons in a corner state. This proves the ultimate size and the somewhat bulk-like behaviour of these donors.

We have started to investigate the coherence of such objects. Concerning the corner state, we have been quickly limited by the low bandwidth inherent to direct loading and read-out of the spin state through the source and drain. Concerning the Coupled-Atom transistor, we have demonstrated for the first time coherent electron exchange between two donors in silicon. This constitutes a major step towards donor-based quantum computing. For both experiments and for future accurate coherence measurements, the setup of charge-sensing techniques increasing the measurements bandwidth is unavoidable.

The next developments of such devices, concerning both dopants and quantum dots, will be to improve the control over the tunnel coupling between these objects, as well as to improve the control over the barriers. Two directions can be foreseen: first, new control gates could be added within the same volume. This would be a step out of the actual CMOS technology process. It would also allow for more tunability and flexibility on the device fabrication with this combined CMOS channel process and home-made gate patterning. Secondly, the idea to combine STM technique with deterministic doping of donors within a CMOS platform is still certainly very challenging but would open doors towards real dopant-based quantum applications.

Conclusion (français)

Au cours de cette thèse nous avons étudié plusieurs aspects du transport à travers des nanotransistors SOI-MOSFET fabriqués à Grenoble par le LETI. Grâce à la maturité et au développement constant de la technologie CMOS, il est maintenant possible de contacter électriquement les premiers électrons de la bande de conduction du silicium et des électrons liés à des dopants uniques si ces derniers sont centrés dans le canal.

Nous avons montré que la géométrie particulière de ces nanofils en silicium avec leur section carrée induit un confinement des premiers électrons dans les coins du canal. Nous avons alors observé un système constitué de deux boîtes quantiques couplées en parallèle lorsque une tension négative est appliquée sur le substrat, repoussant les électrons vers les coins hauts du nanofil. L'écart entre les premiers niveaux (environ 1 meV), l'énergie de charge (environ 20 meV) et l'énergie de charge mutuelle (1 meV) sont déterminées par spectroscopie en transport. De si grandes énergies confirment la petite taille de ces boîtes quantiques. Une dépendance en champ magnétique du spectre d'addition prouve que l'état fondamental à deux électrons est un singulet pour chaque boîte, et ce jusqu'à au moins 5.5 T, les deux électrons occupant donc l'orbitale de plus basse énergie. Cette observation d'un singulet montre que la dégénérescence de vallée, caractéristique particulière du silicium, est complètement levée par le confinement quantique et le champ électrique. L'écart d'énergie mesuré entre les deux vallées est comparable à d'autres observés dans des gaz 2D obtenus par des hétérostructures en silicium, compris entre 0.1 et 1 meV. La compréhension de cette levée de dégénérescence en fonction du champ électrique et du désordre de surface reste encore à approfondir. De plus nous avons montré qu'il existe des corrélations électroniques entre ces électrons confinés et les électrons de conduction des réservoirs en étudiant l'effet Kondo et les singularités au niveau de Fermi, ces travaux restant aussi à compléter. Ces travaux ouvrent de nouvelles perspectives pour les études et les applications des boîtes quantiques en silicium avec ce mélange entre dégénrescences de vallée, de spin, les niveaux orbitaux et des corrélations à N corps.

Dans un deuxième temps nous avons poursuivi le travail entrepris par Mathieu Pierre concernant le transport à travers des dopants uniques dans le silicium. Nous sommes maintenant capable de modifier le champ électrique transverse tout en suivant l'ionisation d'un donneur dans un nanofil trigate très court grâce aux deux grilles polarisables (grille avant et substrat). L'environnement mésoscopique très complexe autour du donneur affecte ses propriétés en fonction de sa position dans le nanofil: le large champ électrique qui règne dans le nanofil implique pour l'électron lié au donneur d'être dans un état dit "interfacial" où la fonction d'onde est pour une part non plus centrée sur le donneur mais poussée vers une interface. Nous avons aussi révélé l'influence très forte des sources et drain mé-

talliques très proches du donneur qui écrantent les intéractions coulombiennes entre les donneurs mais qui peuvent aussi contribuer à stabiliser d'un état de double occupation de ces dopants. Des simulations numériques prenant en compte la réelle géométrie 3D des échantillons nous ont aidés à comprendre ces mécanismes d'écrantage. Une prochaine étape serait de simuler la double occupation d'un donneur, ce qui reste encore exigeant car cela demande de prendre en compte les intéractions électron-électron.

Nous avons ensuite réalisé en collaboration avec Benoît Roche, l'étudiant qui m'a précédé, le premier transistor à atomes couplés. Il présente un nouveau principe de fonctionnement: le courant est contrôlé par l'alignement des états fondamentaux de deux dopants placés en série entre la source et le drain. Dans cette thèse nous nous sommes concentrés sur l'aspect spectroscopique, montrant que ce principe permet d'effectuer une mesure très précise de l'écart entre les niveaux d'un donneur. En effet, utilisant l'état fondamental d'un donneur comme filtre en énergie, il est possible de s'affranchir de l'élargissement thermique des densités d'état des contacts et surtout de leurs fluctuations locales afin de déterminer sans ambiguïté le spectre du deuxième donneur. Nous avons alors mesuré des levées de dégénérescence de vallée jusqu'à 10 meV, i.e. presque un ordre de grandeurplus grand que celles medurées pour les premiers électrons de la bande de conduction confinés dans les états de coin. Cela prouve la taile ulime des fonctions d'onde électronique autour de ces donneurs malgré la présence de la nanostructure.

Nous avons commencé à s'intéresser à la cohérence de tels objets. En ce qui concerne la mesure du temps de cohérence de l'état exité de spin d'un électron confiné dans un état de coin, nous avons été limité par la trop faible bande passante de notre montage, conséquence directe du fait de devoir mesurer le courant à travers ce même état entre les source et drain. Le transistor à atomes couplés nous a lui permis de démontrer pour la première qu'il est possible d'induire des échanges cohérents d'une charge entre deux atomes. Cela constitue une avancée majeure vers de futures applications en calculs quantiques avec des dopants dans le silicium. Mais pour ces deux expériences, le développement de détecteurs de charge pour augmenter la bande passante est indispensable.

Concernant la fabrication des échantillons, que ce soit pour les dopants ou les boîtes quantiques, il semble nécessaire de pouvoir contrôler de manière plus fine à la fois les couplages tunnels entre ces objets et aussi ceux avec les réservoirs. Deux directions doivent être privilégiées: tout d'abord on peut imaginer de nouvelles architectures impliquant de plus nombreuses grilles de contrôle, même si cela n'est pas la direction choisie par la microélectronique et la technologie CMOS. On peut alors imaginer de combiner un aspect de fabrication utilisant des procédés CMOS pour la gravure du canal et un aspect de fabrication propre à nos besoins en ce qui concerne la déposition des grilles, ce qui est réalisable aussi au CEA Grenoble avec une salle blanche dédiée à ce genre d'activités. Cela donnerait plus de flexibilité sur la fabrication des échantillons. Deuxièmement l'idée de combiner une technique de microscopie locale pour implanter des dopants de manière déterministe au sein d'une plateforme CMOS est une perspective très intéressante pour des applications quantiques, même si de nombreux défis restent à réaliser.

Appendix A

Our samples are fabricated by LETI, a semi-industrial microelectronics foundry. As compared to standard fabrication process for fundamental research, usually made in a research clean room, here we have at our disposal many more samples. Indeed samples are fabricated on 300 mm-diameter silicon wafers, which contain around 50000 samples. We detail in the following how we can access a specific sample starting from a whole wafer.

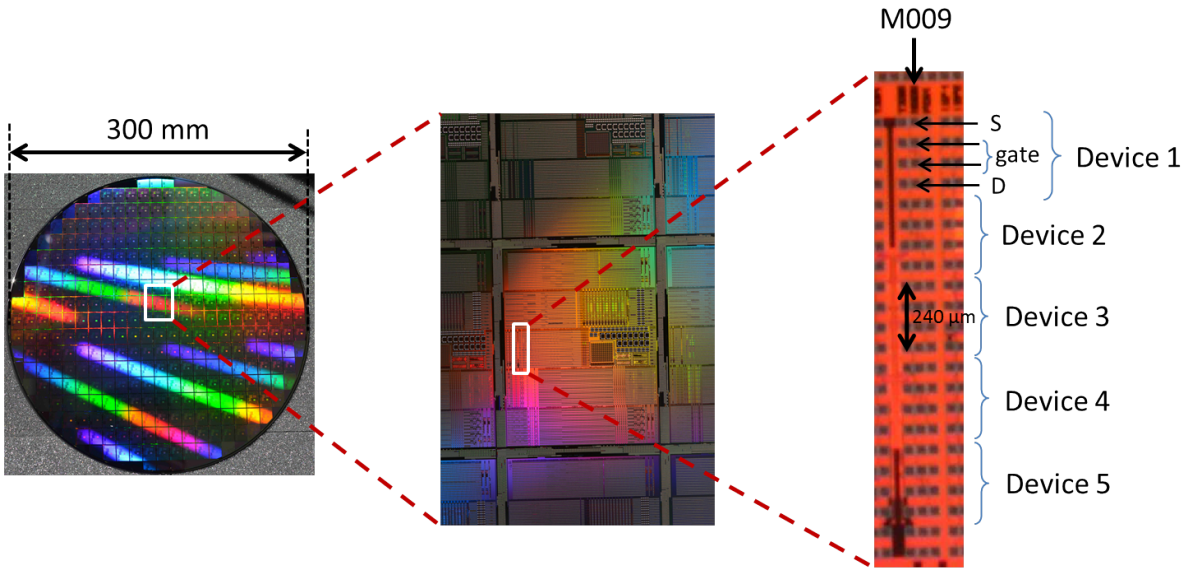

Figure 5.13 *(left) picture of a whole 300 mm-diameter wafer. It contains about 200 dice, which have the same nominal samples. (center) Picture of a typical die. Each die is divided into different arrays of bonding pads used to contact the samples. (right) Zoom on the array of the M009 devices to identify the source, drain and the gate bonding pads for the devices* M009_1 *to* M009_5.

We will take the example of the devices presented in Chapter 2, called M009. A picture of a typical wafer is shown in Fig. 5.13. A wafer is divided in around 200 dice, whose one is represented in the middle picture of Fig. 5.13. On a single die, all the planned samples are fabricated in a specific position. For instance, the samples presented in Chapter 2 are fabricated in the region corresponding to the right picture of Fig. 5.13 (*i.e.* a blow-up of the middle picture). We can observe a vertical array of bonding pads, designed by the vertical arrow. The first four pads, designed by the horizontal arrows and separated by 80 μm, correspond to a single device (called Device 1 or M009_1) with from top to bottom the Source pad, the two pads for the gate, and the Drain pad. This sequence is

repeated for the pads located below, which correspond to the devices called from M009_2 to M009_5. Generally, the samples belonging to such an array differ by a geometrical parameter (usually width or length). In the case of M009, devices 1 to 5 have a width of 40 nm and respective gate lengths of 34, 44, 74, 94 and 114 nm.

As mentioned, all dice contain the exact same devices. Thus, studying a sample (for instance M009_1) from die to die, we can perform statistics of the fabrication process. In order to measure the characteristics of several samples on the whole wafer, we use a commercial machine bought by LETI dedicated for room-temperature automatic measurements. It is composed of a horizontal frame on which the wafer is attached and of conducting pins which can contact the desired bonding pads (SD and gates). An I-V characteristics of the device is then recorded thanks to an I-V source/measurement station, whose outputs and inputs are connected to the pins. Moving the frame with respect to the pins allow to contact and measure the exact same device on different dice. After a few wafer alignment and calibration steps, these measures can automatically been carried out, saving a considerable amount of time. For instance we measured all the M009 devices (1 to 5) on 118 dice of one wafer in about 10 hours, which represents in total 590 samples. As a result, we plot in Fig. 5.14 these measurements, separated in five different plots according to the device number (M009_1 to M009_5). First one can notice that the yield is excellent, close to 100%, with only a few non-working samples. We can also note a very low variability in the threshold voltage and in the sub-threshold slope. Only for the devices M009_1 and M009_2 this variability is slightly increased, showing the difficulty to control the fabrication process for these shortest gate lengths.

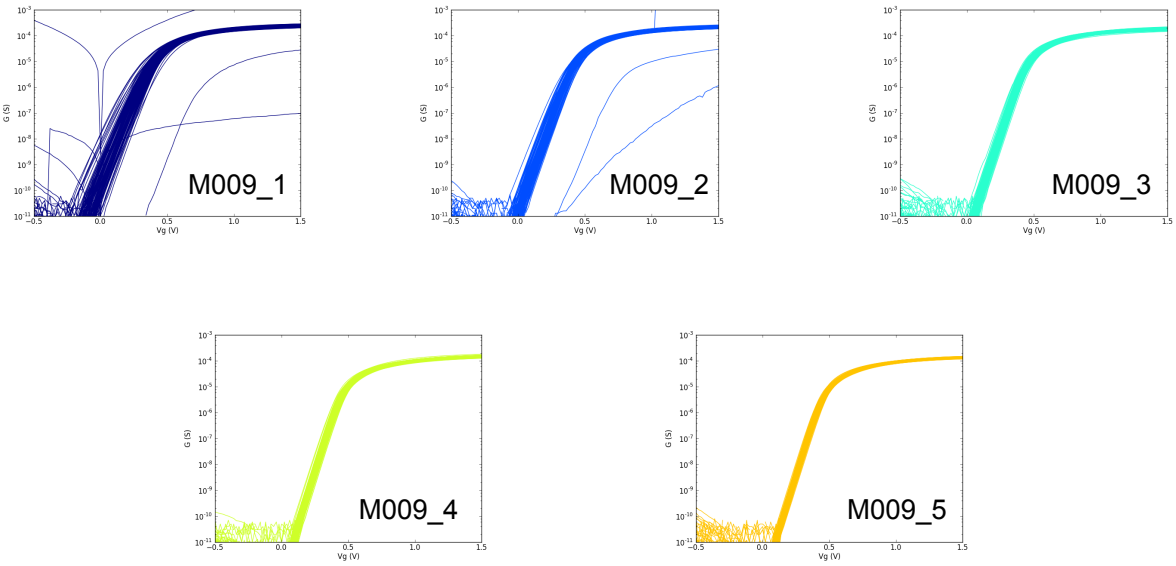

Figure 5.14 *G-Vg characteristics at room temperature for samples M009 performed on 118 dice of the same wafer. The width of the channel is constant (40nm). The gate length changes from 34 nm (*M009_1*) to 114 nm (*M009_5*). The yield is almost 100% and the variability is very low, except for the two shortest gate length.*

Finally, apart from the geometrical characteristics of a device (gate length, width) which can be varied within the same wafer as we have shown above, other fabrication parameters can changed from wafer to wafer, as instance the channel pre-doping, the dimensions of the spacers or the thickness of the film. We give in Fig. 5.15 an array giving the characteristics of 25 wafers, corresponding to a full batch fabricated by LETI.

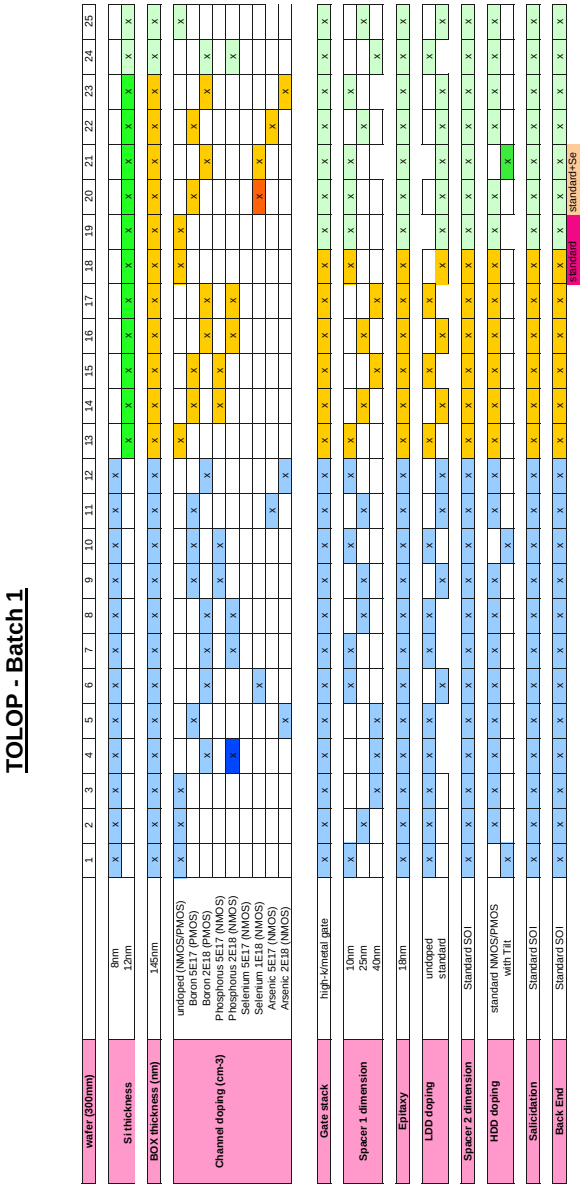

Figure 5.15 *Split of the different fabrication parameters chosen for the 25 wafers of one batch fabricated by LETI.*

List of publications

- *Few electrons in the corner states of a silicon nanowire field effect transistor.*
  B. Voisin, V.-H. Nguyen, J. Renard, X. Jehl, S. Barraud, F. Triozon, M. Vinet, I. Duchemin, Y.-M. Niquet, S. De Franceschi, and M. Sanquer.
  in preparation.

- *Ionization of As dopants in a silicon nanowire.*
  B. Voisin, M. Cobian, X. Jehl, M. Vinet, Y.-M. Niquet, C. Delerue, S. De Franceschi, and M. Sanquer.
  in preparation.

- *A hybrid metal/semiconductor electron pump for practical realization of a quantum ampere.*
  X. Jehl, B.Voisin, T. Charron, P. Clapera, S. Ray, B. Roche, M. Sanquer, S. Djordjevic, L. Devoille, R. Wacquez, M. Vinet
  Phys. Rev. X **3**, 021012 (2013)

- *Coupling and coherent electrical control of two dopants in a silicon nanowire.*
  E. Dupont-Ferrier, B. Roche, B. Voisin, X. Jehl, R. Wacquez, M. Vinet, M. Sanquer, et S. De Franceschi.
  Phys. Rev. Lett. **110**, 136802 (2013)

- *A two-atom electron pump.*
  B. Roche, R.P. Riwar, B. Voisin, E. Dupont-Ferrier, M. Vinet, R. Wacquez, J. Splettstoesser, M. Sanquer, X. Jehl.
  Nature Communications, **4**, 1581 (2013)

- *Detection of a Large Valley-Orbit Splitting in Silicon with Two-Donor Spectroscopy.*
  B. Roche, E. Dupont-Ferrier, B. Voisin, M. Cobian, X. Jehl, R. Wacquez, M. Vinet, Y.-M. Niquet, and M. Sanquer.
  Phys. Rev. Lett. **108**, 206812 (2012)

- *A tunable, dual mode field-effect or single electron transistor.*
  B. Roche, B. Voisin, X. Jehl, R. Wacquez, M. Sanquer, M. Vinet, V. Deshpande and B. Previtali.
  Appl. Phys. Lett. **100**, 032107 (2012)

Bibliography

[1] D. A. Abanin and L. S. Levitov. Tunable fermi-edge resonance in an open quantum dot. *Phys. Rev. Lett.*, 93(12):126802–, September 2004.

[2] E. Abrahams, P. W. Anderson, D. C. Licciardello, and T. V. Ramakrishnan. Scaling theory of localization: Absence of quantum diffusion in two dimensions. *Phys. Rev. Lett.*, 42(10):673–676, March 1979.

[3] P. W. Anderson. Absence of diffusion in certain random lattices. *Phys. Rev.*, 109(5):1492–1505, March 1958.

[4] Tsuneya Ando, Alan B. Fowler, and Frank Stern. Electronic properties of two-dimensional systems. *Rev. Mod. Phys.*, 54(2):437–672, April 1982.

[5] A. Asenov. Random dopant induced threshold voltage lowering and fluctuations in sub-0.1 μm mosfet's: A 3-d “atomistic” simulation study. *Electron Devices, IEEE Transactions on*, 45(12):2505–2513, 1998.

[6] J. Bardeen and W. H. Brattain. The transistor, a semi-conductor triode. *Phys. Rev.*, 74(2):230–231, July 1948.

[7] S. D. Barrett and G. J. Milburn. Measuring the decoherence rate in a semiconductor charge qubit. *Phys. Rev. B*, 68(15):155307–, October 2003.

[8] C. W. J. Beenakker. Theory of coulomb-blockade oscillations in the conductance of a quantum dot. *Phys. Rev. B*, 44(4):1646–1656, July 1991.

[9] L. Besombes, Y. Léger, L. Maingault, D. Ferrand, H. Mariette, and J. Cibert. Probing the spin state of a single magnetic ion in an individual quantum dot. *Phys. Rev. Lett.*, 93(20):207403–, November 2004.

[10] H. Bethe and S. Salpeter. *Quantum Mechanics of One- and Two-Electrons Atoms*. 2008.

[11] Edgar Bonet, Mandar M. Deshmukh, and D. C. Ralph. Solving rate equations for electron tunneling via discrete quantum states. *Phys. Rev. B*, 65(4):045317–, January 2002.

[12] M. G. Borselli, R. S. Ross, A. A. Kiselev, E. T. Croke, K. S. Holabird, P. W. Deelman, L. D. Warren, I. Alvarado-Rodriguez, I. Milosavljevic, F. C. Ku, W. S.

Wong, A. E. Schmitz, M. Sokolich, M. F. Gyure, and A. T. Hunter. Measurement of valley splitting in high-symmetry Si/SiGe quantum dots. *Appl. Phys. Lett.*, 98(12):123118–3, March 2011.

[13] Heinz-Peter Breuer, Wolfgang Huber, and Francesco Petruccione. Quasistationary distributions of dissipative nonlinear quantum oscillators in strong periodic driving fields. *Phys. Rev. E*, 61(5):4883–4889, May 2000.

[14] M. J. Calderõn, J. Verduijn, G. P. Lansbergen, G. C. Tettamanzi, S. Rogge, and Belita Koiller. Heterointerface effects on the charging energy of the shallow D^- ground state in silicon: Role of dielectric mismatch. *Phys. Rev. B*, 82(7):075317–, August 2010.

[15] James R. Chelikowsky and Marvin L. Cohen. Electronic structure of silicon. *Phys. Rev. B*, 10(12):5095–5107, December 1974.

[16] Zener Clarence. Non-adiabatic crossing of energy levels. *Proceedings of the Royal Society of London. Series A.*, 137(833):696–702, 1932.

[17] D. H. Cobden and B. A. Muzykantskii. Finite-temperature fermi-edge singularity in tunneling studied using random telegraph signals. *Phys. Rev. Lett.*, 75(23):4274–4277, December 1995.

[18] S. De Franceschi, S. Sasaki, J. M. Elzerman, W. G. van der Wiel, S. Tarucha, and L. P. Kouwenhoven. Electron cotunneling in a semiconductor quantum dot. *Phys. Rev. Lett.*, 86(5):878–881, January 2001.

[19] S. Deleonibus. Physical and technological limitations of nanocmos devices to the end of the roadmap and beyond. *The European Physical Journal - Applied Physics*, 36(03):197–214, 2006.

[20] V. Deshpande. *Scaling Beyond Moore: Single Electron Transistor and Single Atom Transistor Integration on CMOS*. PhD thesis, Université de Grenoble, 2012.

[21] Mamadou Diarra, Christophe Delerue, Yann-Michel Niquet, and Guy Allan. Screening and polaronic effects induced by a metallic gate and a surrounding oxide on donor and acceptor impurities in silicon nanowires. *J. Appl. Phys.*, 103(7):073703–5, April 2008.

[22] A L Efros and B Shklovskii. *Electronic properties of doped semiconductors*. 1984.

[23] A L Efros and B I Shklovskii. Coulomb gap and low temperature conductivity of disordered systems. *Journal of Physics C: Solid State Physics*, 8(4):L49–, 1975.

[24] C C Escott, F A Zwanenburg, and A Morello. Resonant tunnelling features in quantum dots. *Nanotechnology*, 21(27):274018–, 2010.

[25] Holger Frahm, Carsten von Zobeltitz, Niels Maire, and Rolf J. Haug. Fermi-edge singularities in transport through quantum dots. *Phys. Rev. B*, 74(3):035329–, July 2006.

[26] Mark Friesen, M. A. Eriksson, and S. N. Coppersmith. Magnetic field dependence of valley splitting in realistic Si/SiGe quantum wells. *Applied Physics Letters*, 89(20):–, 2006.

[27] Martin Fuechsle, MahapatraS., ZwanenburgF. A., Mark Friesen, ErikssonM. A., and Michelle Y. Simmons. Spectroscopy of few-electron single-crystal silicon quantum dots. *Nat Nano*, 5(7):502–505, July 2010.

[28] Martin Fuechsle, Jill A. Miwa, Suddhasatta Mahapatra, Hoon Ryu, Sunhee Lee, Oliver Warschkow, Lloyd C. L. Hollenberg, Gerhard Klimeck, and Michelle Y. Simmons. A single-atom transistor. *Nat Nano*, 7(4):242–246, April 2012.

[29] Akira Fujiwara, Hiroshi Inokawa, Kenji Yamazaki, Hideo Namatsu, Yasuo Takahashi, Neil M. Zimmerman, and Stuart B. Martin. Single electron tunneling transistor with tunable barriers using silicon nanowire metal-oxide-semiconductor field-effect transistor. *Appl. Phys. Lett.*, 88(5):053121–3, January 2006.

[30] A. K. Geim, T. J. Foster, A. Nogaret, N. Mori, P. J. McDonnell, Jr. Scala, N. La, P. C. Main, and L. Eaves. Resonant tunneling through donor molecules. *Phys. Rev. B*, 50(11):8074–8077, September 1994.

[31] A. K. Geim, P. C. Main, Jr. La Scala, N., L. Eaves, T. J. Foster, P. H. Beton, J. W. Sakai, F. W. Sheard, M. Henini, G. Hill, and M. A. Pate. Fermi-edge singularity in resonant tunneling. *Phys. Rev. Lett.*, 72(13):2061–2064, March 1994.

[32] L. Glazman and Raikh M. Resonant kondo transparency of a barrier with quasilocal impurity states. *JETP Letters*, 47(8):452–455, 1988.

[33] D. Goldhaber-Gordon, J. Göres, M. A. Kastner, Hadas Shtrikman, D. Mahalu, and U. Meirav. From the kondo regime to the mixed-valence regime in a single-electron transistor. *Phys. Rev. Lett.*, 81(23):5225–5228, December 1998.

[34] D. Goldhaber-Gordon, Hadas Shtrikman, D. Mahalu, David Abusch-Magder, U. Meirav, and M. A. Kastner. Kondo effect in a single-electron transistor. *Nature*, 391(6663):156–159, January 1998.

[35] V. N. Golovach, X. Jehl, M. Houzet, M. Pierre, B. Roche, M. Sanquer, and L. I. Glazman. Single-dopant resonance in a single-electron transistor. *Phys. Rev. B*, 83(7):075401–, February 2011.

[36] R. Hanson, L. P. Kouwenhoven, J. R. Petta, S. Tarucha, and L. M. K. Vandersypen. Spins in few-electron quantum dots. *Rev. Mod. Phys.*, 79(4):1217–1265, October 2007.

[37] R. Hanson, B. Witkamp, L. M. K. Vandersypen, L. H. Willems van Beveren, J. M. Elzerman, and L. P. Kouwenhoven. Zeeman energy and spin relaxation in a one-electron quantum dot. *Phys. Rev. Lett.*, 91(19):196802–, November 2003.

[38] Y. L. Hao, A. P. Djotyan, A. A. Avetisyan, and F. M. Peeters. Shallow donor states near a semiconductor-insulator-metal interface. *Phys. Rev. B*, 80(3):035329–, July 2009.

[39] Y L Hao, A P Djotyan, A A Avetisyan, and F M Peeters. D^- shallow donor near a semiconductor-metal and a semiconductor-dielectric interface. *Journal of Physics: Condensed Matter*, 23(11):115303–, 2011.

[40] T. Hayashi, T. Fujisawa, H. D. Cheong, Y. H. Jeong, and Y. Hirayama. Coherent manipulation of electronic states in a double quantum dot. *Phys. Rev. Lett.*, 91(22):226804–, November 2003.

[41] Martina Hentschel, Denis Ullmo, and Harold U. Baranger. Fermi-edge singularities in the mesoscopic x-ray edge problem. *Phys. Rev. Lett.*, 93(17):176807–, October 2004.

[42] M. Hofheinz, X. Jehl, M. Sanquer, G. Molas, M. Vinet, and S. Deleonibus. Individual charge traps in silicon nanowires. 54(3):299–307–, 2006.

[43] Max Hofheinz. *Coulomb blockade in silicon nanowire MOSFETs*. PhD thesis, Université Grenoble I – Joseph Fourier, 2006.

[44] L. C. L. Hollenberg, A. S. Dzurak, C. Wellard, A. R. Hamilton, D. J. Reilly, G. J. Milburn, and R. G. Clark. Charge-based quantum computing using single donors in semiconductors. *Phys. Rev. B*, 69(11):113301–, March 2004.

[45] Binhui Hu and C. H. Yang. Electron spin blockade and singlet-triplet transition in a silicon single electron transistor. *Phys. Rev. B*, 80(7):075310–, August 2009.

[46] Pablo Jarillo-Herrero, Jing Kong, Herre S.J. van der Zant, Cees Dekker, Leo P. Kouwenhoven, and Silvano De Franceschi. Orbital kondo effect in carbon nanotubes. *Nature*, 434(7032):484–488, March 2005.

[47] B. E. Kane. A silicon-based nuclear spin quantum computer. *Nature*, 393(6681):133–137, May 1998.

[48] KatsarosG., SpathisP., StoffelM., FournelF., MongilloM., BouchiatV., LeflochF., RastelliA., SchmidtO. G., and De FranceschiS. Hybrid superconductor-semiconductor devices made from self-assembled sige nanocrystals on silicon. *Nat Nano*, 5(6):458–464, June 2010.

[49] M. A. H. Khalafalla, Y. Ono, K. Nishiguchi, and A. Fujiwara. Identification of single and coupled acceptors in silicon nano-field-effect transistors. *Applied Physics Letters*, 91(26):–, 2007.

[50] Paul M. Koenraad and Michael E. Flatte. Single dopants in semiconductors. *Nat Mater*, 10(2):91–100, February 2011.

[51] W. Kohn and J. M. Luttinger. Theory of donor states in silicon. *Phys. Rev.*, 98(4):915–922, May 1955.

[52] Jun Kondo. Resistance minimum in dilute magnetic alloys. *Progress of Theoretical Physics*, 32(1):37–49, July 1964.

[53] J. Könemann, P. König, T. Schmidt, E. McCann, Vladimir I. Fal'ko, and R. J. Haug. Correlation-function spectroscopy of inelastic lifetime in heavily doped gaas heterostructures. *Phys. Rev. B*, 64(15):155314–, September 2001.

[54] F. H. L. Koppens, C. Buizert, K. J. Tielrooij, I. T. Vink, K. C. Nowack, T. Meunier, L. P. Kouwenhoven, and L. M. K. Vandersypen. Driven coherent oscillations of a single electron spin in a quantum dot. *Nature*, 442(7104):766–771, August 2006.

[55] Christian Kurtsiefer, Sonja Mayer, Patrick Zarda, and Harald Weinfurter. Stable solid-state source of single photons. *Phys. Rev. Lett.*, 85(2):290–293, July 2000.

[56] N. S. Lai, W. H. Lim, C. H. Yang, F. A. Zwanenburg, W. A. Coish, F. Qassemi, A. Morello, and A. S. Dzurak. Pauli spin blockade in a highly tunable silicon double quantum dot. *Sci. Rep.*, 1:–, October 2011.

[57] Pei F. Laird E.A. and Kouwenhoven L. A valley-spin qubit in a carbon nanotube. *Nat Nano*, 8(8):565–568, August 2013.

[58] G. P. Lansbergen, R. Rahman, C. J. Wellard, I. Woo, J. Caro, N. Collaert, S. Biesemans, G. Klimeck, L. C. L. Hollenberg, and S. Rogge. Gate-induced quantum-confinement transition of a single dopant atom in a silicon finfet. *Nat Phys*, 4(8):656–661, August 2008.

[59] G. P. Lansbergen, G. C. Tettamanzi, J. Verduijn, N. Collaert, S. Biesemans, M. Blaauboer, and S. Rogge. Tunable kondo effect in a single donor atom. *Nano Lett.*, 10(2):455–460, December 2009.

[60] W H Lim, C H Yang, F A Zwanenburg, and A S Dzurak. Spin filling of valley–orbit states in a silicon quantum dot. *Nanotechnology*, 22(33):335704–, 2011.

[61] W. H. Lim, F. A. Zwanenburg, H. Huebl, M. Mottonen, K. W. Chan, A. Morello, and A. S. Dzurak. Observation of the single-electron regime in a highly tunable silicon quantum dot. *Appl. Phys. Lett.*, 95(24):242102–3, December 2009.

[62] Daniel Loss and David P. DiVincenzo. Quantum computation with quantum dots. *Phys. Rev. A*, 57(1):120–126, January 1998.

[63] Pierre M., Wacquez R., Jehl X., Sanquer M., Vinet M., and Cueto O. Single-donor ionization energies in a nanoscale cmos channel. *Nat Nano*, 5(2):133–137, February 2010.

[64] K. A. Matveev and A. I. Larkin. Interaction-induced threshold singularities in tunneling via localized levels. *Phys. Rev. B*, 46(23):15337–15347, Dec 1992.

[65] Andrea Morello, Jarryd J. Pla, Floris A. Zwanenburg, Kok W. Chan, Kuan Y. Tan, Hans Huebl, Mikko Mottonen, Christopher D. Nugroho, Changyi Yang, Jessica A. van Donkelaar, Andrew D. C. Alves, David N. Jamieson, Christopher C. Escott, Lloyd C. L. Hollenberg, Robert G. Clark, and Andrew S. Dzurak. Single-shot readout of an electron spin in silicon. *Nature*, 467(7316):687–691, October 2010.

[66] John J. L. Morton, Alexei M. Tyryshkin, Richard M. Brown, Shyam Shankar, Brendon W. Lovett, Arzhang Ardavan, Thomas Schenkel, Eugene E. Haller, Joel W. Ager, and S. A. Lyon. Solid-state quantum memory using the 31p nuclear spin. *Nature*, 455(7216):1085–1088, October 2008.

[67] N. F. MOTT. Metal-insulator transition. *Rev. Mod. Phys.*, 40(4):677–683, October 1968.

[68] M. Mottonen, K. Y. Tan, K. W. Chan, F. A. Zwanenburg, W. H. Lim, C. C. Escott, J.-M. Pirkkalainen, A. Morello, C. Yang, J. A. van Donkelaar, A. D. C. Alves, D. N. Jamieson, L. C. L. Hollenberg, and A. S. Dzurak. Probe and control of the reservoir density of states in single-electron devices. *Phys. Rev. B*, 81(16):161304–, April 2010.

[69] Y. Nakamura, Yu. A. Pashkin, T. Yamamoto, and J. S. Tsai. Charge echo in a cooper-pair box. *Phys. Rev. Lett.*, 88(4):047901–, January 2002.

[70] Tai Kai Ng and Patrick A. Lee. On-site coulomb repulsion and resonant tunneling. *Phys. Rev. Lett.*, 61(15):1768–1771, October 1988.

[71] Y. M. Niquet, D. Rideau, C. Tavernier, H. Jaouen, and X. Blase. Onsite matrix elements of the tight-binding hamiltonian of a strained crystal: Application to silicon, germanium, and their alloys. *Phys. Rev. B*, 79(24):245201–, June 2009.

[72] E. P. Nordberg, G. A. Ten Eyck, H. L. Stalford, R. P. Muller, R. W. Young, K. Eng, L. A. Tracy, K. D. Childs, J. R. Wendt, R. K. Grubbs, J. Stevens, M. P. Lilly, M. A. Eriksson, and M. S. Carroll. Enhancement-mode double-top-gated metal-oxide-semiconductor nanostructures with tunable lateral geometry. *Phys. Rev. B*, 80(11):115331–, September 2009.

[73] Home Page of International Roadmap. http://www.itrs.net/.

[74] William D. Oliver, Yang Yu, Janice C. Lee, Karl K. Berggren, Leonid S. Levitov, and Terry P. Orlando. Mach-zehnder interferometry in a strongly driven superconducting qubit. *Science*, 310(5754):1653–1657, December 2005.

[75] Yukinori Ono, Jean-Francois Morizur, Katsuhiko Nishiguchi, Kei Takashina, Hiroshi Yamaguchi, Kazuma Hiratsuka, Seiji Horiguchi, Hiroshi Inokawa, and Yasuo Takahashi. Impurity conduction in phosphorus-doped buried-channel silicon-on-insulator field-effect transistors at temperatures between 10 and 295k. *Phys. Rev. B*, 74(23):235317–, December 2006.

[76] T. H. Oosterkamp, T. Fujisawa, W. G. van der Wiel, K. Ishibashi, R. V. Hijman, S. Tarucha, and L. P. Kouwenhoven. Microwave spectroscopy of a quantum-dot molecule. *Nature*, 395(6705):873–876, October 1998.

[77] Mickael L. Perrin, Christopher J. O. Verzijl, Christian A. Martin, Ahson J. Shaikh, Rienk Eelkema, van EschJan H., Jan M. van Ruitenbeek, Joseph M. Thijssen, Herre S. J. van der Zant, and Diana Dulic. Large tunable image-charge effects in single-molecule junctions. *Nat Nano*, 8(4):282–287, April 2013.

[78] J. R. Petta, A. C. Johnson, J. M. Taylor, E. A. Laird, A. Yacoby, M. D. Lukin, C. M. Marcus, M. P. Hanson, and A. C. Gossard. Coherent manipulation of coupled electron spins in semiconductor quantum dots. *Science*, 309(5744):2180–2184, September 2005.

[79] Mathieu Pierre. *Transport mono-électronique et détection de dopants uniques dans des transistors silicium*. PhD thesis, Université Grenoble I – Joseph Fourier, 2010.

[80] PierreM., WacquezR., JehlX., SanquerM., VinetM., and CuetoO. Single-donor ionization energies in a nanoscale cmos channel. *Nat Nano*, 5(2):133–137, February 2010.

[81] F. G. Pikus and K. K. Likharev. Nanoscale field-effect transistors: An ultimate size analysis. *Appl. Phys. Lett.*, 71(25):3661–3663, December 1997.

[82] Jarryd J. Pla, Kuan Y. Tan, Juan P. Dehollain, Wee H. Lim, John J. L. Morton, David N. Jamieson, Andrew S. Dzurak, and Andrea Morello. A single-atom electron spin qubit in silicon. *Nature*, 489(7417):541–545, September 2012.

[83] Jarryd J. Pla, Kuan Y. Tan, Juan P. Dehollain, Wee H. Lim, John J. L. Morton, Floris A. Zwanenburg, David N. Jamieson, Andrew S. Dzurak, and Andrea Morello. High-fidelity readout and control of a nuclear spin qubit in silicon. *Nature*, 496(7445):334–338, April 2013.

[84] Enrico Prati, Marco De Michielis, Matteo Belli, Simone Cocco, Marco Fanciulli, Dharmraj Kotekar-Patil, Matthias Ruoff, Dieter P Kern, David A Wharam, Jan Verduijn, Giuseppe C Tettamanzi, Sven Rogge, Benoit Roche, Romain Wacquez, Xavier Jehl, Maud Vinet, and Marc Sanquer. Few electron limit of n-type metal oxide semiconductor single electron transistors. *Nanotechnology*, 23(21):215204–, 2012.

[85] R. Rahman, G. P. Lansbergen, J. Verduijn, G. C. Tettamanzi, S. H. Park, N. Collaert, S. Biesemans, G. Klimeck, L. C. L. Hollenberg, and S. Rogge. Electric field reduced charging energies and two-electron bound excited states of single donors in silicon. *Phys. Rev. B*, 84(11):115428–, September 2011.

[86] R. Rahman, J. Verduijn, N. Kharche, G. P. Lansbergen, G. Klimeck, L. C. L. Hollenberg, and S. Rogge. Engineered valley-orbit splittings in quantum-confined nanostructures in silicon. *Phys. Rev. B*, 83(19):195323–, May 2011.

[87] Rajib Rahman, G. P. Lansbergen, Seung H. Park, J. Verduijn, Gerhard Klimeck, S. Rogge, and Lloyd C. L. Hollenberg. Orbital stark effect and quantum confinement transition of donors in silicon. *Phys. Rev. B*, 80(16):165314–, October 2009.

[88] Rajib Rahman, Seung H Park, Gerhard Klimeck, and Lloyd C L Hollenberg. Stark tuning of the charge states of a two-donor molecule in silicon. *Nanotechnology*, 22(22):225202–, 2011.

[89] K. S. Ralls, W. J. Skocpol, L. D. Jackel, R. E. Howard, L. A. Fetter, R. W. Epworth, and D. M. Tennant. Discrete resistance switching in submicrometer silicon inversion layers: Individual interface traps and low-frequency (1/f?) noise. *Phys. Rev. Lett.*, 52(3):228–231, January 1984.

[90] A K Ramdas and S Rodriguez. Spectroscopy of the solid-state analogues of the hydrogen atom: donors and acceptors in semiconductors. *Reports on Progress in Physics*, 44(12):1297–, 1981.

[91] B. Roche, R.-P. Riwar, B. Voisin, E. Dupont-Ferrier, R. Wacquez, M. Vinet, M. Sanquer, J. Splettstoesser, and X. Jehl. A two-atom electron pump. *Nat Commun*, 4:1581–, March 2013.

[92] B. Roche, B. Voisin, X. Jehl, R. Wacquez, M. Sanquer, M. Vinet, V. Deshpande, and B. Previtali. A tunable, dual mode field-effect or single electron transistor. *Appl. Phys. Lett.*, 100(3):032107–3, January 2012.

[93] Benoît Roche. *transport électronique à travers deux dopants, en régime statique et dynamique, dans des transistors silicium*. PhD thesis, Université de Grenoble, 2012.

[94] L. P. Rokhinson, L. J. Guo, S. Y. Chou, and D. C. Tsui. Kondo-like zero-bias anomaly in electronic transport through an ultrasmall si quantum dot. *Phys. Rev. B*, 60(24):R16319–R16321, December 1999.

[95] M. Ruth, T. Slobodskyy, C. Gould, G. Schmidt, and L. W. Molenkamp. Fermi edge singularity in ii–vi semiconductor resonant tunneling structures. *Appl. Phys. Lett.*, 93(18):182104–3, November 2008.

[96] A. L. Saraiva, M. J. Calderón, Rodrigo B. Capaz, Xuedong Hu, S. Das Sarma, and Belita Koiller. Intervalley coupling for interface-bound electrons in silicon: An effective mass study. *Phys. Rev. B*, 84(15):155320–, October 2011.

[97] A. L. Saraiva, M. J. Calderón, Xuedong Hu, S. Das Sarma, and Belita Koiller. Physical mechanisms of interface-mediated intervalley coupling in si. *Phys. Rev. B*, 80(8):081305–, August 2009.

[98] A. L. Saraiva, Belita Koiller, and Mark Friesen. Extended interface states enhance valley splitting in Si/SiO_2. *Phys. Rev. B*, 82(24):245314–, December 2010.

[99] R. J. Schoelkopf, P. Wahlgren, A. A. Kozhevnikov, P. Delsing, and D. E. Prober. The radio-frequency single-electron transistor (rf-set): A fast and ultrasensitive electrometer. *Science*, 280(5367):1238–1242, May 1998.

[100] J. H. F. Scott-Thomas, Stuart B. Field, M. A. Kastner, Henry I. Smith, and D. A. Antoniadis. Conductance oscillations periodic in the density of a one-dimensional electron gas. *Phys. Rev. Lett.*, 62(5):583–586, January 1989.

[101] H. Sellier, G. P. Lansbergen, J. Caro, S. Rogge, N. Collaert, I. Ferain, M. Jurczak, and S. Biesemans. Transport spectroscopy of a single dopant in a gated silicon nanowire. *Phys. Rev. Lett.*, 97(20):206805–, November 2006.

[102] H. Sellier, G. P. Lansbergen, J. Caro, S. Rogge, N. Collaert, I. Ferain, M. Jurczak, and S. Biesemans. Subthreshold channels at the edges of nanoscale triple-gate silicon transistors. *Applied Physics Letters*, 90(7):–, 2007.

[103] S.N. Shevchenko, S. Ashhab, and Franco Nori. Landau-zener-stückelberg interferometry. *Physics Reports*, 492(1):1–30, July 2010.

[104] Shiue-yuan Shiau, Sucismita Chutia, and Robert Joynt. Valley kondo effect in silicon quantum dots. *Phys. Rev. B*, 75(19):195345–, May 2007.

[105] C. B. Simmons, J. R. Prance, B. J. Van Bael, Teck Seng Koh, Zhan Shi, D. E. Savage, M. G. Lagally, R. Joynt, Mark Friesen, S. N. Coppersmith, and M. A. Eriksson. Tunable spin loading and T_1 of a silicon spin qubit measured by single-shot readout. *Phys. Rev. Lett.*, 106(15):156804–, April 2011.

[106] W. J. Skocpol, P. M. Mankiewich, R. E. Howard, L. D. Jackel, D. M. Tennant, and A. Douglas Stone. Universal conductance fluctuations in silicon inversion-layer nanostructures. *Phys. Rev. Lett.*, 56(26):2865–2868, June 1986.

[107] M. Specht, M. Sanquer, S. Deleonibus, and G. Guégan. Signature of kondo effect in silicon quantum dots. *European Physical Journal B*, 26(4):503–508–, 2002.

[108] J. Stehlik, Y. Dovzhenko, J. R. Petta, J. R. Johansson, F. Nori, H. Lu, and A. C. Gossard. Landau-zener-stückelberg interferometry of a single electron charge qubit. *Phys. Rev. B*, 86(12):121303–, September 2012.

[109] T. H. Stoof and Yu. V. Nazarov. Time-dependent resonant tunneling via two discrete states. *Phys. Rev. B*, 53(3):1050–1053, January 1996.

[110] K. Takashina, Y. Ono, A. Fujiwara, Y. Takahashi, and Y. Hirayama. Valley polarization in si(100) at zero magnetic field. *Phys. Rev. Lett.*, 96(23):236801–, June 2006.

[111] Kuan Yen Tan, Kok Wai Chan, Mikko Möttönen, Andrea Morello, Changyi Yang, Jessica van Donkelaar, Andrew Alves, Juha-Matti Pirkkalainen, David N. Jamieson, Robert G. Clark, and Andrew S. Dzurak. Transport spectroscopy of single phosphorus donors in a silicon nanoscale transistor. *Nano Lett.*, 10(1):11–15, December 2009.

[112] Yuan Taur. An analytical solution to a double-gate mosfet with undoped body. *Electron Device Letters, IEEE*, 21(5):245–247, 2000.

[113] G. C. Tettamanzi, J. Verduijn, G. P. Lansbergen, M. Blaauboer, M. J. Calderón, R. Aguado, and S. Rogge. Magnetic-field probing of an su(4) kondo resonance in a single-atom transistor. *Phys. Rev. Lett.*, 108(4):046803–, January 2012.

[114] P. K. Tien and J. P. Gordon. Multiphoton process observed in the interaction of microwave fields with the tunneling between superconductor films. *Phys. Rev.*, 129(2):647–651, January 1963.

[115] W. G. van der Wiel, S. De Franceschi, J. M. Elzerman, T. Fujisawa, S. Tarucha, and L. P. Kouwenhoven. Electron transport through double quantum dots. *Rev. Mod. Phys.*, 75(1):1–22, December 2002.

[116] W. G. van der Wiel, S. De Franceschi, T. Fujisawa, J. M. Elzerman, S. Tarucha, and L. P. Kouwenhoven. The kondo effect in the unitary limit. *Science*, 289(5487):2105–2108, September 2000.

[117] J. Verduijn, G. C. Tettamanzi, and S. Rogge. Wave function control over a single donor atom. *Nano Lett.*, 13(4):1476–1480, March 2013.

[118] Rutger Vrijen, Eli Yablonovitch, Kang Wang, Hong Wen Jiang, Alex Balandin, Vwani Roychowdhury, Tal Mor, and David DiVincenzo. Electron-spin-resonance transistors for quantum computing in silicon-germanium heterostructures. *Phys. Rev. A*, 62(1):012306–, June 2000.

[119] M. Xiao, M. G. House, and H. W. Jiang. Parallel spin filling and energy spectroscopy in few-electron si metal-on-semiconductor-based quantum dots. *Appl. Phys. Lett.*, 97(3):032103–3, July 2010.

[120] M. Xiao, I. Martin, E. Yablonovitch, and H. W. Jiang. Electrical detection of the spin resonance of a single electron in a silicon field-effect transistor. *Nature*, 430(6998):435–439, July 2004.

[121] Igor V. Yurkevich, Jim Baldwin, Igor V. Lerner, and Boris L. Altshuler. Decoherence of charge qubit coupled to interacting background charges. *Phys. Rev. B*, 81(12):121305–, March 2010.

[122] Floris A. Zwanenburg, Andrew S. Dzurak, Andrea Morello, Michelle Y. Simmons, Lloyd C. L. Hollenberg, Gerhard Klimeck, Sven Rogge, Susan N. Coppersmith, and Mark A. Eriksson. Silicon quantum electronics. *Rev. Mod. Phys.*, 85(3):961–1019, July 2013.

[123] Floris A. Zwanenburg, Cathalijn E. W. M. van Rijmenam, Ying Fang, Charles M. Lieber, and Leo P. Kouwenhoven. Spin states of the first four holes in a silicon nanowire quantum dot. *Nano Lett.*, 9(3):1071–1079, February 2009.